Modeling Radiation-induced Mixing at Interfaces Between Low Solubility Metals

by

Liang Zhang

B.S., Shanghai Jiao Tong University (2007)
S.M., Massachusetts Institute of Technology (2009)

Submitted to the Department of Nuclear Science and Engineering
in partial fulfillment of the requirements for the degree of

Doctor of Philosophy

at the

MASSACHUSETTS INSTITUTE OF TECHNOLOGY

February 2014

Author .....
Department of Nuclear Science and Engineering
January 15, 2014

Certified by .....
Michael J. Demkowicz
Assistant Professor of Materials Science and Engineering
Thesis Supervisor

Ceritified by .....
Bilge Yildiz
Associate Professor of Nuclear Science and Engineering
Thesis Reader

Accepted by .....
Mujid S. Kazimi
TEPCO Professor of Nuclear Engineering
Chairman, Department Committee on Graduate Theses

Modeling Radiation-induced Mixing at Interfaces Between Low Solubility Metals

by

Liang Zhang

Submitted to the Department of Nuclear Science and Engineering
on January 15, 2014, in partial fulfillment of the
requirements for the degree of
Doctor of Philosophy

Abstract

This thesis studies radiation-induced mixing at interfaces between low solubility metals using molecular dynamics (MD) computer simulations. It provides original contributions on the fundamental mechanisms of radiation-induced mixing and morphological stability of multilayer nanocomposites under heavy ion or neutron radiation.

An embedded atom method (EAM) interatomic potential is constructed to reproduce the main topological features of the experimental equilibrium phase diagram of the Cu-Nb system in both solid and liquid states. Compared with two previously available EAM Cu-Nb potentials, the phase diagram of the current potential shows better agreement with the experimental phase diagram. The newly constructed potential predicts that the Cu-Nb liquid phase at equilibrium is compositionally patterned over lengths of about 2.3 nm. All three Cu-Nb potentials have the same solid phase behavior but different liquid phase properties, serving as a convenient set of model systems to study the effect of liquid phase properties on radiation-induced mixing.

To study radiation-induced intermixing, a specialized MD simulation is developed that models multiple 10 keV collision cascades sequentially up to a total dose of $\sim$5 displacements per atom (dpa). These simulations are comparable to experiments conducted at cryogenic temperatures. Mixing is modeled using all three Cu-Nb potentials and found to be proportional to the square root of dose, independent of interface crystallography, and highly sensitive to liquid phase interdiffusivity. It occurs primarily by liquid phase interdiffusion in thermal spikes rather than by ballistic displacements. Partial de-mixing is also seen within thermal spikes, regardless of liquid phase solubility, which is explained by segregation of impurities into the liquid core of the thermal spikes.

Additional MD and phase field simulations are carried out on Cu-Nb multilayered nanocomposites with individual layer thicknesses above 1 nm. These simulations demonstrate that Cu-Nb multilayers with individual layer thicknesses above 2-4 nm remain morphologically stable when subjected to 100 keV collision cascades, characteristic of neutron or heavy ion irradiation. The probability of morphological instability rapidly increases as the layer thickness decreases to 1 nm, which is due to

overlap of zones of liquid-like interdiffusion inside radiation-induced thermal spikes at neighboring interfaces in the multilayer.

This work shows that to design morphologically stable radiation-tolerant nanocomposites, it is desirable to a) choose low solubility metals with small liquid phase interdiffusivity as the constituents, and b) use a microstructural length scale larger than twice the size of the interdiffusion zone inside thermal spikes.

Thesis Supervisor: Michael J. Demkowicz
Title: Assistant Professor of Materials Science and Engineering

Acknowledgments

The work in this thesis would be impossible without the wisdom, guidance and support from my advisor Prof. Michael Demkowicz. I am fortunate to be one of his graduate students for the past four and a half years, and it is one of the most invaluable experiences in my life. His rigor, critical thinking, and methodology on how to solve complicated problems will benefit me throughout my future career. I am also grateful for his patience, understanding, and encouragement that helped me overcome the difficulties during the course of my doctoral research.

I would like to thank Prof. Bilge Yildiz to be my thesis reader and bring me to the field of computational materials science when I first came to MIT. Without her introduction, I cannot imagine that I would conduct research in this field. I would also like to thank Profs. Ju Li, Michael Short, and Sidney Yip to serve as my thesis examing committee, and provide many useful feedback and suggestions.

I would like to thank Dr. Alfredo Caro (LANL) to be my doctoral supervision committee member and his hospitality during my two summer visits to Los Alamos National Laboratory, where I learned the techniques of interatomic potential constructions and free energies calculations. I also appreciate his profound insight and fruitful discussions on the radiation-induced mixing.

I owe special thanks to Dr. Enrique Martinez (LANL) for his support in both research and life. I acknowledge his guidance and help on density functional theory calculations of enthalpy of mixing and semi-grand canonical Monte Carlo simulations.

I am also indebted to Dr. Amit Misra, Dr. Ben Liu (LANL), Dr. Ruifeng Zhang (ISU), Prof. Pascal Bellon (UIUC) for their useful discussions and insightful comments.

I would like to thank all members in Demkowicz group at MIT, especially Drs. Kedarnath Kolluri, Richard Baumer and Abishek Kashinath for their support, encouragement and feedback, and Dina Yuryev for her help on phase field modeling.

I am glad to thank Meng Luo, Peng Xu, Xiangdong Liang, Yang Zhang, Vu Huynh, Yue Fan, Guoqiang Xu, Wenshan Yu, Alberto Fraile, Niraj Gupta, Shivraj

Karewar for their wonderful friendship and support.

I acknowledge the financial support from the Center for Materials at Irradiation and Mechanical Extremes, an Energy Frontier Research Center funded by the U.S. Department of Energy, Office of Science, Office of Basic Energy Sciences under Award Number 2008LANL1026.

Lastly, I dedicate this thesis to my parents Guoming Zhang and Lingling Li, as well as my dear wife, Lili Wang. I love you all.

Contents

List of Figures

List of Tables

Chapter 1

Introduction

This Chapter motivates the importance of studying radiation-induced mixing at interfaces between metals with low solid solubility using computer simulations. The main structure of this thesis is also summarized.

1.1 Motivations

Reliable, safe, and economical nuclear energy systems require strong structural materials maintaining their mechanical, dimensional, and microstructural stability under harsh environments, combining the effects of high temperature, stress, corrosion, vibration, and an intense radiation field [1, 2]. For future generation's fission energy systems or future fusion reactors, structural materials are expected to perform in long-term service under higher temperature and more radiation intensive environment [3, 4]. Originally developed in the late 1950s and 1960s, many alloys currently used as structural materials in fission reactors will not be suitable in future advanced nuclear energy systems [5]. Therefore, the success of bridging the gap from the concepts of advanced nuclear power systems to reality relies on the development of high performance radiation-resistant materials [6].

One promising way to improve radiation resistance is to introduce a large number of interfaces as sinks to remove radiation-induced defects [7], e.g. by dispersing a high and uniform density of nanoscale oxide particles in steels [8, 9, 10] or by developing

nanocomposite materials [11, 12, 13]. Reducing microstructural dimensions increases radiation resistance as it shortens the average diffusion distance of radiation-induced defects to interfaces. In particular, a model system of nanolayered two-phase low solubility bi-metal composites has shown high strength [14], high thermal stability [15, 16] and superior tolerance to radiation damage [17, 13], including high levels of He [18, 19, 20]. Figure 1-1 shows under the same radiation conditions (200keV He, 3dpa, 450°C), numerous voids have been observed in nanocrystalline Cu, while almost no radiation damage is observed for nanolayered Cu-Nb composites [12].

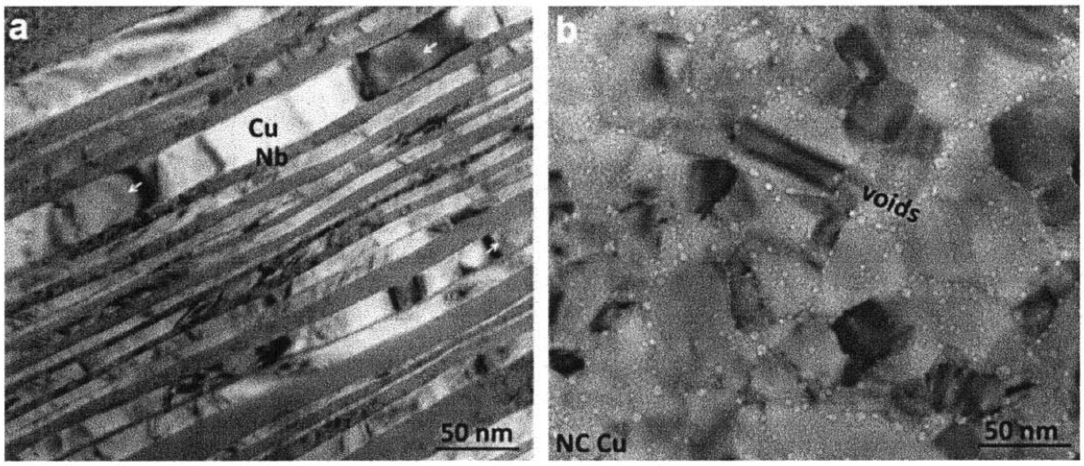

Figure 1-1: (a) Irradiated nanolayered Cu-Nb composites with 20 nm individual layer thickness are nearly void free. (b) Irradiation damage in nanocrystalline Cu under identical conditions. From [12].

However, materials containing large volume fraction of interfaces are inherently thermodynamically unstable: their energy may be lowered by complete intermixing, if they are composed of soluble elements, or by complete phase separation, if their constituents have low solid solubility.

In particular, multilayers of immiscible systems are morphologically metastable: they can only maintain their morphology under certain conditions, e.g. below certain temperature. For example, Figure 1-2 shows that the morphology of nanolayered Cu-Nb composites is stable at 600°C, but it rapidly coarsens and spheriodizes when annealing at 700°C for 1 hour [15].

Microstructural and compositional evolution towards thermodynamic equilibrium

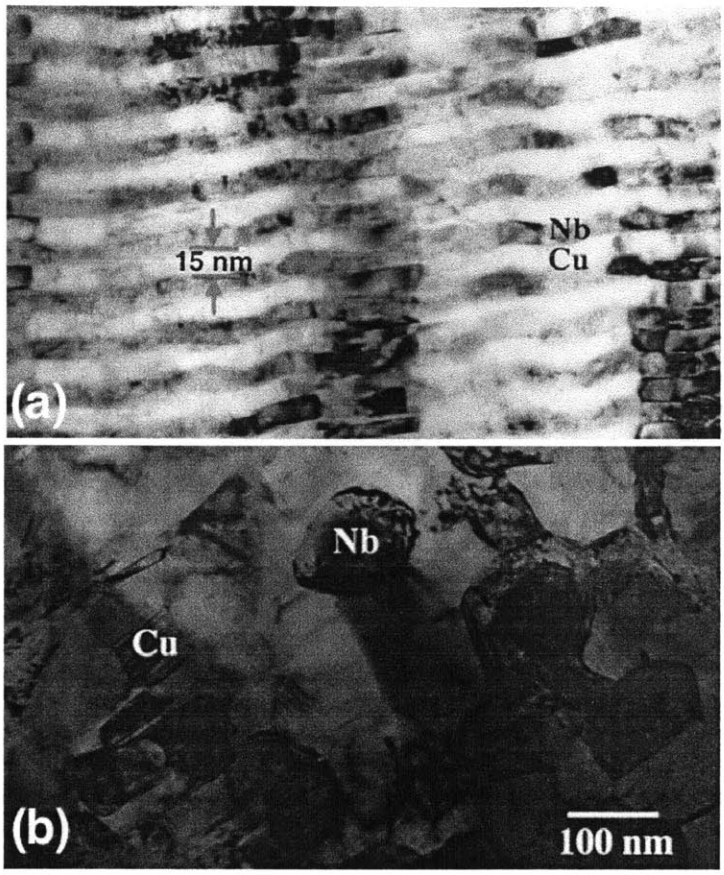

Figure 1-2: Microstructure of Cu-Nb multilayer annealing at (a) 600°C, 1 hour and (b) 700°C, 1 hour. From [15].

can be accelerated by irradiation [21, 22, 23, 24]. Thus, it is obvious to not design metallic interfaces with systems of large solid solubility or forming compounds, as rapid intermixing or formation of intermetallics would occur under irradiation [23, 24].

For metals of low solid solubility, the breakdown of their layered structures is often initiated by "pinch-off" mechanism: when one layer is penetrated by its neighboring layers, the discontinuous layer will rapidly coarsen, which eventually leads to spheriodization and complete phase separation (Figure 1-2). The pinchoff may be induced by thermal grooving [16] or radiation [25]. One example of pinchoff is shown in Figure 1-3.

Many experiments have shown that nanolayered composite composed of low solubility metals are morphologically stable under light ion radiation, such as He^+ [11, 27].

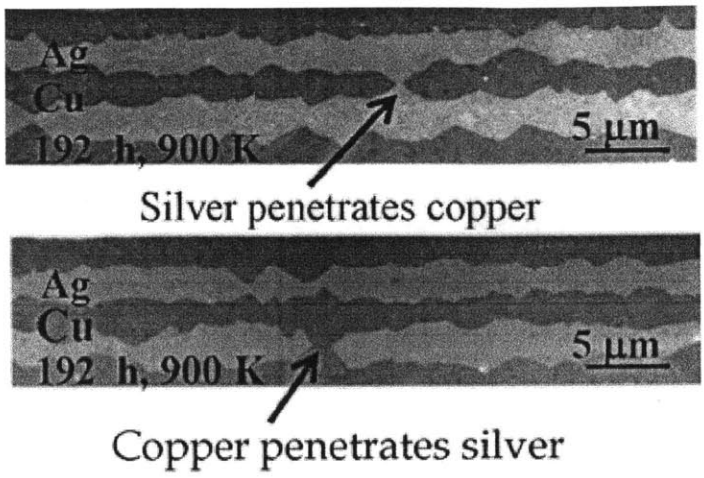

Figure 1-3: Scanning electron micrographs showing the pinchoff of Cu and Ag layers in a microlaminate, following a 192 h, 900 K anneal. From [26].

However, less is understood for their microstructural stability under heavy ion or neutron radiation. Instead of mainly creating point defects under light ion radiation, collision cascades will occur as a result of energetic heavy ion or neutron bombardment, which may lead to extensive intermixing.

Radiation-induced mixing across interfaces may initiate morphological instabilities that eventually lead to phase separation [25, 28]. Thus, to design radiation tolerant materials with improved microstructural stability, it is important to understand the detailed nature and factors that control radiation-induced mixing process. Previous studies have revealed many of the qualitative mechanisms affecting radiation-induced mixing [22, 29, 30]. Nonetheless, fully quantitative descriptions of some of these mechanisms have yet to be developed.

Thanks to the exponential growth of computing power, computer simulation has been an indispensible, powerful, and effective way to perform virtual experiments, discover new mechanisms, predict new materials structures, and characterize material performance. For example, first principle calculations provide important insight on the formation of stable Y-, Ti-, and O-rich nanoclusters in Fe-based alloys, which are enabled by pre-existing vacancy that lower the energy of the bound state [31]. Molecular dynamics has been a popular technique to study displacement damage

and formation of initial point defects and defect clusters in bcc and fcc materials [32, 33, 34]. Accelerated molecular dynamics was used to help reveal a new point defect recombination mechanism, i.e. interstitials re-emitted from grain boundaries to annihilate the vacancies in the bulk [35].

Computer simulation is particularly valuable to study radiation-induced mixing, because (1) radiation damage experiments are normally difficult to be set up, especially for high-energy neutron radiation, (2) experiments can hardly reach the temporal resolution of initial defect productions ($\sim 10^{-14} - 10^{-12}$ second), and (3) experiments cannot easily provide dynamic 3-D high spatial resolution of atomic structure to illustrate the radiation-induced mixing process. Computer simulations can be easily set up and excellently fit the time and length scale for radiation-induced mixing. In addition, it has the unique power to conduct various virtual experiments in different systems to validate or discover mechanisms that are impossible in experiments. Therefore, this research focuses on modeling radiation-induced mixing on isolated interfaces and multilayers, and its importance on morphological stability of nanolayered composites.

1.2 Thesis outline

The goal of this research is to better understand radiation-induced mixing between metals with low solid solubility, and investigate morphological stability of their nanolayered composites under heavy ion or neutron irradiation, with the aid of computer simulations. The model system that extensively studied throughout this thesis is nanolayered composite consisting of fcc-Cu and bcc-Nb.

Chapter 2 reviews the current understanding on initial radiation damage process, theories in the literature about radiation-induced mixing, and simulations that have been performed on radiation-induced mixing. Previous studies on morphological stability of layered structure are also reviewed. Basic computer simulation techniques that used in this research such as energy minimization and molecular dynamics are introduced in Chapter 3.

Current theories show that liquid phase thermodynamics is a key parameter to determine radiation-induced mixing. However, none of the currently available interatomic potentials can well describe liquid phase thermodynamics of Cu-Nb system. Thus, a new interatomic potential is developed, which is summarized in Chapter 4. Equilibrium binary phase diagram and liquid phase properties predicted by three Cu-Nb interatomic potentials are determined and compared in details in Chapter 5. The three interatomtic potentials have the same *solid* phase behaviors, but completely distinct *liquid* phase properties. They serve as a convenient set to study the effect of *liquid* phase properties on radiation-induced mixing unambiguously.

Chapter 6 describes the process of modeling radiation-induced mixing on isolated interfaces. Multiple collision cascades are performed to simulate mixing under continuous heavy ion or neutron radiation at cryogenic temperature. Effects of liquid phase thermodynamics and kinetics, interface crystallography, and ballistic displacement on radiation-induced mixing are investigated. An analytical expression for radiation-induced mixing at interfaces between low solubility metals is derived.

When the layer thickness decreases to a few nanometers, a single collision cascade may overlap several layers and layers may be pinched off by touching of perturbed neighboring layers. Chapter 7 presents radiation-induced mixing on multilayer nanocomposites. Enhanced intermixing when layer thickness is around 1nm is explained by overlap of diffusion zone inside thermal spike.

At elevated temperatures, after the initial defects production due to collision cascades, de-mixing will recover the intermixed interfaces due to thermally activated diffusion. Chapter 8 presents phase field modeling on the microstructural evolution of initially intermixed multilayers with different layer thicknesses. Morphological stability of multilayers under heavy ion or neutron radiation is investigated.

Finally, Chapter 9 summarizes the main contribution of this research, and discusses the implication of this study on better designing future radiation resistant materials. What remains to be further investigated is also discussed.

Chapter 2

Literature Review

This Chapter briefly reviews the basics on radiation damage process and current understanding on theories on radiation-induced mixing. A few examples of construction of interatomic potentials that reproduce experimental phase diagrams are also discussed. Previous simulation work on radiation-induced mixing and morphological stability of layered structures are summarized.

2.1 Radiation damage process

Radiation damage originates in the collisions between incident energetic particles and the target atoms. When energetic ion or atom travels through the lattice, energy may lose by elastic collisions [36, 37], electron excitation [38, 39], ionization [38, 39], or Bremsstrahlung [40, 39]. When energy is relatively low (less than ~0.1MeV), most energy loss is due to collisions between ions or nuclei through nuclear stopping, which would lead to displacement damage of target atoms [38]. The short-range repulsive interaction is proposed to be approximated by many screening functions, and a much used one is developed by Ziegler, Biersack and Littmark [41], which will be discussed in Section 3.1. When energy is relatively high (above ~0.1MeV), electronic stopping dominates and the nuclei will be less likely displaced from their lattice sites. If the energy of incident ions is in the MeV or GeV range, it is often referred as swift heavy ions, which can release sufficient energy to induce permanent damage-trails in many

amorphizing materials, named ion-tracks [42, 43]. This research focuses on the energy range where nuclear stopping dominates, and damage occurs by atomic displacement.

The incoming high-energy particles can be light ions (e.g. He, H), heavy ions (e.g. Xe, I, Cs), neutrons, or electrons split from fission reaction or radioactive decay [44]. In future fusion reactors, the main radiation damage to the structural materials comes from high-energy neutron and high level of He implantation [3]. The cross sections of heavy ion or neutron to target atoms are usually much larger than those of light ion or electron. Light ions or electrons will produce damage as isolated Frenkel pairs [1]. By contrast, heavy ions or neutrons will pass most of their kinetic energy to primary knocked-on atoms (PKAs), which will generate a branching cascade of additional knocked-on atoms that are displaced from their original lattice site. The collision cascade usually lasts for $\sim 10^{-11}$ seconds, leaving behind point defects and defect clusters [1, 34].

Collision cascade can be roughly divided into two stages: the ballistic phase and the thermal spike. During the ballistic phase, PKAs, like billiard balls, undergo high-energy two-body collisions with surrounding atoms, which consequently become displaced. The ballistic phase lasts for a few tenths of a picosecond and is followed by a thermal spike, in which the kinetic energy of the PKA is Boltzmann-distributed among all atoms in a localized volume [45]. The initial average temperature in a thermal spike is usually much higher than the melting temperature of the solids, forming a transient liquid droplet that quenches back down to nearly ambient temperature within a few picoseconds [34]. After the droplet resolidifies, it leaves behind defects such as vacancies and interstitials [46], point defect clusters [47], or antisite defects in ordered compounds [48].

The idea of thermal spike was first introduced by Brinkman in 1953 [49]. Seitz and Koehler [50] first calculated that diffusion might happen inside the thermal spike. Later in 1976, Vineyard [51] developed a theoretical model to calculate number of atomic jumps inside thermal spike by analytically solving the heat equation. Local melting inside thermal spike is first confirmed in 1987 using molecular dynamics simulation of 5KeV PKA in Cu [52].

The size and lifetime of collision cascade increase with the energy of incident heavy ion or neutron. When the incident energy is larger than 10KeV, several spatially distinguishable sub-cascades with lower PKA energy will be generated instead of a giant cascade [53, 54]. Although it has been reported that high-energy collision cascades have increasingly continuous structures and can create novel large defect clusters [55, 47], one may still reasonably assume that high-energy PKAs (>100KeV) will branch into a collection of lower energy sub-cascades.

In addition to initial high-energy ballistic collision and diffusion inside thermal spike, atoms can also be displaced by replacement collision sequence (RCS) mechanism in lattice structures, where one atom replaces the next along a closed-packed row when recoil energy is of the order of a few ten eV [56]. RCS of Open chain creates a vacancy at the first collisional lattice site and an interstitial after the last atom is at rest, while so-called closed chain RCS does not produce net defects. In either case, RCS may contribute a large amount of mixing [57]. The maximum length of RCS can be a few tens of nanometers, and it is insensitive to ambient temperature [58]. It is believed that most RCS happens before the thermal spike phase [53], creating a center core of vacancies surrounding by a distribution of interstitials [59, 53].

Another important mechanism of long-range atomic displacement is by transport of high-energy atoms (1-10keV) in almost force-free channels bordered by close-packed atomic chains [60]. The channeling effect is strongly dependent on their initial direction of motion and initial positions. For example, in fcc the traveling range is largest along ¡011¿ and can be a few hundred nanometers, while channeling cannot happen when the initial atom starts from a lattice site [61]. A review of theory and experiments on channeling effects can be found in [62].

The amount of displacement damage is often measured in unit of displacement per atom, dpa, which is environment independent. It is very convenient to use dpa to compare experiments at different conditions, i.e. high fluence of low-energy neutron radiation versus low fluence of high-energy neutron damage. A dose of one dpa indicates on average all the atoms in the system have been displaced from their original lattice sites as stable defects once. The internationally recognized standard

method for computing displacements is the Norgett-Robinson-Torrens (NRT) model [63]. Note that different models or standards may give very different number of displacements and defects. In particular, the number of Frenkel pairs measured in molecular dynamics simulations is usually a factor of 3-5 smaller than that predicted by NRT model [64], and the factor is often even larger when comparing molecular dynamics results with the famous Kinchin-Pease model [65]. To avoid the misleading comparisons of data reported in different simulations and experiments, Stoller *et al.* [66] proposed a standard on how dpa should be reported. In this thesis, we use the steps suggested in Ref. [66] to calculate the dpa level.

2.2 Theories on radiation-induced mixing

Radiation-induced mixing has been widely studied over the last 50 years [37, 67], in part due to its applications in alloy modifications [30, 68], fabrication of self-assembled nanocomposites [69, 21], and synthesis of amorphous solids [70]. It is also connected to fundamental process of defect production and displacement damage under irradiation [34].

Above a cohesive energy-dependent characteristic temperature [71], intermixing exhibits Arrenhius behavior because it is dominated by radiation-enhanced diffusion (RED) [67, 71]. Below the characteristic temperature, mixing is temperature independent because it is driven primarily be the high-energy processes occurring during collision cascades [72], and not subsequent thermally-activated phenomena.

Theoretical models of radiation-induced mixing at low temperature in the literature can be roughly divided into two categories: ballistic mixing models and thermal spike models. Ballistic mixing models are popular in the early 1980s, but later thermal spike models are more widely accepted because of their better explanations of experimental results.

Developed in late 1970s, ballistic mixing model views that mixing occurs primarily due to ballistic displacements of atoms, which can be characterized by introducing an effective diffusivity [73]. Later, Sigmund el al. described theoretical expressions for

relocation of impurities based on linear transport theory, suggesting that mixing is strongly dependent on the relative mass of two mixed species [74]. However, Cheng *et al.* [75] found that mixing rates differ substantially for metallic bilayers with similar mass ratios, but are instead correlated with Miedemas heats of mixing [76]. They proposed adding a Darken factor into the effective diffusivity to take into consideration the biased diffusion from chemical driving force [75].

In 1985, Van Rossum and his co-authors [77] reported that for bilayers with zero heats of mixing, radiation-induced mixing is inverse proportional to the square of average cohesive energy, implying that mixing happens mainly in the thermal spike. Based on Vineyards thermal spike model [51], Johnson *et al.* derived the phenomenological expression of mixing as a function of average cohesive energy and heat of mixing [22], while Nastasi and Mayer calculated liquid interdiffusivity from a hard sphere fluid model based on the kinetic theory of Enskog, and used it to explain the amount of mixing inside the thermal spike [45].

In studies on bilayers of metals with low solid solubility, Averback *et al.* showed that radiation-induced mixing at low temperatures is largely dependent on the miscibility of liquid phase [78]. For example, Cu-Nb and Cu-Bi, immiscible in solids but miscible in liquids, undergo intensive mixing upon Kr ion irradiation at 6K. By contrast, Cu-Mo, which is immiscible in both solids and liquids, shows minimal mixing under the same irradiation condition. Their model showed that in systems with large liquid heat of mixing, interdiffusivity could be negative, which leads to de-mixing inside the thermal spike and reversal of initial ballistic mixing [79]. However, their thermal spike model largely overestimates the amount of ballistic mixing [78], and it is not clear about the details of atomistic mixing and de-mixing in thermal spike. Full molecular dynamics simulations are desired to validate their theory or provide more insights on the differences of mixing rates in systems with low solid solubility. This is addressed in Chapter 6. In this study, we find mixing mostly occurs in the thermal spike by liquid phase interdiffusion, followed by partial de-mixing during the quench of thermal spike, regardless of liquid phase miscibility.

2.3 Interatomic potentials, liquid phase properties, and phase diagrams in binary systems

Since liquid phase properties are essential to radiation-induced mixing, it is critical to model thermal spikes based on interatomic potentials that well describe the liquid phase properties, such as heat of mixing, miscibility, and structures. However, there is no Cu-Nb interatomic potential in the literature suited for this purpose. As shown in Chapter 5, phase diagrams of two available Cu-Nb interatomic potentials constructed by Demkowicz [80] and Liu [81] completely disagree with the experimental phase diagram, especially in the liquid phase region. Therefore, a new Cu-Nb interatomic potential that well resembles both solid and liquid phase properties is desired.

Potentials for binary systems are usually developed by augmenting two single-element potentials with a cross-element interaction function fitted to quantities such as the dilute heats of mixing at zero temperature or properties of binary compounds, both real (investigated by experiments) and hypothetical (investigated by first-principles calculations) [82]. There is no guarantee, however, that a potential fitted to a limited number of solid-state properties will reproduce the whole phase diagram, especially the liquid phases.

Constructing phase diagrams of interatomic potentials is a resource-intensive task. Attempts to construct potentials that better reproduce phase diagrams of which we are aware have therefore not relied on direct fitting of the diagrams themselves. For example, in a recently developed Au-Si modified EAM (MEAM) potential, Ryu and Cai fitted first-principles data such as cohesive energies and bulk moduli of hypothetic alloy structures as well as substitutional impurity energies. They then further tuned angular cut-off parameters to better align with the experimental phase diagram [83].

Hoyt *et al.* fitted a Cu-Pb EAM potential to reproduce the experimental enthalpies of mixing as a function of composition of liquid phases [84]. The incomplete Cu-Pb phase diagram they calculated from this potential has a small liquid miscibility gap at about 200K below the melting temperature of Cu, which is in fair agreement with experiments. They did not, however, fit for two-phase coexistence in the solid state

nor did they investigate the mutual solid solubility of Cu and Pb.

The Cu-Ag phase diagram calculated with an EAM potential by Williams *et al.* is also in semi-quantitative agreement with experiments [85]. Rather than liquid phase enthalpies of mixing, their Cu-Ag cross-element interaction function is only fitted to the formation energy vs. volume curves of seven hypothetical compounds computed from first-principles at 0K. Their success indicates the possibility that immiscible metal potentials fitted to T=0K properties may be transferrable to high temperatures as well, including to liquid phases. The seven interatomic compounds they used, however, might not sample a sufficient range of atomic environments for metal pairs that are more dissimilar than Cu and Ag.

2.4 Simulations on radiation-induced mixings

Radiation damage and radiation-induced mixing have been extensively studied by binary collision approximation (BCA) and molecular dynamics (MD). BCA assumes that atoms are displaced by a series of elastic or quasi-elastic binary collisions under classical scattering kinematics [86]. BCA well describes the ballistic stage of high-energy collisions (above ~1keV), and it is very computationally efficient, in several orders of magnitude faster than MD. BCA is widely used in many standard codes to generate statistics of collision cascades [87] or RCS [88, 89]. Some of the BCA codes are structureless based on Monte-Carlo methods such as SRIM [90], and others can be applicable in crystal structures such as MARLOWE [91, 92].

However, BCA has many inherently shortcomings. The biggest problem is that the slowing down process of low energy atoms (¡1keV) is not accurately modeled, especially during the thermal spike phase when the diffusion of atoms is not governed by binary collisions, but affected by interactions of many neighboring atoms. BCA produces isolated Frenkel pairs when the energy of collided atoms is greater than threshold displacement energy, ignoring any recombination of vacancies and interstitials. Therefore, BCA often overestimates the number of Frenkel pairs, not to mention that it cannot produce complex defect structures such as defect clusters and

dislocations. Another drawback of BCA is that the angle dependent potentials cannot be incorporated in the scattering integral, thus it is unable to study covalently bonded materials like Silicon [93].

By contrast, MD incorporates many body interactions and it is well suited to the length and time scale of collision cascades. In fact, the first MD simulation was performed in 1960 by Gibson *et al.* to study the dynamics of low energy radiation damage in Cu [94]. The basics of MD are summarized in Section 3.2. The drawback of MD compared with BCA is computation time and limitation of system size [95]. However, with fast growing computation power, MD becomes more and more popular than BCA [34], from 400eV PKAs in systems of only 500 atoms in 1960 [94] to MeV PKAs in systems of billions of atoms recently [55, 96].

Numerous MD simulations have been done in studying radiation-induced mixing. They generally support the view that mixing occurs primarily through liquid phase diffusion inside thermal spikes [97], but also give additional insights. Gades and Urbassek showed that mixing rates are inversely proportional to the square of the cohesive energy and have a stronger than linear dependence on solid phase heats of mixing [98]. Nordlund and Averback reported an inverse Kirkendall effect at irradiated Cu/Co and Cu/Ni interfaces [99]. On the other hand, Sule *et al.* reported that mixing does not depend on chemical driving forces in Ti/Pt and Al/Pt bilayers [100], but seems to be highly dependent on the mass ratio between the overlayer and substrate [101]. They argued that the asymmetry of intermixing in the nearly equal mass Co/Ti system might be due to differences in atomic size [102].

Nevertheless, there appear not have been any MD studies aimed specifically at systematically investigating the effect of liquid phase properties on radiation-induced mixing. Moreover, previous MD studies have either used multiple low energy PKAs (e.g. 500 collision cascade with 0.5keV PKAs [103]) or small numbers of higher energy PKAs, corresponding to low doses [104, 97]. More work of multiple high-energy PKAs can be done to provide more information about the statistics and mechanisms of radiation-induced mixing. In Chapter 6, multiple high-energy collision cascades simulations are performed to investigate radiation-induced mixing, which is directly

comparable to experiments done under cryogenic temperature.

2.5 Morphological stability of layered structures

Layered composites, which can be fabricated by various techniques (e.g. physical/chemical vapor deposition, accumulative roll bonding), have been a class of most popular engineering structures with the ability to tailor layer thickness and interface structures to achieve enhanced materials properties. Recently, nanolayered composites of alternating immiscible metals such as Cu-Nb and Cu-Mo have shown orders of magnitude increase in strength [105, 106] and excellent radiation damage tolerance [11].

However, multilayers are prone to be morphologically instable, due to excess free energy from their large volume fraction of interfaces. Morphological instability may be initiated by high temperature annealing, or by various other driving forces, such as external stress or radiation. For example, Sridhar *et al.* showed that misfit between the neighboring layers may destabilize the layered structure by elastic stress-driven instability mechanism [107, 108]. Phase field modeling of microstructural evolution of multilayers indicate that volume fraction of certain phases is another important factor to determine the instability mode [109, 110].

For multilayers of miscible systems, interdiffusion across interfaces would break down the layered structures, leading to a uniform solid solution or intermetallics [24, 23, 111]. Since interdiffusion is almost inevitable at elevated temperatures, multilayers with miscible constitutes are always inherently instable, although they arose some interests because of their transient interface sharpening phenomenon [112, 113, 114].

For multilayers of immiscible systems at elevated temperature, interdiffusion is very small, especially for systems with large positive heat of mixing, so multilayers may be chemically stable. However, thermal grooving at columnar grain boundaries may result in pinch-off of layers [115, 116], followed by rapid evolution of the discontinuous layers to coarsening grains, which eventually leads to spheriodization and breakdown of layered structures [115, 117].

Thermal grooving often occurs at triple point junctions of columnar grain boundaries and interphase interface by diffusive mass transport [16]. The angle of thermal grooving is governed by the ratio of grain boundary free energies to interfacial free energies. When this ratio is large, triple-point junctions will groove deeper [118]. When the depth of the grooves is larger than layer thickness, pinch-off of layers occurs, followed by rapid spheriodization [15]. Wang and Anderson developed a 2-D grooving model to predict the time to pinch-off of multilayer based on initial morphology, free energies of interface and grain boundaries, and in-plane strain rate [119].

Thermal grooving is not always lead to microstructural instability it sometimes enhances microstructural stability of multilayer. For example, Misra *et al.* discovered that for Cu-Nb multilayer nanocomposites, thermal grooving of grain boundaries lead to the development of stable zig-zag alignment of triple-point junctions that anchor the layered structures [15, 16]. Recently, Wan *et al.* developed a model to explain the formation mechanism of the zig-zag microstructure and presented a multilayer stability map depending on aspect ratio of grain sizes, free energies of interface and grain boundaries, and initial stacking of grains [120, 121].

It is now well known that multilayers of bi-metals with low solid solubility such as Cu-Nb and Cu-Mo are morphological stable under light ion irradiation. Their interfaces remain chemically abrupt after He ion irradiation, indicating that ballistic mixing is reversed by thermally activated de-mixing [17, 11, 122]. However, less is known about the morphologically stability of multilayer under heavy ion irradiation [25]. Extensive mixing inside thermal spike may lead to pinch-off of layers, especially when the core of thermal spike overlaps several alternating layers. In Chapter 7 and 8 of this research, simulation results indicate that multilayer nanocomposites will be morphologically stable when layer thickness is above 2-4nm.

Chapter 3

Methodology and Simulation Tools

This Chapter briefly introduces the basics of the simulation techniques that have been used through out the thesis. Static calculations are used in Chapter 4 to construct a Cu-Nb EAM potential. Molecular dynamics simulations are implemented in Chapter 5 to study liquid phase properties and in Chapter 6 and 7 to model collision cascade process. Semi-grand canonical Monte Carlo simulations are used in Chapter 5 to determine the liquid phase miscibility gap. Finally, phase field simulations are implemented in Chapter 8 to model the microstructural evolution of multilayer nanocomposites after collision cascade.

3.1 Static calculations

In atomistic simulations where the positions of atomic nuclei are explicitly specified, the total potential energy of the system is usually obtained by conducting *ab initio* calculations that directly solve Schrodingers equation under a set of approximations, such as density functional theory (DFT) used in Section 4.3, or by empirical potential approximations that widely used in molecular dynamics and Monte-Carlo simulations. The properties calculated by *ab initio* methods are of great precision and computational costs, and therefore they usually serve as benchmark to develop empirical potentials, which are less accurate but with significantly less computational costs. This research focuses on modeling of radiation-induced mixing process, which

requires to affectively describing the dynamics of atomic transport and diffusion under irradiation. Therefore, empirical potential is used to approximately model the metallic system of interest.

In metallic systems, there is no covalent bond and the empirical potential is usually assumed to be a function of atomic pair-wise interactions, neglecting contribution from interactions of triples, quadruplets, etc. The popular form of empirical potential in metallic system is the embedded atom method (EAM) potential [123], as discussed in Chapter 4. In this thesis, all empirical potentials are in EAM form.

Potential energy minimization (PEM) is used in Section 6.4.3 to get rid of density fluctuation from thermal spike induced pressure wave. At each snapshot, the kinetic energy of every atom is entirely removed, and atoms move to new positions iteratively until the total potential energy reaches local minima in the potential energy landscape. The popular algorithms of PEM are steepest descent, Newton-Raphson, or conjugate gradient methods [124]. All these methods are iterative: move each atom towards certain direction at certain distance, then update the directional information based on the new configuration, until the system reach local minima. In this thesis, I use conjugate gradient method, because it is generally faster than steepest descent, and easier to converge than Newton-Raphson. The basic steps of conjugate gradient methods that used in this study are summarized below.

Assume at the i^{th} cycle of the iterative, the system is at $x_{(i)}^{3N}$ where the position vector x^{3N} is in 3N dimensions representing the coordinates of all atoms, and $x_{(i)}^{3N}$ is their corresponding force vectors. Assuming the potential energy of the system is $U(x_{(i)}^{3N})$ at step i, atoms are moved towards $d_{(i)}^{3N}$ by $\alpha_{(i)}$. The iterative steps of conjugate gradient PEM are [124]:

1. The initial step – use atomic forces as initial directions: $d_{(0)}^{3N} = F_{(0)}^{3N} = -\nabla U(x_{(i)}^{3N})$
2. Find $\alpha_{(i)}$ that minimize potential energy: $U(x_{(i)}^{3N}) = U(x_{(i)}^{3N} + \alpha_{(i)} d_{(i)}^{3N})$
3. Update position of all atoms: $x_{(i+1)}^{3N} = x_{(i)}^{3N} + \alpha_{(i)} d_{(i)}^{3N}$
4. Update the new force: $F_{(i+1)}^{3N} = -\nabla U(x_{(i+1)}^{3N})$

5. Calculate $\beta_{(i+1)} = \max\{\frac{(F^{3N}_{(i+1)})^T(F^{3N}_{(i+1)}-F^{3N}_{(i)})}{(F^{3N}_{(i)})^T F^{3N}_{(i)}}, 0\}$

6. Update the moving directions: $d^{3N}_{(i+1)} = F^{3N}_{(i)} + \beta_{(i+1)} d^{3N}_{(i)}$

7. Go to step 2, until converge on $U(x^{3N}_{(i+1)})$

In step 2, $\alpha_{(i)}$ is obtained by line minimization algorithm: first bracketing a minimum in a range $(\alpha^{\min}_{(i)}, \alpha^{\max}_{(i)})$, and then gradually shrink this range to converge to the minimum by iterative parabolic interpolation [125]. When the configuration is far from a local minimum, the minimization direction d^{3N} needs to be reset to force direction (step 1) periodically. The criteria of restarting conjugate gradient PEM is when the conjugate directions lose their conjugacy: $\frac{(F^{3N}_{(i+1)})^T F^{3N}_{(i)}}{(F^{3N}_{(i)})^T F^{3N}_{(i)}} > 0.2$ [124].

3.2 Molecular dynamics

Molecular dynamics (MD) is a standard simulation technique to model initial defect production and intermixing under collision cascades. In MD simulations, the interactions of atoms are governed by empirical potentials and atoms move by integrating Newtonian equations of motion using a finite difference scheme such as Gear predictor-corrector [126]. All MD simulations in this Thesis were conducted using LAMMPS atomistic modeling code [127]. Visualizations were performed using OVITO [128] and Atomeye [129].

The integration time step Δt should be chosen small enough to maintain numerical accuracy, while at the same time should be as large as possible to be computationally efficient. During collision cascade process, the kinetic energy of fastest atom decreases a few orders of magnitude within tens of picoseconds, from initial PKA of 100keV to thermalized distribution with average kinetic energy less than 0.1eV. In our simulations, the time step is always less than 0.01ps and it is dynamically varying such that the maximum distance for an atom to move within one time step is less than 0.1Å. Then, the time step is very small in the initial ballistic phase, and gradually increase to reach maximum by the end of thermal spike.

3.3 Semi-grand canonical Monte Carlo

Semi-grand canonical Monte Carlo (SGC-MC) method is used to determine the liquid phase miscibility gap, which is relatively difficult to be obtained directly from free energy calculations. We carried out the simulation based on a scalable parallel Monte Carlo code developed by Sadigh *et al.* [130].

Consider a binary system with configuration (x^{3N}, σ^N), where x^{3N} is the position vector in $3N$ space, and σ^N is a N dimensional vector with values of 0 and 1 indicating two different atom types. In a SGC ensemble, the system is in contact with a reservoir at constant temperature and chemical potential for each species, while the total number of atoms is conserved. The partition function of SGC ensemble at temperature T can be expressed as

$$Z_S(\Delta\mu, N) = \int_0^1 Z_C(c, N) \exp(-\beta \Delta\mu N c) dc, \tag{3.1}$$

where $\Delta\mu$ is chemical potential difference, c is concentration of atom type 1, and $Z_C(c, N)$ is the partition function for the canonical ensemble at temperature T, which can be written as

$$Z_C(c, N) = \frac{\int \exp\left(-\beta U(x^{3N}, \sigma^{3N})\right) d^{3N}x}{\Lambda_1^{3(N-n)} \Lambda_2^{3n} n!(N-n)!}, \tag{3.2}$$

where $\Lambda_i = \sqrt{h^2/2\pi m_i k_B T}$ and $\beta = 1/k_B T$. The Monte Carlo algorithm coupled with MD to sample SGC ensemble in (3.1) can be described as follows [130]:

1. Randomly select an atom.
2. Switch its chemical identity (from 0 to 1, or from 1 to 0).
3. Calculate the change in potential energy ΔU and concentration Δc.
4. Accept the change of atom type in step 2 with probability $\min\{1, \exp\left(-\beta(\Delta U + \Delta\mu N \Delta c)\right)\}$.
5. Run MD for a small number of time steps to relax the system.

6. Return to step 1, stop if the system reaches equilibrium.

The importance of SGC-MC is that the acceptance probability depends on chemical potential difference $\Delta\mu$. As shown in Section 5.2, single equilibrium phase is obtained by varying $\Delta\mu$, and then the liquid phase miscibility gap is extrapolated from hysteresis of equilibrium concentration versus $\Delta\mu$ curves.

3.4 Phase field simulation

Classical MD simulations can only reach the time scale up to a few nanosecond, insufficient to study microstructure evolution of multilayer nanocomposites at elevated temperatures which usually lasts for hours or days. Phase field simulation has been a powerful method in modeling and predicting morphological and microstructure evolutions [131], and in studying deformation and defects [132]. In this study, we adopt a simple phase field model to investigate the morphological stability of nanolayered structures.

We use local volumetric concentration ϕ as a conservative parameter. The free energy density is assumed to be a function of local concentration and its gradient

$$f(\phi, \nabla\phi) = f^{hom}(\phi) + K|\nabla\phi|^2 \tag{3.3}$$

where $f^{hom}(\phi)$ is the homogenous free energy density, which is usually expressed as a double well function, and K is gradient-energy coefficient, which relates the characteristic width of interface δ and interfacial energy per unit area γ by [133]

$$\delta \approx \sqrt{K/\Delta f^{hom}_{\max}}, \tag{3.4}$$

$$\gamma \approx \sqrt{K\Delta f^{hom}_{\max}}\Delta\phi, \tag{3.5}$$

where $\Delta f^{hom}_{\max}$ is the maximum value of increments in free energy density relative to a homogeneous system at equilibrium separated by $\Delta\phi$.

The temporal and spatial evolution of the conserved parameter ϕ is governed by

Cahn-Hilliard nonlinear diffusion equation [134, 135, 136]:

$$\frac{\partial \phi}{\partial t} = \nabla \cdot \left(\frac{\tilde{D}}{\partial^2 f^{hom}/\partial \phi^2} \nabla \left(\frac{\partial f^{hom}}{\partial \phi} - 2K\nabla^2 \phi \right) \right) \tag{3.6}$$

where $\tilde{D}$ is the interdiffusion coefficient. In this thesis, the Cahn-Hilliard equation is solved in a finite element code COMSOL [137].

Chapter 4

Development of Interatomic Potential

In this Chapter, a Cu-Nb potential is fitted to the enthalpies of mixing at T=0K determined from first-principles calculations across the whole composition range for both bcc and fcc Cu-Nb solid solutions. Verification of transferability to liquid phase of this newly constructed potential will be discussed in Chapter 5.

4.1 Fitting strategy of Cu-Nb EAM potential

We construct our Cu-Nb potential based on the embedded atom method (EAM) format [123, 138]. Both EAM and the closely related Finnis-Sinclair (F-S) potentials [139] have proven sufficiently accurate and efficient to be of significant utility in studying fcc and (to a lesser degree) bcc metals [140, 141, 142]. The total energy of an EAM system consists of two terms: the embedding energy F_{α_i} and a pair-wise interaction energy $V_{\alpha_i\alpha_j}$, as expressed below,

$$E_{total} = \sum_i \left[F_{\alpha_i} \left(\sum_{j \neq i} \rho_{\alpha_j}(r_{ij}) \right) + \frac{1}{2} \sum_{j \neq i} V_{\alpha_i \alpha_j}(r_{ij}) \right]. \tag{4.1}$$

Subscript α_i represents the type of atom with index i, ρ_{α_j} is the electron density function of atom type α_j and r_{ij} is the distance between atoms i and j.

We start from a pure Cu EAM potential by Mishin *et al.* [143] and a pure Nb FS potential developed by Ackland and Thetford [142]. The Cu potential we chose predicts properties of crystal structures comparably well to another widely used Cu EAM potential by Voter [140], but reproduces lattice defect energies as well as interactions between atoms at close range with better accuracy, which is important in studies of materials under irradiation.

A Nb EAM potential that performs comparably well could not be found in the literature. First-principles calculations show that the lowest energy self-interstitial in bcc Nb is the <111>-split dumbbell [144], a property that is reproduced only in the potential by Derlet *et al.* [145]. Johnson and Oh's Nb potential predicts <100>-split dumbbells as the most stable self-interstitial structure [80, 141] and Ackland's the <110>-split dumbbell [142]. The lowest self-interstitial energy in the latter, however, is less than 1eV lower than the value from first-principles calculations [144], compared to more than 2eV lower in the former. The mechanical properties of Ackland Nb have been further assessed in a separate study concerned with shock compression, which is another important research area for Cu-Nb multilayer nanocomposites [81], and were found to be superior to those of five other EAM and F-S type potentials [146]. We therefore chose the Ackland Nb potential as the best compromise between mechanical and point defect properties among the available options.

Certain transformations of the embedding and pair interaction functions that do not alter the energies of pure element EAM potentials but do influence the energies of multi-component systems have traditionally been used in constructing binary potentials [80]. To simplify the fitting procedure, we adopt the following transformations discussed by Caro *et al.* [147] to minimize the embedding function contribution to the enthalpy of mixing:

$$\rho_\alpha(r) = \rho^0_\alpha(r)/\varrho^0_{\alpha,eq}, \tag{4.2}$$

$$F_\alpha(\rho_\alpha) = F^0_\alpha\left(\rho^0_\alpha(r)\right) - F^{0\prime}_\alpha\left(\varrho^0_{\alpha,eq}\right)\rho^0_\alpha(r), \tag{4.3}$$

$$V_{\alpha\alpha}(r) = V^0_{\alpha\alpha}(r) + 2F^{0\prime}_\alpha\left(\varrho^0_{\alpha,eq}\right)\rho^0_\alpha(r). \tag{4.4}$$

Here, superscript 0 denotes original functions and $\varrho^0_{\alpha,eq}$ is the original average electron

density on a lattice site when the system of fcc Cu or bcc Nb is at equilibrium at 0K:

$$\varrho^0_{\alpha,eq} = \sum_{j \neq i} \rho^0_\alpha (r_{ij}) \,. \tag{4.5}$$

The equilibrium density per atom in fcc Cu or bcc Nb in this effective representation is always unity at 0K, eliminating the first-order contribution of the embedding term to the enthalpy of mixing for alloys [147]. Thus, the only remaining task is to fit the Cu-Nb cross-element interaction function, V_{AB}, without need of changing any of the other functions.

We fit our cross-element interaction function to the $T = 0K$ enthalpies of mixing of random fcc and bcc alloys across the entire composition range of Cu and Nb. Strains and atomic positions in such structures may be relaxed using standard atomistic modeling techniques. Such relaxations, however, are time-consuming and make parameter fitting inefficient. We therefore use an approximate model of random alloys by Ackland and Vitek [148] to calculate the average energy for randomly mixed but not fully relaxed crystal structures. For an EAM system with either species A or B occupying site i, the energy per atom ε_{rand} can be written as

$$\varepsilon_{rand} = x_A^2 \sum_j V_{AA}(r_{ij}) + x_B^2 \sum_j V_{BB}(r_{ij}) + 2x_A x_B \sum_j V_{AB}(r_{ij}) + x_A F_A(\tilde{\rho}) + x_B F_B(\tilde{\rho}). \tag{4.6}$$

where $\tilde{\rho}$ is the average density on a lattice site contributed by neighboring A and B atoms, defined as $\tilde{\rho} = x_A \sum_j \rho_A(r_{ij} + x_B \sum_j \rho_B(r_{ij}$. The enthalpy of mixing per atom is

$$\Delta h_{mix} = \varepsilon_{rand} - (x_A \varepsilon_A + x_B \varepsilon_B) \,, \tag{4.7}$$

where x_A and x_B are concentrations of A, B atoms and ε_A and ε_A are energies per atom of pure elements in the same phase as the alloy. The lattice constants a of the alloy structures are interpolated between the lattice constants of Cu and Nb in either fcc or bcc phases using Vegard's law: $a = x_{Nb} a_{Nb} + x_{Cu} a_{Cu}$.

We use the following form to fit V_{AB} for Cu and Nb interaction:

$$V_{AB}(r) = \begin{cases} \sum_{i=-7}^{2} c_i r^i \left(r - r_{cut}\right)^2 & \text{for} \quad r < r_{cut} \\ 0 & \text{for} \quad r \geq r_{cut} \end{cases}, \tag{4.8}$$

where c_i are constants to be determined and r_{cut} is the cutoff radius beyond which the interaction energy is set to zero. The ten fitting parameters $c_{i=(-72)}$ give enough degrees of freedom to avoiding pre-determining shape of the cross potential V_{AB}. With this representation of V_{AB}, the enthalpy of mixing in bcc and fcc phases at $0K$, Δh_{mix}^{bcc} and Δh_{mix}^{fcc}, may be calculated as a function of concentration.

To obtain the values of c_i that parameterize V_{AB}, we minimize a cost function that measures the difference between the enthalpies of mixing in bcc and fcc alloys obtained from our potential and target functions from first-principles calculations. The cost function we try to minimize is

$$\chi = \sum_{x_i=0}^{1} \left[w(x_i) \left(\Delta h_{mix}^{fcc}(x_i) - \Delta h_{DFT}^{fcc}(x_i) \right)^2 + \left(\Delta h_{mix}^{bcc}(x_i) - \Delta h_{DFT}^{bcc}(x_i) \right)^2 \right], \tag{4.9}$$

where $w(x)$ is a weight function

$$w(x) = \frac{1}{2} \left[1 - \tanh\left(8\pi(x - 0.14)\right) \right], \tag{4.10}$$

used to target Cu-rich fcc alloys for reasons that will be explained in the next subsection. We use Gauss-Newton methods to find the unconstrained local minimum with multi-variables [124]. Since the cost function may have multiple local minima, the 10 c_i parameters are highly dependent on their initial values and may have multiple solutions after optimization, many of which might not have a form describing physically realistic pair interactions. Thus, we choose initial values of c_i that give V_{AB} closest to the average of V_{AA} and V_{BB} by minimizing the cost function,

$$\chi_0 = \sum_{r_i=r_a}^{r_{cut}} \Delta r \left[V_{AB} - \frac{1}{2} \left(V_{AA}(r_i) + V_{BB}(r_i) \right) \right]^2, \tag{4.11}$$

r_a in (4.11) is the cutoff of a short-range repulsive region, which will be described in Section 4.4. Using these c_i as initial values, we obtain a $V_{AB}(r)$ that reproduces the enthalpies of mixing for both bcc and fcc alloys and has a physically reasonable form.

4.2 Fitting target: enthalpies of mixing

Liquid phase miscibility is governed by free energies of formation of liquid phases, which are expensive to obtain from first-principles. In this study, therefore, we use the enthalpies of formation in solid phases at zero temperaturewhich are considerably easier to determineas a target for potential fitting, with the hope that the potential thereby obtained will nevertheless accurately model the liquid portion of the Cu-Nb phase diagram without directly fitting to the experiments.

Cu and Nb form no stable compounds in any part of the composition range, and fcc-Cu and bcc-Nb are almost immiscible. To obtain a extensive and relevant database of properties to fit, we have computed the enthalpies of mixing of the Cu-Nb alloy in bcc and fcc random solid solutions over the entire composition range using density functional theory (DFT) as implemented in the SIESTA code [149]. The calculations are spin non-polarized and use the local density approximation (LDA) with the Ceperly-Alder parametrization [150]. Core electrons are replaced by nonlocal norm-conserving pseudopotentials. Valence electrons are described by linear combinations of numerical pseudoatomic orbitals [151].

The maximum cutoff radius for the Cu pseudopotential is set to 1.47Å, and its basis set consists of two localized functions for the 4s and five for the 3d states. The cutoff radii are 4.14Å and 2.51Å, respectively. The equilibrium resulting lattice parameter for the fcc phase is 3.61Å, close to the experimental value of 3.60Å. The bcc phase lattice parameter is 2.87Å. For the Nb pseudopotential the maximum cutoff radius is set to 1.05Å, and its basis set consists of two localized functions for the 4s and 5s states, three localized functions for the 4p and 5p states and five for the 4d states. The cutoff radii are 3.7Å, 3.29Å, 3.42Å, 3.40Å and 3.83Å, respectively. The lattice parameter found for pure Nb in the bcc phase was 3.24Å, 1.8% lower than the

experimental value of 3.30Å. In the fcc phase the calculated lattice parameter was 4.16Å. Enthalpies of mixing were calculated in bcc supercells containing 128 atoms while a supercell with 108 atoms was employed for fcc structures. We have converged the k-point grid to a 3x3x3 mesh and the Methfessel-Paxton broadening scheme [152] was used with a 0.3 eV width.

The enthalpies of mixing in bcc and fcc phases at various concentrations are calculated based on (4.7). Configurations at different concentrations were generated following the special quasi-random structure (SQS) methodology [153], which generates supercells that have the lowest possible short-range order and are therefore the best representative configurations of a random solid solution. As described in the previous section, the lattice parameter for each configuration was taken following Vegard's law. We ran two types of simulations: one relaxing only the electronic structure and the second relaxing atomic positions and system strains at constant zero stress. The results are shown in Figure 4-1(a). We represent these curves using a Redlich-Kister expansion [154] to first order in the concentration:

$$\Delta h_{mix}(x) = x(1-x)\left[a + b(1-2x)\right]. \tag{4.12}$$

The bcc solid solution remains stable across the entire composition range, so the bcc enthalpy of mixing curve was used directly in the fitting procedure. By contrast, the fcc phase rich in Nb is unstable. Indeed, for calculations at constant stress the system undergoes a phase transformation from fcc to tetragonal. In the case of just one Cu atom in fcc Nb, the y axis contracts by about 21.5% while the x and z axes expand by about 10.8%. This instability was verified using a more robust ultrasoft pseudopotential [155, 156] DFT method implemented in the VASP code [157, 158]. DFT simulation of a fcc supercell containing one Cu atom in 107 Nb atoms allowing both cell shape and volume change results in a face-center-tetragonal structure.

The Cu rich side of fcc solutions, however, is stable below 20%-at Nb. Therefore, the final target function we use weights the fcc enthalpy of mixing curve as described

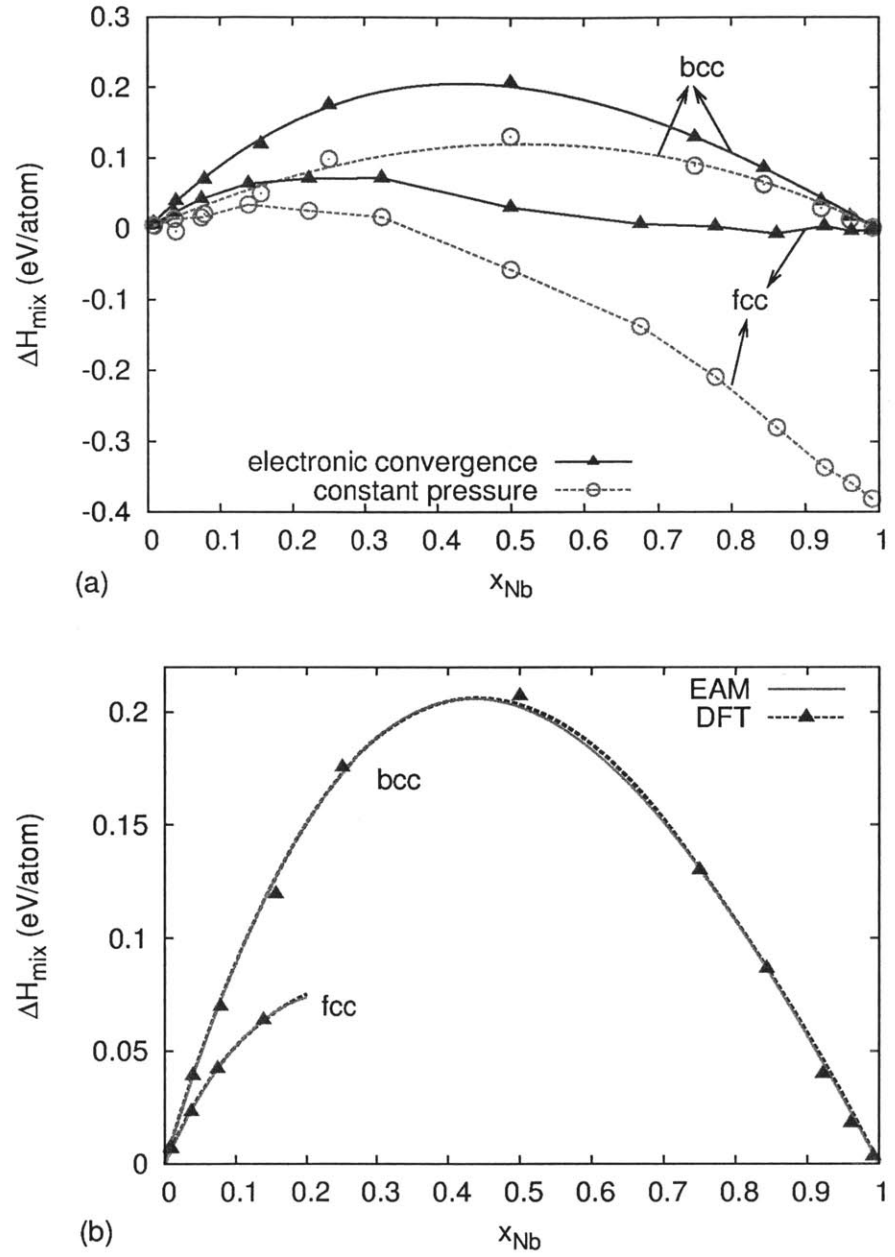

Figure 4-1: Enthalpies of mixing at $T = 0K$ for (a) bcc and fcc Cu-Nb solid solutions obtained from first-principles calculations. The fcc phase rich in Nb is unstable under constant pressure relaxation. In (b), enthalpies of mixing for bcc and fcc solid solutions obtained from the newly constructed EAM potential are shown to have excellent agreement with the DFT data.

in the previous subsection so that only the stable range is fitted. For bcc solutions, the coefficients in (4.12) used to fit enthalpies of mixing are $a = 0.8085, b = 0.2243$; and for fcc solutions below 20%-at Nb, $a = 0.1081, b = 0.5882$. Figure 4-1(b) compares the $T = 0K$ enthalpies of mixing calculated from our fitted EAM potential to the target functions described above, demonstrating excellent agreement.

4.3 Short-range repulsive potential

In simulations of irradiation, high kinetic energy (>1keV) particles may approach target atoms at distances orders of magnitude shorter than the equilibrium lattice spacing. A two-body repulsive potential developed by Ziegler, Biersack and Littmark (ZBL) [41] has proven useful for describing these short-range interactions. The ZBL potential is intended for atomic separations "r" of no more than a few Bohr radii, so we join it to the pair-interaction functions of our EAM potential by fitting a spline

$$V_s(r) = a_0 + a_1 r^{-1} + a_2 r^{-2} + a_3 r^{-3} \tag{4.13}$$

over a range $r_a < r < r_b$. The coefficients a_0, a_1, a_2 and a_3 are required to satisfy $V_s(r_a) = V_{ZBL}(r_a)$ and $V\prime_s(r_a) = V\prime_{ZBL}(r_a)$ at $r = r_a$ as well as $V_s(r_b) = V_{EAM}(r_b)$ and $V\prime_s(r_b) = V\prime_{EAM}(r_b)$ at $r = r_b$. Separate splines are fitted for all three pair potentials V_{AA}, V_{BB} and V_{AB}, but in all cases $r_a = 1$Å and $r_b = 2$Å.

To eliminate the contribution of the embedding term in the total energy when the interaction is governed by ZBL, we require the electron density function and its derivative to reduce to zero at $r = 0$. This is accomplished by a spline at $r < r_b$ of the form

$$\rho_s(r) = b_2 r^2 + b_3 r^3 \tag{4.14}$$

where b_2 and b_3 are determined by satisfying $\rho_s(r_b) = \rho_{EAM}(r_b)$ and $\rho\prime_s(r_b) = \rho\prime_{EAM}(r_b)$ at $r_b = 2$Å. Figure 4-2 shows the final embedding, electron density, and pair interaction functions for our newly constructed Cu-Nb EAM potential. The fitting coefficients for the Cu-Nb interaction function and ZBL spline fits are listed in

Appendix A. Table 4.1 lists lattice parameters, cohesive energies per atom, bulk moduli, and heat of formation of four hypothetical compounds computed using the fitted potential. These values are also listed for checking when others try to implement this potential. As expected, none of these compounds appear in the equilibrium phase diagram. All these hypothetical compounds have positive heat of formation and are thermodynamically unstable at $T = 0K$.

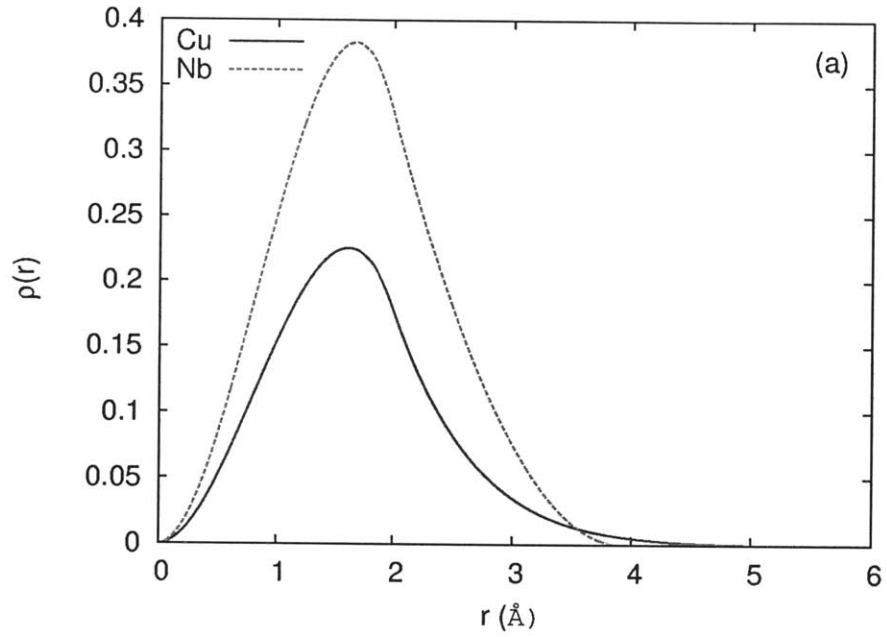

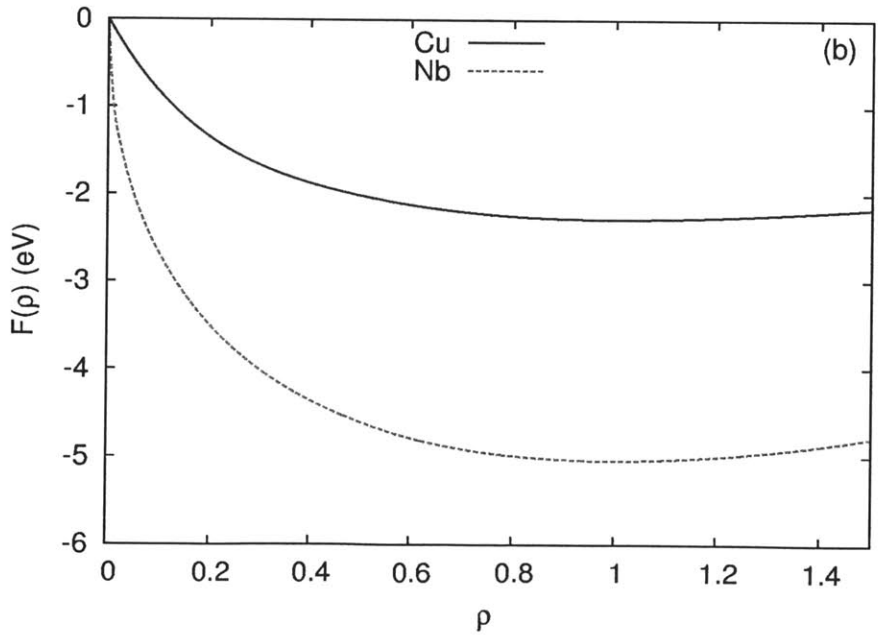

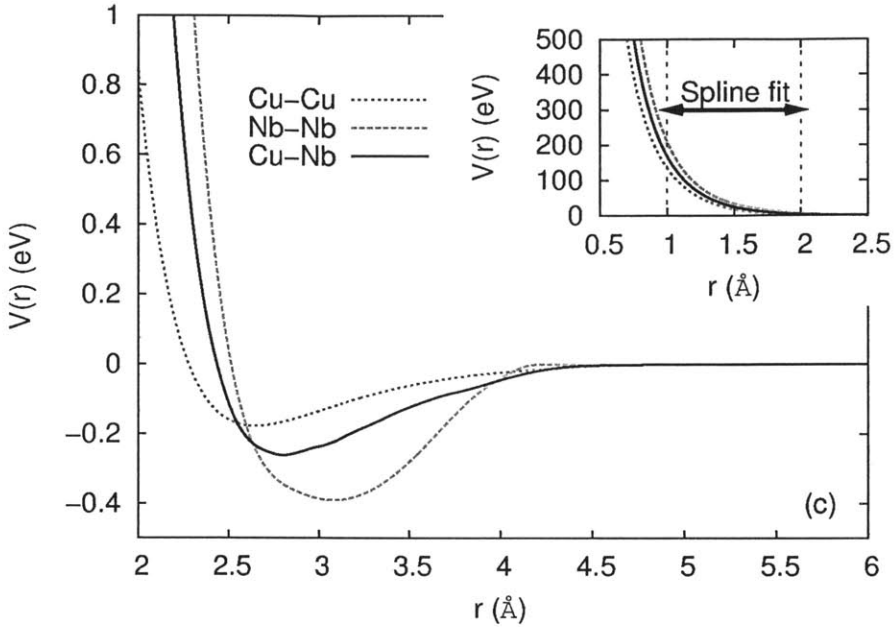

Figure 4-2: Final EAM potential functions: (a) Cu and Nb electron density functions; (b) embedding functions for Cu and Nb; (c) pair interaction functions between Cu-Cu, Nb-Nb, and Cu-Nb. The inset in (c) shows the spline fit between the EAM pairwise interaction functions and ZBL.

4.4 Comparison of three EAM potentials

From now on, the newly constructed Cu-Nb EAM is named EAM1. There are two other Cu-Nb EAM potentials available in the literature: one due to Demkowicz and Hoagland [80] (named EAM2), and the other one constructed by Liu *et al.* for shock compression simulations of Cu-Nb multilayer (named EAM3, see ref. [159, 146]). These potentials were constructed starting from different single-element potentials and used different strategies to fit cross-element interactions. These differences are summarized in Table 4.2. The differences in liquid phase properties and phase diagrams among three potentials are summarized in Chapter 5.

Table 4.1: Summary of lattice constants (a), cohesive energy per atom (E_{coh}), bulk moduli (B), and heat of formation (ΔH_f) of four hypothetical compounds calculated with the fitted Cu-Nb potential.

Structure	a(Å)	E_{coh} (eV)	B (GPa)	ΔH_f(eV)
CsCl ($B2$)	3.130	-5.401	181.0	0.154
CuAu ($L1_0$)	3.862	-5.339	150.2	0.216
Cu3Au ($L1_2$), 25%Nb	3.750	-4.415	168.7	0.133
CuTi3 ($L6_0$), 75%Nb	3.983	-6.283	136.9	0.279

Table 4.2: Summary of construction of the three different Cu-Nb EAM potentials. EAM1 is fitted to ΔH in fcc/bcc solid solution. EAM2 and EAM3 are fitted to dilute heats of mixing, and lattice constant and bulk modulus of CsCl structure.

	EAM1	EAM2	EAM3
Cu-Nb potential	Present study	Demkowicz [80]	Liu [159]
Cu Potential	Mishin [143]	Voter [140]	Voter [140]
Nb Potential	Ackland [142]	Johnson [141]	Ackland [142]

Chapter 5

Phase Diagrams and Liquid Phase Properties

This Chapter verifies that the potential so constructed is transferrable to liquid phases by determining its complete phase diagram. We compare it to ones obtained from experimental data and phase diagrams obtained from two other Cu-Nb EAM potentials. Finally, we investigate the thermodynamic properties and structures of the Cu-Nb liquids predicted by all three potentials. We find that our new potential most accurately reproduces the complete Cu-Nb phase diagram and also predicts that the equilibrium liquid is a single phase with distinct compositional patterning over lengths of approximately 2nm.

5.1 Free energy calculation

To obtain phase diagrams from potentials, we calculate the Gibbs free energy curves for different phases as a function of temperature and composition and then construct the common tangent lines among them. To calculate free energies, we use a thermodynamic package that implements the methodology described by (5.1-5.17) below, as described in [160, 161]. In the following descriptions, we do not distinguish the Gibbs free energy and Helmholtz free energy, since they are the same under the conditions of our simulations, namely zero pressure. Internal energy and enthalpy are also equal

at zero pressure.

In addition to enthalpy, free energy has a temperature-dependent entropy contribution that cannot be calculated directly from the potential. Free energy per atom $f(T)$ may nevertheless be obtained using the Gibbs-Duhem integral,

$$f(T) = f(T_0)\frac{T}{T_0} - T\int_{T_0}^{T} \frac{h(\tau)}{\tau^2} d\tau, \tag{5.1}$$

where $f(T_0)$ is the free energy per atom at a reference temperature T_0 and $h(\tau)$ is the enthalpy per atom as a function of temperature, τ. The task of finding $f(T)$ for any temperature may therefore be reduced to (a) obtaining the enthalpy as a function of temperature, which is straightforward in MD, and (b) calculate the free energy at the reference temperature T_0.

Figure 5-1 shows an example of the enthalpy as a function of temperature for pure fcc Cu, bcc Nb, and bcc $Cu_{0.5}Nb_{0.5}$ solid solution (not stable). All three systems are first heated from their respective solid forms at $T = 0K$ to liquids at 4000K and then cooled back down to $T = 0K$. Each point in the figure represents the average value of enthalpy at each temperature obtained from a 20ps MD run in the NPT ensemble under a Nose-Hoover thermostat. Since our simulation cell is finite in size, the melting temperature is overpredicted upon heating and underestimated upon cooling. This hysteresis is helpful for our calculation, because it allows us to obtain the enthalpy function for both solid and liquid phases beyond the thermodynamic melting temperature. This in turn eases the accurate determination of a temperature where solid and liquid free energies will cross. Within any one given phase (solid or liquid) at one composition, we fit the enthalpy function with a second-order polynomial

$$h(\tau) = A + B\tau + C\tau^2, \tag{5.2}$$

where A, B, C are constants, and use this polynomial in the integral in (5.1).

We use the Hamiltonian switching technique to calculate the free energy $f(T_0)$ at

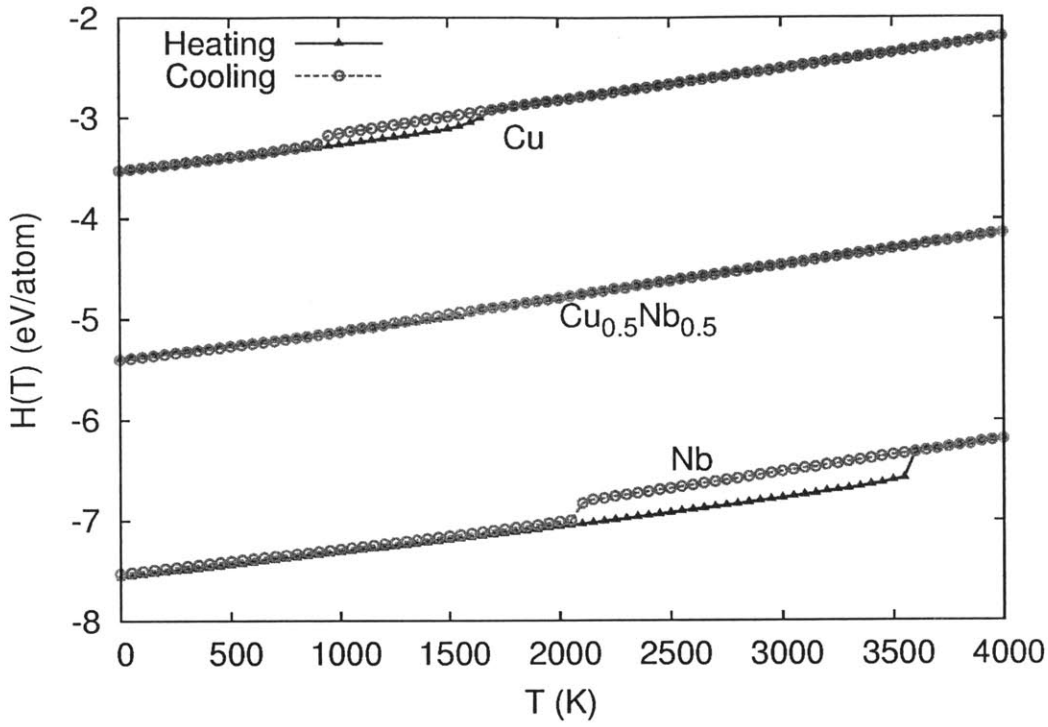

Figure 5-1: Enthalpy as a function of temperature for fcc Cu, bcc Nb, and bcc $Cu_{0.5}Nb_{0.5}$.

the reference temperature, T_0. The free energy of any phase may be expressed as

$$f(T_0) = f_{ref}(T_0) + \Delta f(T_0), \tag{5.3}$$

where $\Delta f(T_0)$ is the free energy difference between the free energy $\Delta f(T_0)$ of the system of interest and that of a different system, whose free energy, $f_{ref}(T_0)$, is assumed to be known. We now define a new Hamiltonian H_S that interpolates between the Hamiltonian of the system with known free energy, U_{ref}, and that of the system of interest, U_{EAM}, as the variable λ goes from 0 to 1 [126]:

$$H_S(\lambda) = \lambda U_{EAM} + (1 - \lambda)U_{ref}. \tag{5.4}$$

The free energy difference may then be written as an integral over the derivative of the Hamiltonian H_S as the variable λ switches it between the reference system and

the system of interest [126]:

$$\Delta f_S = \frac{1}{N}\int_0^1 \langle \frac{\partial H_S}{\partial \lambda} \rangle_\lambda d\lambda = \frac{1}{N}\int_0^1 \langle U_{EAM} - U_{ref} \rangle_\lambda d\lambda \tag{5.5}$$

Here, $\langle \cdots \rangle_\lambda$ represents equilibrium under a Hamiltonian $H_S(\lambda)$ in a canonical (NVT) ensemble for a given value of λ.

A convenient reference system for determining free energies of solids is the Einstein crystal: a collection of harmonic oscillators of frequency ω [161]. The energy of an Einstein crystal is

$$U_{ref} = U_{Eins} = 3Nk_BT, \tag{5.6}$$

and its free energy per particle is

$$f_{Eins}(T_0) = -3k_BT_0 \ln \frac{k_BT_0}{\hbar\omega} = -3k_BT_0 \ln \frac{T_0}{T_E}, \tag{5.7}$$

where T_E is a parameter known as the Einstein temperature. Although in principle the Hamiltonian switching method works for any value of T_E, choosing values that are close to the Debye temperatures of the solids of interest improves numerical accuracy by minimizing the free energy difference between the end states of the integration in (5.5). We therefore choose $T_E = 315K$ for Cu, and $T_E = 275K$ for Nb.

Figure 5-2 shows $\frac{1}{N}\langle U_{EAM} - U_{Eins} \rangle_\lambda$ as a function of λ at $T_0 = 296K$ for bcc Nb. For each λ, the average value of $U_{EAM} - U_{Eins}$ is obtained from a 20ps MD run at constant volume and constant temperature. Then we use a sixth-order polynomial to fit $\frac{1}{N}\langle U_{EAM} - U_{Eins} \rangle_\lambda$ as a function of λ and obtain Δf_S by integrating over λ from 0 to 1.

The procedure to calculate the liquid phase free energy is similar to that for the solid phase, but the reference state is the ideal gas [162]. Since in an ideal gas there is no interaction among atoms and atoms may overlap, an intermediate repulsive gas state is necessary to bridge the reversible path for switching from the liquid to the

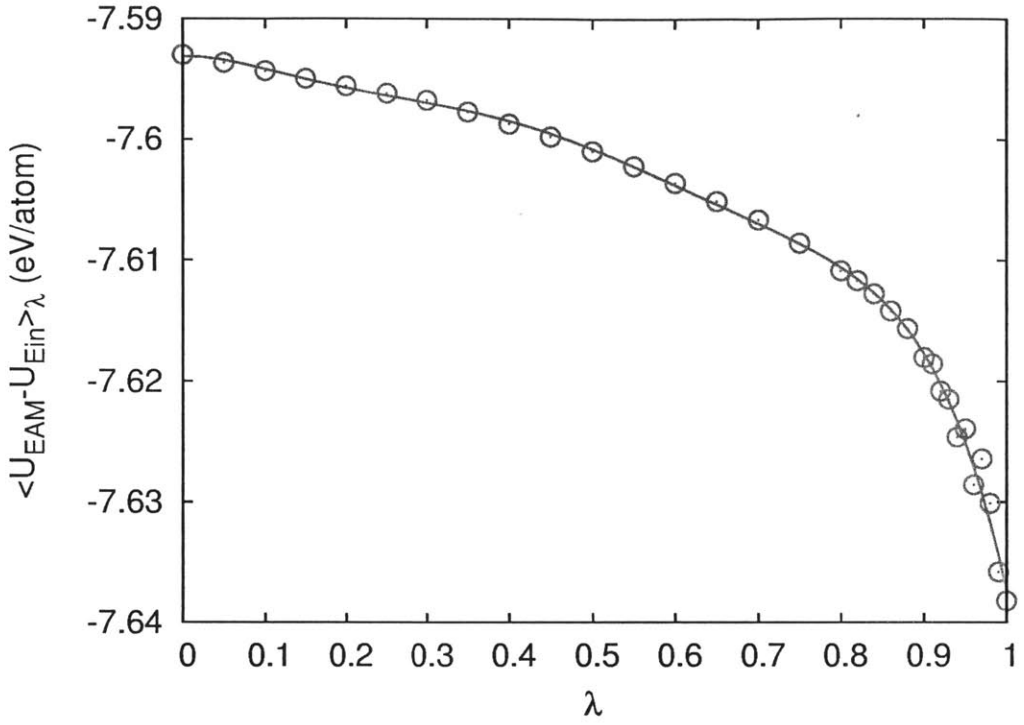

Figure 5-2: $\langle U_{EAM} - U_{Eins} \rangle_\lambda$ as a function of λ for bcc Nb at T=296K.

ideal gas. Thus, we write the liquid phase free energy as

$$f_{EAM,L}(T_0) = f_{ideal}(T_0) + \Delta f_{L1} + \Delta f_{L2}, \tag{5.8}$$

where $f_{ideal}(T_0)$ is the free energy of an ideal gas at T_0, Δf_{L1} is the free energy difference between the liquid phase and a repulsive gas, and $\Delta_f L2$ is the free energy difference between the repulsive and ideal gasses.

Any purely repulsive interatomic potential may be used to model the repulsive gas. We use the purely repulsive part of the pair interaction terms in our EAM so that the repulsive gas state is close to the liquid state predicted by the potential, increasing the numerical accuracy of the integral in (5.5). For the liquid phase we therefore write

$$H_S(\lambda) = \lambda U_{EAM} + (1 - \lambda) U_{replusive}. \tag{5.9}$$

This expression can be used to determine the free energy difference between the EAM

liquid, governed by Hamiltonian U_{EAM}, and the repulsive gas, governed by $U_{repulsive}$, using (5.5):

$$\Delta f_{L1} = \frac{1}{N}\int_0^1 \langle U_{EAM} - U_{repulsive}\rangle_\lambda d\lambda \tag{5.10}$$

Then, the repulsive gas can be expanded to an ideal gas with infinite volume at zero pressure. The work done for this reversible process is

$$\Delta f_{g1} = \int P dv = k_B T_0 \int_0^{\rho_0} \frac{P}{\rho k_B T_0}\frac{d\rho}{\rho}. \tag{5.11}$$

The free energy of an ideal gas made up of atoms of mass m at density ρ_0 and temperature T_0 has the analytic form [161]

$$f_{ideal}(T_0, \rho_0) = k_B T_0 \left[\ln\left(\rho\Lambda^3\right) - 1\right], \tag{5.12}$$

where Λ is the de Broglie thermal wavelength given by

$$\Lambda = \frac{h}{\sqrt{2\pi m k_B T_0}}. \tag{5.13}$$

The free energy of an ideal gas with zero density can be determined by compressing it to an ideal gas with density ρ_0. The work required for this reversible process, which is the free energy difference between the two states, has the simple form

$$\Delta f_{g2} = \int P dv = k_B T_0 \int_{\rho_0}^{0} \frac{d\rho}{\rho}. \tag{5.14}$$

The, the free energy difference between the repulsive gas and the ideal gas of equal density ρ_0 is

$$\Delta f_{L2} = \Delta f_{g1} + \Delta f_{g2} = k_B T_0 \int_0^{\rho_0} \left(\frac{P}{\rho k_B T_0} - 1\right)\frac{d\rho}{\rho}. \tag{5.15}$$

The free energies for Einstein crystals and ideal gasses given above hold for single-component systems. For an alloy with composition x, the free energy of its Einstein crystal should additionally include the configuration entropy contribution $S_{conf}(x)$,

which can be expressed as

$$f_{Eins}(x, T_0) = (1-x) f_{Eins}^{Cu} + x f_{Eins}^{Nb} - T_0 s_{conf}(x), \tag{5.16}$$

where $s_{conf}(x) = -k_B [x \ln(x) + (1-x)\ln(1-x)]$ for an ideal solid solution. Similarly, for an ideal gas the free energy can be calculated as the sum of two separate gases with no configurational entropy, or two mixed gases with configurational entropy contribution

$$\begin{aligned} f_{ideal}(x, T_0, \rho_0) &= (1-x) f_{ideal}^{Cu}(T_0, (1-x)\rho_0) + x f_{ideal}^{Nb}(T_0, x\rho_0) \\ &= (1-x) f_{ideal}^{Cu}(T_0, \rho_0) + x f_{ideal}^{Nb} - T_0 s_{conf}(x). \end{aligned} \tag{5.17}$$

We use the Hamiltonian switching methods discussed above to determine free energy values at reference temperatures T_0 for both solid and liquid phases. For solids we choose $T_0 = 296K$ and for liquids $T_0 = 4000K$. Then, using the Gibbs-Duhem integral, free energies for both phases at any temperature can be obtained by integrating over the enthalpies. We then express these free energies as functions of composition and temperature, using the form

$$f_{EAM}^{bcc,fcc,liq}(x, T) = A(x) - B(x)T\ln(T) - C(x)T^2 + D(x)T, \tag{5.18}$$

where $A(x)$, $B(x)$, $C(x)$ (from Gibbs-Duhem integration) and D(x) (from Hamiltonian switching calculations) are functions of concentration. Then common tangent lines are constructed to obtain the phase boundaries at different temperatures.

5.2 Liquid phase miscibility gap

Since the method for obtaining free energies described above relies on integrals of enthalpy, it may only be used for phases that are stable over the duration of the MD run needed to compute the average enthalpy. In particular, the above scheme will not work for a uniform liquid inside a miscibility gap because such a single liquid phase

is not stable: atoms in the liquid are often sufficiently mobile to establish two-phase coexistence rapidly (within a few tens to hundreds of ps) if it is thermodynamically favorable. Semi-grand-canonical Monte-Carlo (SGC-MC) calculations (introduced in Chapter 3) have proven useful for studying miscibility gaps in both solid phases, e.g. Si-Ge [163, 164], and liquid phases, such as Cu-Pb [84] and Lennard-Jones models [165]. Thus, we use SGC-MC coupled with MD to identify liquid miscibility gaps [130].

In our calculations, the chemical potential difference $\Delta\mu = \mu_{Cu} - \mu_{Nb}$, the total number of atoms N, and system temperature T are held fixed under constant zero pressure, P. A system with 32000 atoms is equilibrated by iteratively making 5×10^3 attempts at switching the chemical identities of Cu-Nb atom pairs with probabilities governed by Metropolis sampling followed by MD for 0.4 ps, which is long enough to relax local distortions from the transmutation of atoms. By varying the chemical potential difference while keeping other parameters constant we obtain the equilibrium concentration as a function of $\Delta\mu$. If a miscibility gap exists, this curve has a hysteresis loop in a finite system. The hysteresis is due to the free energy barrier to nucleate the second phase when approaching the miscibility gap from a single-phase region. If there is no miscibility gap, the equilibrium composition does not depend on the history of system and shows no hysteresis when $\Delta\mu$ is varied. Examples of calculations with and without hysteresis are shown in Figure 5-3.

5.3 Comparison of phase diagrams of three EAM potentials

The computed complete binary phase diagrams for these three potentials are shown in Figure 5-4. The three potentials all show limited solubility in fcc Cu and bcc Nb phases, but with completely different liquid phase thermodynamics. The phase diagram of our newly constructed potential EAM1 is in semi-quantitative agreement with the experimental phase diagram. They both have a fully miscible liquid phase as

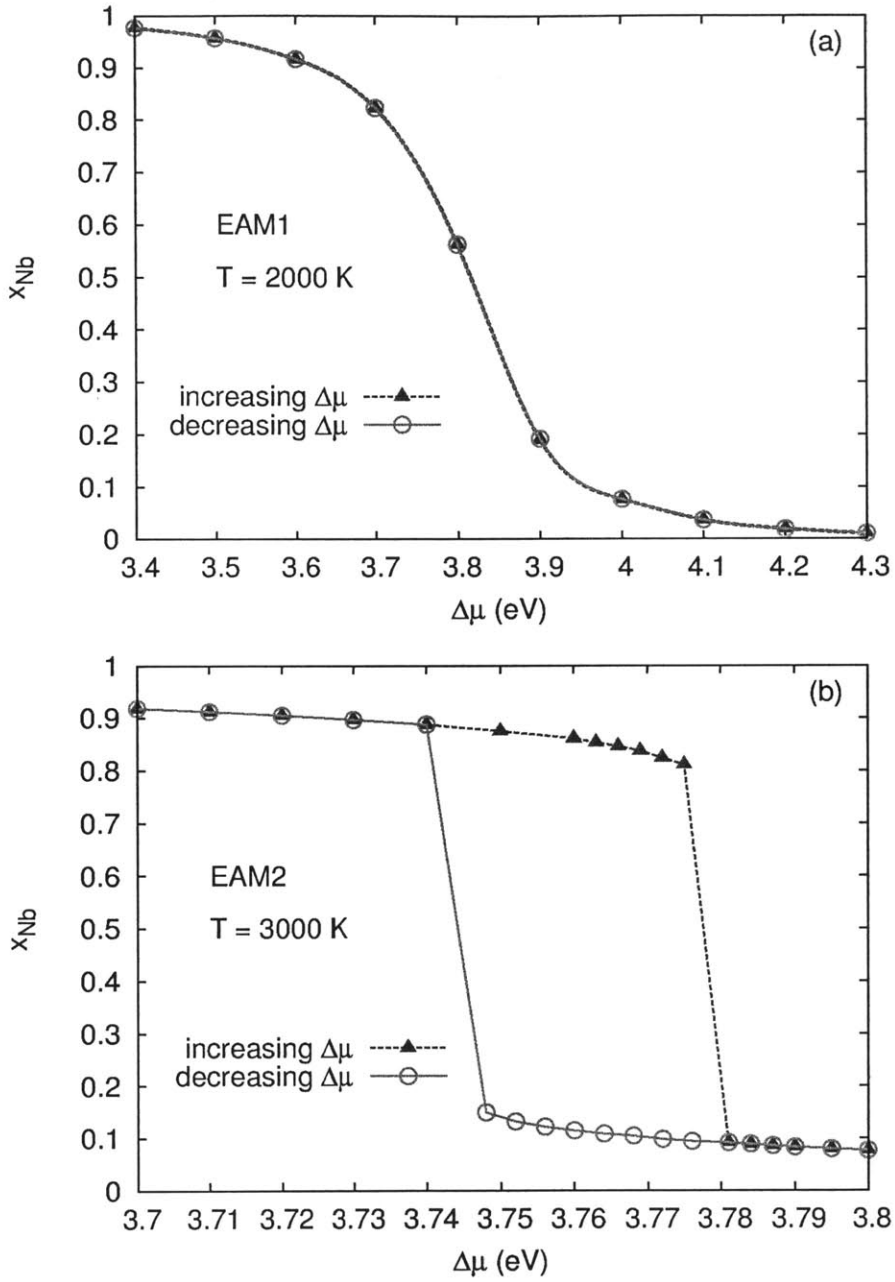

Figure 5-3: Equilibrium Nb concentration in the liquid phase as a function of chemical potential difference obtained from SGC-MC calculations. In (a), the liquid phase is completely miscible under EAM1 at $T = 3000K$, so there is no hysteresis in the Nb concentration. The hysteresis in (b) indicates a liquid miscibility gap for EAM2 at $T = 3000K$.

well as a eutectic point, although the eutectic point in the phase diagram of EAM lies at 20 at% Nb and 830°C, while the eutectic in the experimental phase diagram locates near the melting point of Cu with very limited Nb solubility. Correspondently, the Nb liquidus line in the phase diagram of EAM1 ends up at higher Nb concentration than the liquidus line in the experimental phase diagram. Nevertheless, the phase diagram predicted by EAM1 has the basic features and topologically agrees with experiments. Therefore, the cross potential we obtained by fitting enthalpies of mixing as a function of composition at $T = 0K$ reproduces the thermodynamics of both liquid and solid phases reasonably well. The melting temperature of Nb is overpredicted compared with experiments, but this is a result of the single-element Nb potential and not due to the fitting of the cross-element interactions.

EAM2 also predicts a eutectic point, which is located at 3.5 at% Nb and 1055°C. Unlike the experimental phase digram, the phase diagram for EAM2 has a wide range liquid miscibility gap with critical temperature near 3500°C, possibly close to or even above the thermodynamic boiling point (not determined in this study). By contrast, EAM3 predicts a completely miscible liquid phase. The eutectic point could not be determined because the Cu-Nb liquid vitrifies before the eutectic temperature is reached. The atomic mobility in the glassy state is negligible, thus the liquid free energy cannot be extrapolated to these temperatures. The thermodynamically favorable state for EAM3 at low temperatures in the mid-range of compositions may be a complex compound or even a non-crystalline solid.

5.4 Comparison of liquid phase thermodynamics of three EAM potentials

The composition-dependent free energies of mixing of liquid phases at $T = 4000K$ and $T = 2500K$ for the three potentials are shown in Figure 5-5(a). EAM2 predicts liquid phase separation at $T = 2500K$, so the free energy of a single-phase liquid under EAM2 is not accessible through molecular dynamics at this temperature and

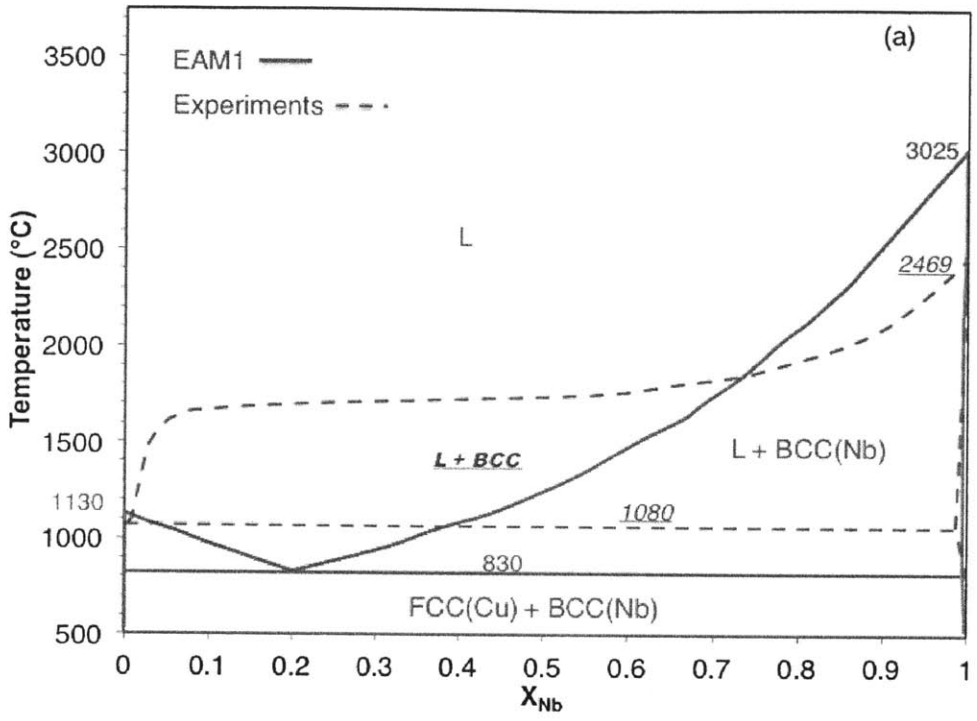
(a)
EAM1
Experiments
3025
L
2469
L + BCC
L + BCC(Nb)
1130
1080
830
FCC(Cu) + BCC(Nb)
Temperature (°C)
3500
3000
2500
2000
1500
1000
500
0
0.1
0.2
0.3
0.4
0.5
0.6
0.7
0.8
0.9
1
X_{Nb}

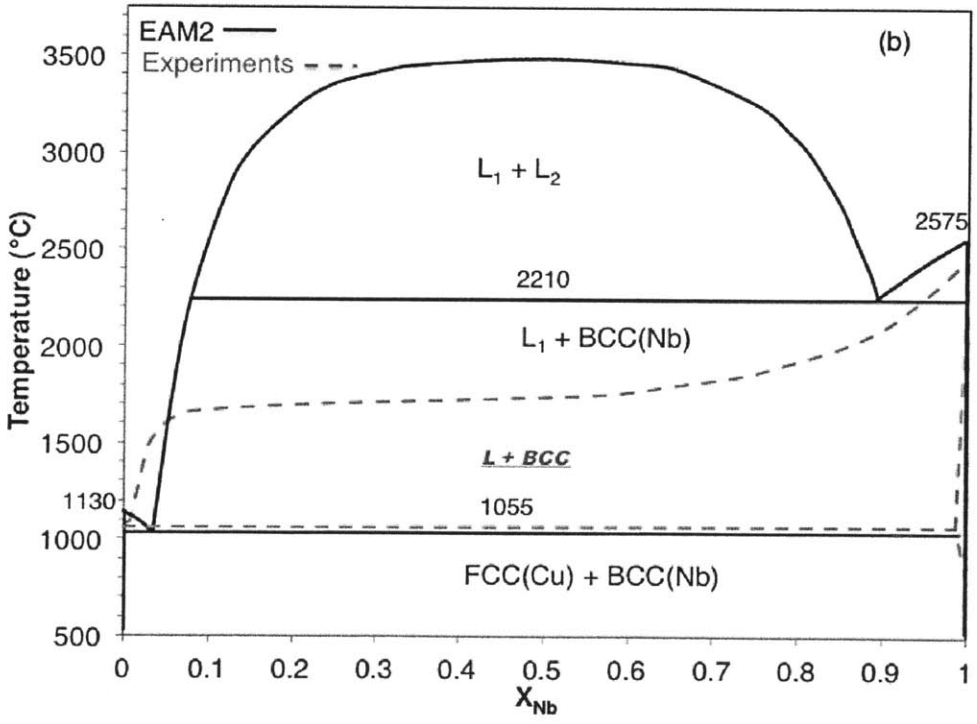
(b)
EAM2
Experiments
$L_1 + L_2$
2575
2210
L_1 + BCC(Nb)
L + BCC
1130
1055
FCC(Cu) + BCC(Nb)
Temperature (°C)
3500
3000
2500
2000
1500
1000
500
0
0.1
0.2
0.3
0.4
0.5
0.6
0.7
0.8
0.9
1
X_{Nb}

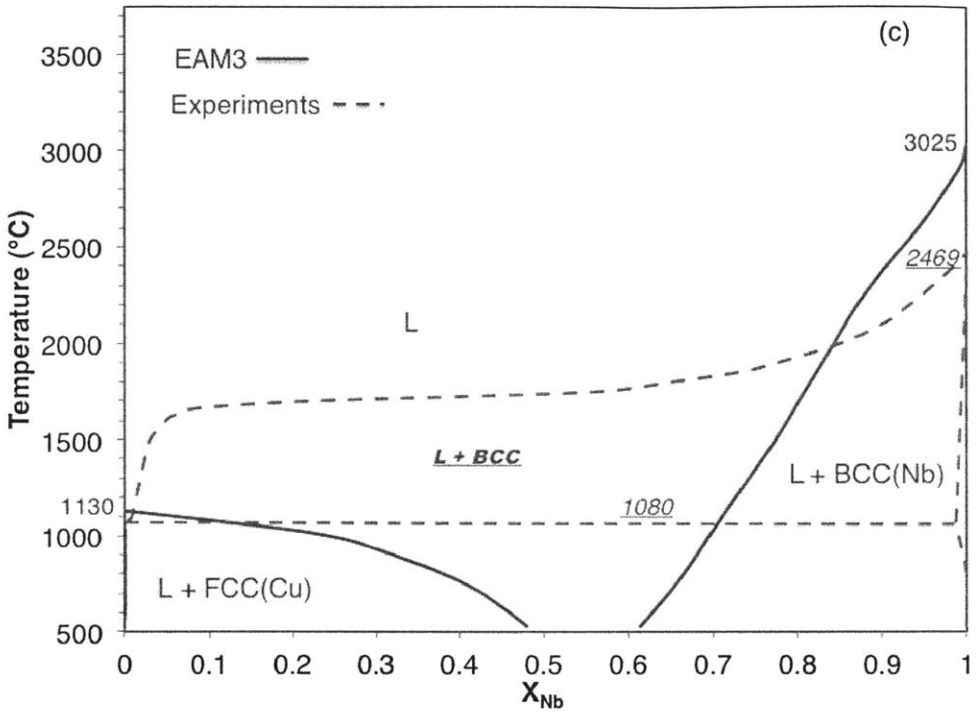

Figure 5-4: Equilibrium binary phase diagram computed using (a) EAM1, (b) EAM2, and (c) EAM3, compared with experimental phase diagram. The Phase diagram from EAM1 shown in (a) is closest to the experimentally determined Cu-Nb phase diagram among all three potentials tested in this study.

is therefore not plotted. As expected, EAM2, which has a liquid miscibility gap, has the highest free energy of mixing in the liquid phase, while EAM3 has the lowest free energy of mixing.

Enthalpies of mixing corresponding to the curves in Figure 5-5(a) are plotted in Figure 5-5(b). To estimate the enthalpy of mixing for the undercooled single-phase liquid in EAM2 at $T = 2500K$, we equilibrate a structure at 50% Nb concentration taken from EAM3 at 2500K under EAM2 for 2 ps, which is too short for substantial phase separation to occur. Although both EAM1 and EAM2 have positive enthalpies of mixing, the former is considerably lower than that of EAM2. The enthalpy of mixing in EAM3 has an anomalous shape: positive in the Cu-rich liquid and negative in the Nb-rich liquid. The negative part may account for the deep eutectic observed in this potential.

Given free energies and enthalpies of mixing, entropies of mixing may be also obtained. They are shown in Figure 5-5(c) for the three potentials at $T = 2500K$ and $T = 4000K$. EAM3 has the largest entropy of mixing, while those of EAM1 and EAM2 are similar in magnitude. The full liquid miscibility in EAM1 is therefore due to its relatively lower enthalpy of mixing than in EAM2, not higher entropy.

Figure 5-5(d) shows the excess volume as a function of composition for equilibrium liquid phases at $T = 4000K$ (above the critical temperature in EAM2) and at $T = 2500K$ (inside the liquid miscibility gap). The excess volume ΔV is defined as

$$\Delta V = V_{liq} - (xV_{Cu} + (1-x)V_{Nb}), \tag{5.19}$$

where V_{liq}, V_{Cu} and V_{Nb} are the volumes of liquid alloy, pure Cu, and pure Nb, respectively. Again, we estimate the excess volume of undercooled single-phase liquid for EAM2 at 2500K by equilibrating the structure from EAM3 and plotted in Figure 5-5(d). For both high and low temperatures, the liquid phase in EAM1 has almost zero excess volume, EAM2 has large positive excess volumes, and EAM3 predicts a more packed Cu-Nb liquid alloy with negative excess volume. Comparing Figure 5-5(d) to Figure 5-5(c), we see that the trend in excess volumes is opposite to that of entropy for three different potentials, i.e., liquid phase with larger excess volume has lower entropy.

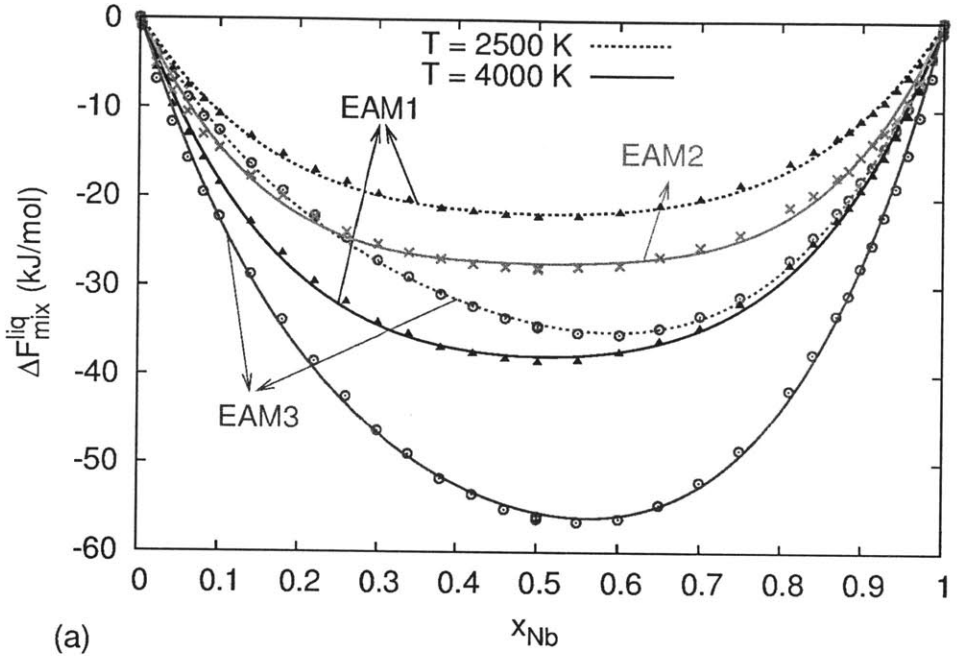
T = 2500 K
T = 4000 K
EAM1
EAM2
EAM3
ΔF^{liq}_{mix} (kJ/mol)
x_{Nb}

(a)

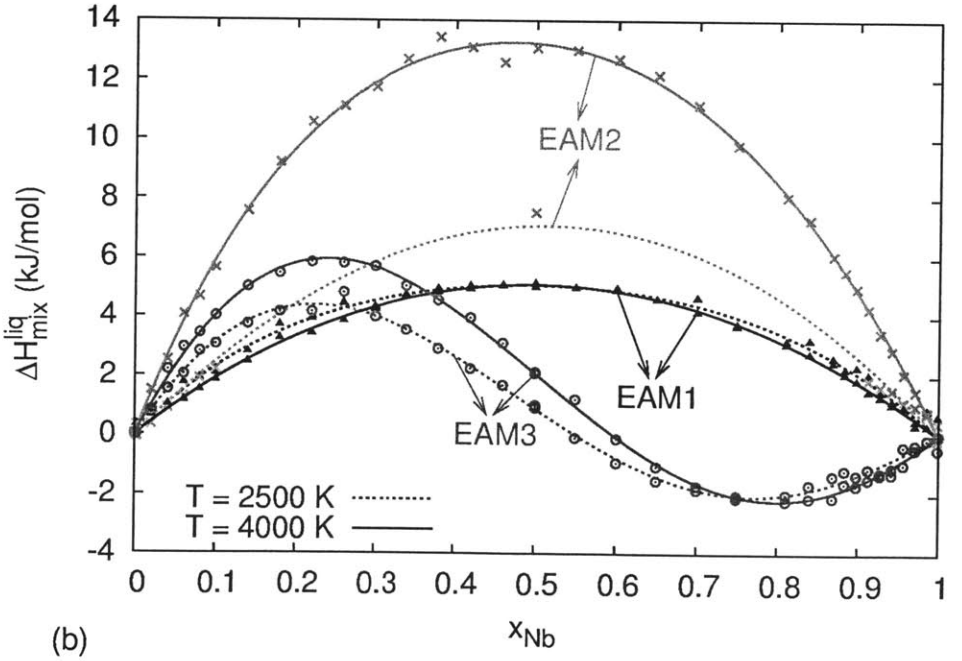
EAM2
EAM1
EAM3
T = 2500 K
T = 4000 K
ΔH^{liq}_{mix} (kJ/mol)
x_{Nb}

(b)

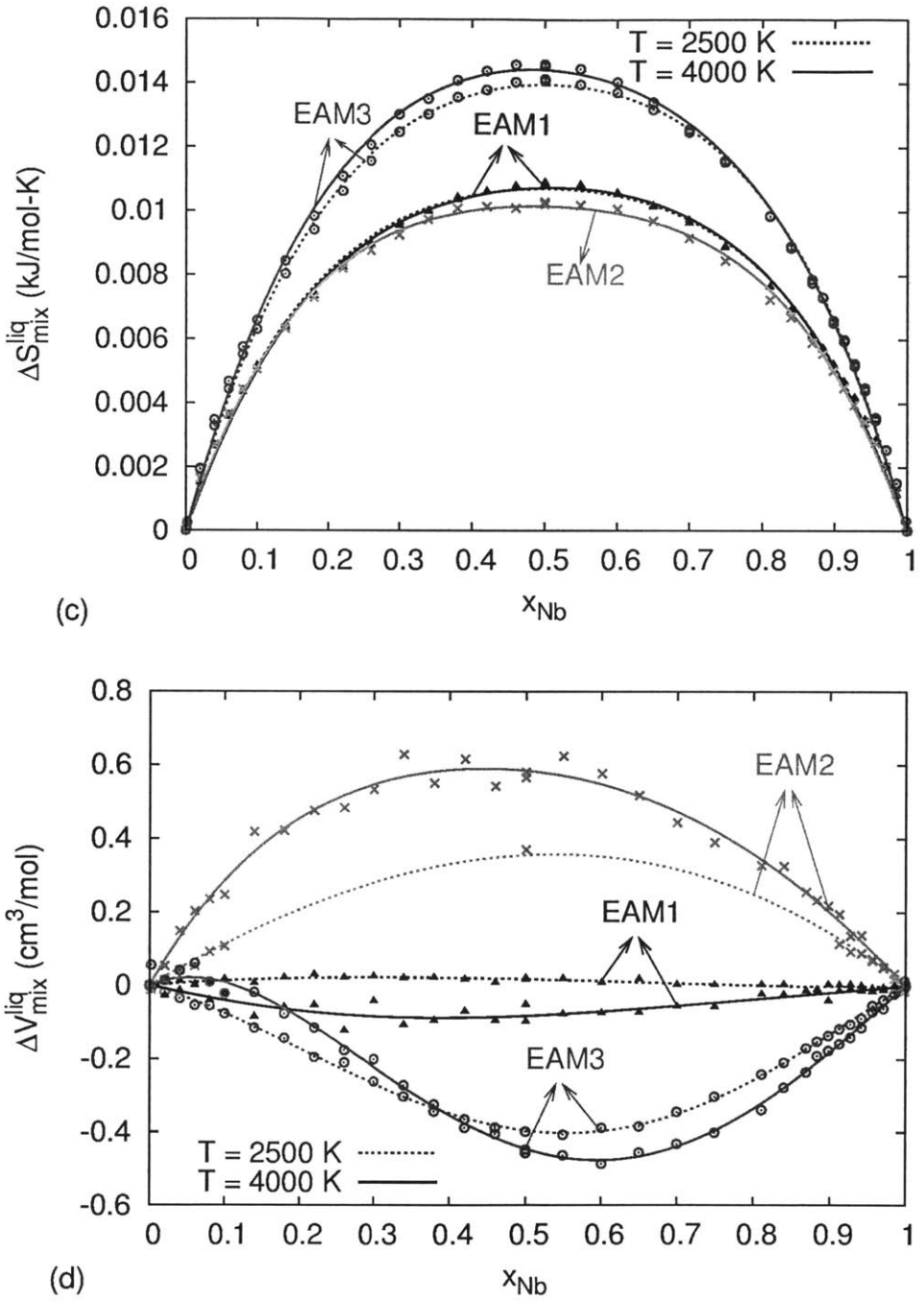

Figure 5-5: Free energy of mixing (a), enthalpy of mixing (b), entropy of mixing (c), and excess volume (d) as a function of composition for equilibrium liquid phases under EAM1, EAM2, and EAM3 at 4000 K and 2500 K. The free energy and entropy of mixing under EAM2 at 2500K in (a) and (c) is not shown because of liquid phase separation.

The thermodynamic behavior predicted by the potentials is readily verified by MD. We performed long-time simulations in the NPT ensemble starting from phase separated pure Cu and Nb liquids at 2500K, as shown in Figure 5-6(a). During this simulation, the undercooled Nb remains liquid: it does not crystallize nor vitrify. The diffusivity of Nb atoms in the undercooled liquid at 2500K is $4.6 \times 10^{-4}\text{cm}^2/\text{s}$ for EAM1 and EAM3 and $3.2 \times 10^{-4}\text{cm}^2/\text{s}$ for EAM2. Both are high values characteristic of liquids. The initially phase separated liquids evolve differently under the three different potentials. As expected, after 3ns under EAM2, the liquid remains phase separated, with only individual impurity atoms mixing into the single-phase liquid. For systems governed by EAM1 and EAM3, a single liquid phase is thermodynamically favorable and the two starting liquid phases become completely mixed.

5.5 Comparison of liquid phase structures of three EAM potentials

The final liquid structure under EAM1, Figure 5-6(b), appears to be less randomly mixed than the liquid structure from EAM3, Figure 5-6(d). In fact, EAM1 appears to yield a compositionally patterned liquid structure with a characteristic length scale at equilibrium. To further confirm that the compositionally patterned liquid represents the liquid in thermodynamic equilibrium, we conduct another MD simulation starting from the more perfectly mixed liquid structure obtained using EAM3 shown in Figure 5-6(d). Allowing this structure to equilibrate under EAM1, we find that it reverts back to a compositionally patterned structure like that in Figure 5-6(b) within only a few ps. No matter what the initial configuration, the final equilibrium liquid in EAM1 always shows local compositional patterning.

To further characterize the structure of the liquids modeled above, we computed the average short-range order (SRO) parameter. For any Cu atom, the SRO is [166]

$$SRO_{Cu} = 1 - \frac{Z_{Nb}}{Z_{tot} x_{Nb}}. \tag{5.20}$$

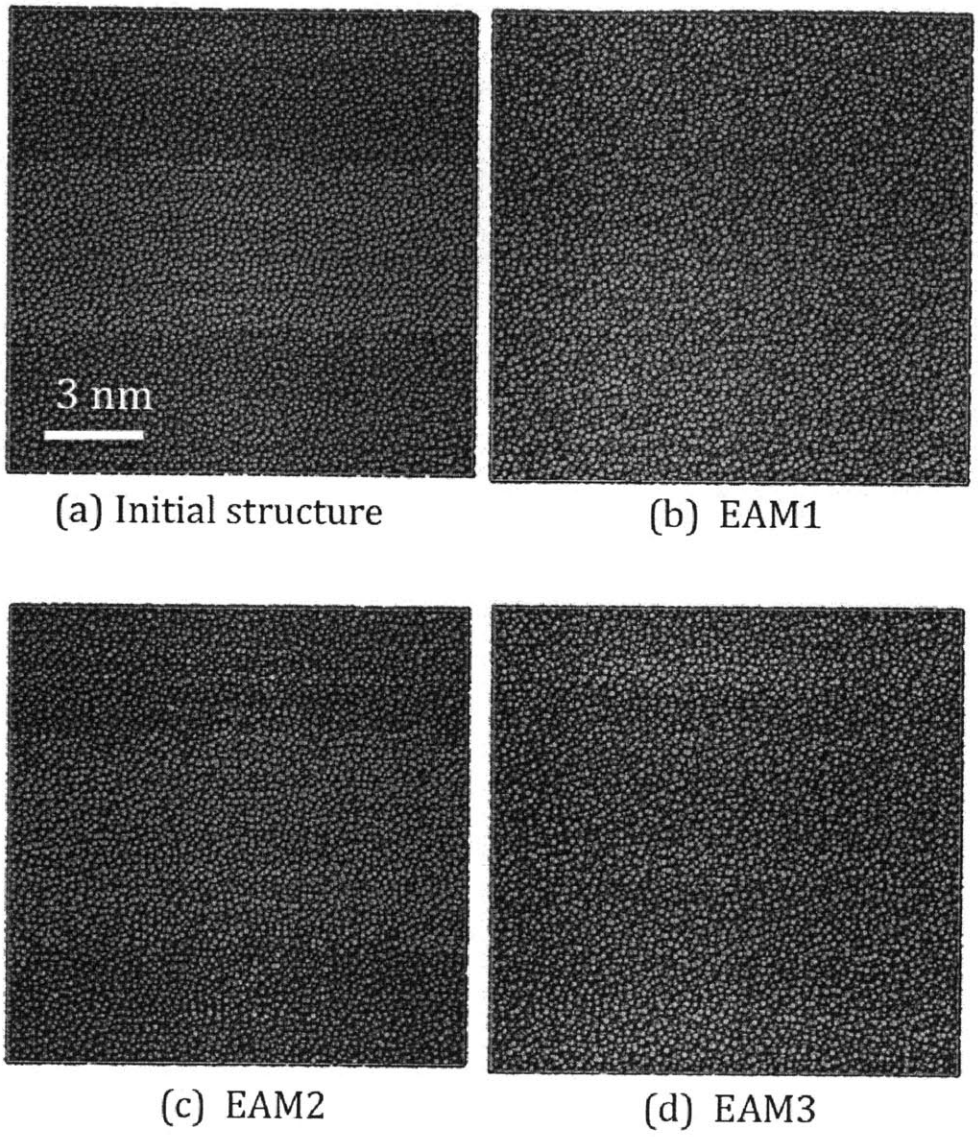

Figure 5-6: Cu-Nb liquids equilibrating in NPT MD simulations at 2500K. The initial configuration is shown in (a). After 3ns, the Cu-Nb liquid (b) becomes a compositionally patterned single phase under EAM1, (c) remains phase separated under EAM2, and (d) becomes a uniformly mixed single phase under EAM3. The supercells are cubes with edge lengths of 12nm containing 54000 Cu (yellow) and 54000 Nb (blue) atoms.

Here, Z_{Nb} is the number of Nb atoms within a specified cutoff distance of the central Cu atom, Z_{tot} is the total number of atoms within the cutoff, and x_{Nb} is the average concentration of Nb atoms in the system. Similarly, we define SRO for Nb atoms as

$1 - Z_{Cu}/\left(Z_{tot}x_{Cu}\right)$. The cutoff distance is determined to be the first minimum in the pair distribution function of the liquid phase, which is about 4Å for both Cu and Nb atoms in our study.

From the above definition, for a binary system with concentration 50%, the SRO equals 1 when the Cu and Nb atoms are completely phase separated, 0 when Cu and Nb atoms are randomly mixed, and negative or equal to -1 when Cu-Nb forms an ordered structure. As shown in Figure 5-7, the average SRO for Cu and Nb atoms in liquid phase with 50% Nb under EAM2 increases with time at 2500K due to phase separation. EAM3 shows nearly ideal random mixing, with SRO equals to 0. The liquid phase in EAM1, however, has a SRO parameter at equilibrium of about 0.08, implying that the liquid has some local ordering.

To further investigate this ordering, we compute the Bhatia-Thornton structure factors, which can be expressed as [167],

$$\begin{aligned} S_{nn}(q) &= x_A^2 S_{AA}(q) + x_B^2 S_{BB}(q) + 2x_A x_B S_{AB}(q), \\ S_{cc}(q) &= x_A x_B \left[1 + x_A x_B \left(S_{AA}(q) + S_{BB}(q) - 2S_{AB}(q)\right)\right], \end{aligned} \tag{5.21}$$

where $S_{\alpha\beta}(\alpha\beta = AA, AB, BB)$ is the pair static structure factor, which is a Fourier transform of pair distribution function $g_{\alpha\beta}$ for a system with volume V and number of atoms N [126],

$$S_{\alpha\beta}(q) = 1 + \frac{N}{V}\int_0^\infty \left[g_{\alpha\beta}(q) - 1\right]\frac{\sin qr}{qr} 4\pi r^2 dr. \tag{5.22}$$

The Bhatia-Thornton structure factors $S_{nn}(q)$ and $S_{cc}(q)$ can be viewed as static spatial correlation functions for number-number and concentration-concentration fluctuations, and their values for equilibrium liquid structures from EAM1 and EAM3 are shown in Figure 5-8.

The number-number structure factors $S_{nn}(q)$ are very similar in EAM1 and EAM3. The locations of their first peaks are both at $q = 2.72\text{Å}^{-1}$, indicating the average distance of the first nearest neighbors in EAM1 and EAM3 are very similar. The small values of $S_{nn}(0)$ in EAM1 and EAM3 represent a typical dense liquid with very

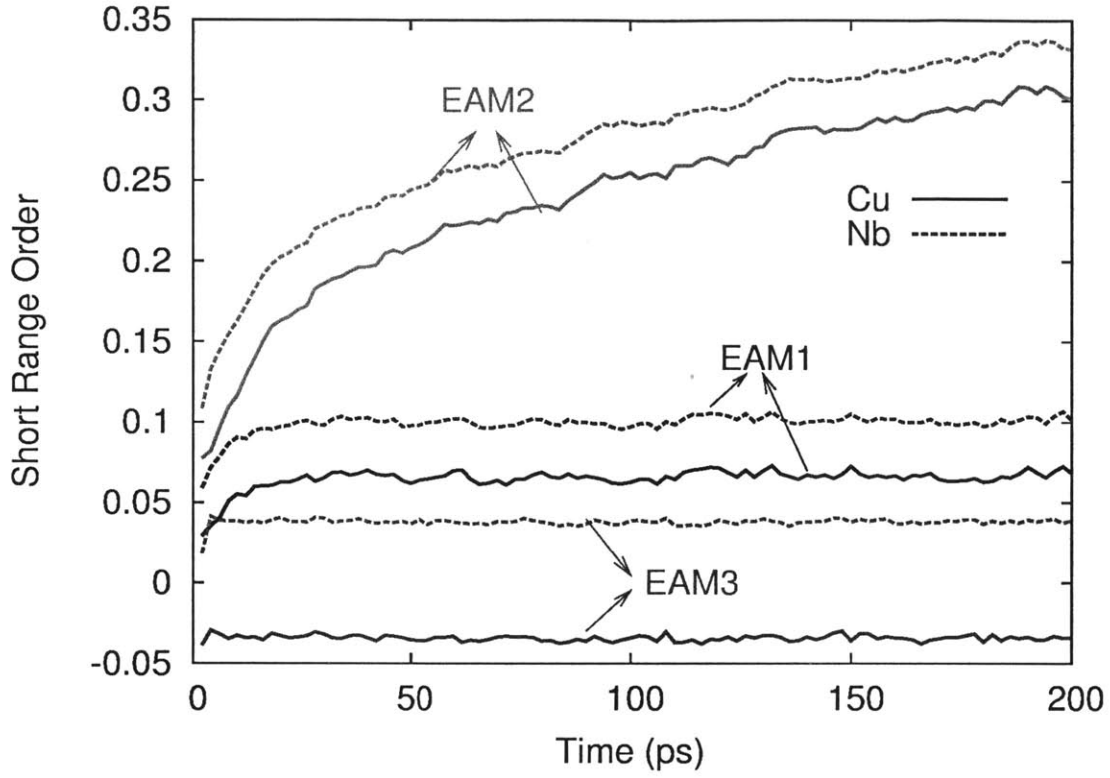

Figure 5-7: Cu-Nb liquids equilibrating in NPT MD simulations at 2500K. The initial configuration is shown in (a). After 3ns, the Cu-Nb liquid (b) becomes a compositionally patterned single phase under EAM1, (c) remains phase separated under EAM2, and (d) becomes a uniformly mixed single phase under EAM3. The supercells are cubes with edge lengths of 12nm containing 54000 Cu (red) and 54000 Nb (blue) atoms.

low compressibility. However, the concentration-concentration structure factors S_{cc} in EAM1 and EAM3 are quite different. The first peak in S_{cc} for EAM3 occurs at a different wavenumber from the first peak in S_{nn} and S_{cc} has a minimum close to the wavenumber of the first peak in S_{nn}. These peak positions are consistent with the complete liquid miscibility of EAM3, because on the nearest neighbor length scale, Cu atoms are preferentially surrounded by Nb atoms and vice versa, so that the local concentration of Cu (or Nb) is smaller than the average concentration, which gives rise to the minimum in S_{cc} close to the first peak in of S_{nn}.

For EAM3, the first peaks in both S_{cc} and S_{nn} occur near $q \approx 2.72\text{Å}^{-1}$, but are nevertheless slightly offset due to liquid phase miscibility. Unlike EAM3, however, S_{cc}

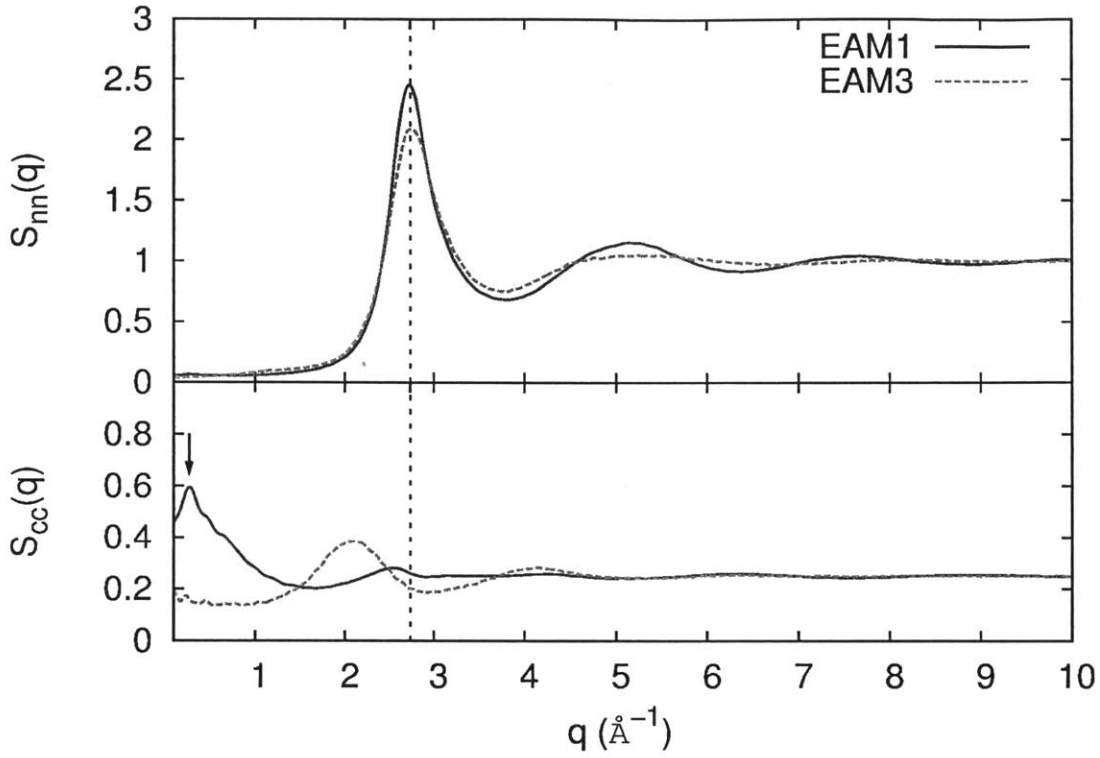

Figure 5-8: Structure factors S_{nn} and S_{cc} in equilibrium liquids at 2500K from EAM1 and EAM3. The arrow indicates a small peak at $q \approx 0.27\text{Å}^{-1}$ for S_{cc} under EAM1, corresponding to a characteristic length $\lambda \approx 23\text{Å}$.

for EAM1 has an additional peak at $q \approx 0.27\text{Å}^{-1}$. To confirm this peak is statistically significant, we calculated the uncertainty of S_{cc}, shown for low q values in Figure 5-9. To obtain these uncertainties, the error bars on partial pair distribution functions are first calculated based on variations of $g(r)$ for each atom. Then, the standard deviation of the mean of S_{cc} is obtained via their Fourier Transforms. Figure 5-9 demonstrates that the decrease in S_{cc} below $q \approx 0.27\text{Å}^{-1}$ is statistically significant. In addition, we computed $S_{cc}(q)$ for system sizes ranging from 50,000 to 300,000 atoms, and found that the location of the peak does not depend on system size. In view of the above evidence, we believe that the peak in S_{cc} at $q \approx 0.27\text{Å}^{-1}$ is not an artifact of the way we compute S_{cc}. Rather, it is due to compositional patterning over a length much larger than the nearest neighbor distance. The characteristic length λ corresponding to a given q is $\lambda = 2\pi/q$ giving $\lambda \approx 23\text{Å}$ for $q \approx 0.27\text{Å}^{-1}$, in good

qualitative agreement with the length scale for compositional patterning deduced by visual inspection of Figure 5-6(b).

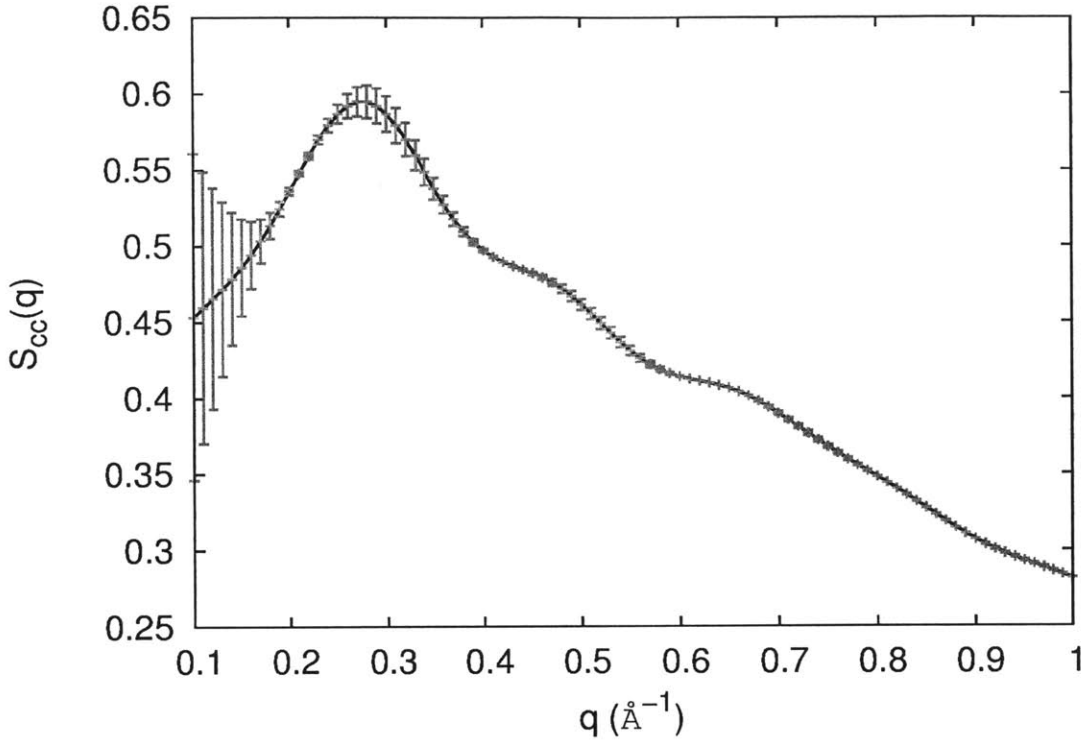

Figure 5-9: Concentration-concentration structure factor S_{cc} for EAM1 in the small q region with uncertainties plotted.

5.6 Comparison of liquid phase interdiffusivities of three EAM potentials

By carrying out multiple collision cascade simulations using the three EAM potentials in the next Chapter, we will show that radiation-induced mixing is highly dependent on liquid phase properties. In addition, most mixing occurs inside TSs, which may be viewed as hot transient liquid droplets. Therefore, we investigate whether liquid phase interdiffusion may account for the mixing observed in TSs. To that end, we calculate liquid phase interdiffusivities for all three potentials at 4000K, corresponding

to typical initial temperatures inside TSs.

We use two methods to determine liquid phase interdiffusivities. In the first, we perform direct MD simulations of intermixing between pure Cu and pure Nb, which were equilibrated separately at 4000K. We then join the two liquids, allow them to intermix during an extended MD run using the NPT ensemble [168], and measure the interdiffusivity from the concentration profile, which will be described in Section 6.3.3. The outcomes are given in Table 5.1 and show that interdiffusion is fastest in EAM3, slowest in EAM2, and intermediate in EAM1.

We also calculate liquid phase interdiffusivity in each potential directly from the free energy of the liquid phase. Assuming the atomic volume of Cu and Nb in the liquid phase at 4000K is similar, the concentration dependent interdiffusivity may be related to intrinsic diffusivities by

$$\tilde{D} = x_1 D_2 + x_2 D_1, \tag{5.23}$$

where $x_{1(2)}$ is atom fraction, and intrinsic diffusivity $D_{1(2)}$ may be written as

$$D_{1(2)} = \frac{x_{1(2)}}{k_B T} \frac{d\mu_{1(2),T}}{dx_{1(2)}} D^*_{1(2)} = \frac{x_{1(2)}(1 - x_{1(2)})}{k_B T} \frac{d^2 f_T}{dx^2_{1(2)}} D^*_{1(2)}, \tag{5.24}$$

where $D^*_{1(2)}$ is the self-diffusivity of Cu(Nb) in a chemically homogenous binary solution [133]. D^*_1 and D^*_2 were determined by computing mean squared displacements of Cu and Nb atoms in separate simulations on compositionally uniform liquids. In (5.24), we used the relation between chemical potential, $\mu_{1(2),T}$, and Gibbs free energy, f_T,

$$\mu_{1(2),T} = f_T(x_{1(2)}) + \frac{df_T(x_{1(2)})}{dx_{1(2)}}(1 - x_{1(2)}). \tag{5.25}$$

We obtained the Gibbs free energy of the liquid state for all three potentials via the Hamiltonian switching method, as described in Section 5.1. At a given temperature T, it may also be expressed as

$$f_T(x) = s_0 + s_1 x + s_2 x^2 + s_3 k_B T \left(x \ln x + (1 - x) \ln(1 - x)\right), \tag{5.26}$$

Table 5.1: Liquid phase interdiffusivities (Å^2/ps) at 4000K calculated by two methods for all three EAM potentials as well as parameters used in the calculation of interdiffusivity using the free energy method.

Potential	Liquid phase interdiffusivity		Parameters			
	From MD	From free energy	s_2 (eV)	s_3	D_1^* (Å^2/ps)	D_2^* (Å^2/ps)
EAM1	1.40	1.30	-0.285	0.99	2.14	1.50
EAM2	0.79	0.74	-0.625	1.01	2.04	1.52
EAM3	2.55	3.06	0.402	1.00	2.55	1.86

where $s_{0,1,2,3}$ are fitting parameters. For solutions showing no short range order, s_3 is unity. Combining (5.23) with the preceding three expressions, the concentration dependent interdiffusivity may be written as

$$\tilde{D} = x_1 D_2 + x_2 D_1 = \left(\frac{2s_2}{k_B T} x_1 x_2 + s_3 \right) (x_1 D_2^* + x_2 D_1^*) . \tag{5.27}$$

Note that parameters s_0 and s_1 do not affect interdiffusivity because they simply interpolate between the free energies of the pure elements and therefore do not influence the excess free energy. Then, the average liquid phase interdiffusivity is

$$\bar{D} = \int_0^1 \tilde{D} dx_1 = \left(\frac{s_2}{6k_B T} + \frac{s_3}{2} \right) (D_1^* + D_2^*) . \tag{5.28}$$

The interdiffusivities calculated by this method are listed in Table 5.1. They are found to be in good agreement with those computed from direct MD simulations of interdiffusion of pure Cu and Nb liquids. The parameters used in (5.28) are listed in Table 5.1. The self-diffusivities, D_1^* and D_2^*, as well as parameter s_3 have nearly equal values in all three potentials. Only the values of s_2 differ substantially.

Chapter 6

Radiation-induced Mixing at Isolated Interfaces

This Chapter is designed specifically to investigate the effect of liquid phase properties on radiation-induced mixing (RIM) using MD simulations. It is carried out by simulating ~10,000 10keV PKAs per model investigated, corresponding to high dose, heavy ion or neutron bombardment. We focus on the low temperature limit of RIM, where no thermally activated diffusion occurs. In immiscible metals, these conditions give an upper bound on RIM rates, since the effect of thermally assisted diffusion would have been to cause thermodynamically driven de-mixing. We do not model implantation of ions and there are no surfaces, overlayers, or substrates in our system.

6.1 Model system and simulation setup

Many experimental investigations of RIM have been conducted on bilayers composed of low solid solubility face-centered cubic (fcc) and body-centered cubic (bcc) metals, including Cu-Nb [169, 78], Cu-Mo [78], Cu-Bi [78], Cu-V [17], Cu-W [170], Ag-Fe [171], and Cu-Fe [172]. These binary systems span a wide range of liquid-phase behaviors and therefore provide a good opportunity to study the effect of liquid phase properties on RIM. However, they also have a wide range of atomic mass ratios and

solid phase behaviors, making it challenging to unambiguously attribute differences in RIM to liquid phase properties alone.

To get around this problem, we decided to focus on just one fcc/bcc system, namely Cu-Nb, using three EAM potentials studied in Chapter 4 and 5. Each potential accurately describes the solid-phase portion of the equilibrium phase diagram of Cu-Nb, namely that the two elements do not form compounds and exhibit low solid solubility. Each potential also reproduces the solid phase dilute heats of mixing of Cu and Nb obtained from CALPHAD modeling [173]. Finally, short-range interactions in all three potentials follow the ZBL form [41], yielding identical high-energy scattering cross-sections. However, all three potentials exhibit markedly different liquid phase properties [159]. Naturally, only one of these potentials provides a best description of the Cu-Nb binary system. However, taken together, these three potentials provide an extremely convenient computational model system that enables us to unambiguously determine the effect of liquid phase properties on RIM, independent of other factors. These three potentials therefore span a range of liquid phase solubilities, from high (EAM3) to intermediate (EAM1) to low (EAM2) – a trend reflected in the liquid phase heats of mixing. This trend also correlates with variations in liquid excess volume and liquid phase structure.

To carry out simulations of RIM, we construct models containing a Cu and a Nb layer of equal thickness bonded together under periodic boundary conditions in all directions. The simulation cells are $\sim 15 \times 15 \times 15$ nm^3 in size and contain ~250,000 atoms. These models are large enough for collision cascades initiated by 10keV PKAs not to interact with their periodic images. However, they are also sufficiently small so that many thousands of cascades may be modeled in them in a reasonable time. To study the effect of interface crystallography on RIM, we constructed models containing three different types of interfaces. The exact model dimensions for each interface are chosen to minimize the strains needed to impose periodic boundary conditions.

Interface A is formed along closest packed planes, namely {111}Cu and {110}Nb. Within the interface plane, a <110>Cu direction is parallel to a <111>Nb direction. This interface is in the Kurdjumov-Sachs orientation relation and is observed

in physical vapor deposited Cu-Nb multilayers [174]. Interface B also exhibits the Kurdjumov-Sachs orientation relation, but has different interface planes than interface A, namely {112}Cu and {112}Nb. It is seen in Cu-Nb composites synthesized by severe plastic deformation, e.g. accumulative roll bonding (ARB) [12, 14] or accumulated drawing and bundling (ADB) [175, 176]. In interface C, a {001}Cu plane is joined to a {110}Nb plane and <100>Cu is parallel to <111>Nb within the interface. It has not been seen in any Cu-Nb composites to date. However, unlike A and B, this interface is not in the Kurdjumov-Sachs orientation relation, so we study RIM in it for comparison.

6.2 Modeling and measuring intermixing

6.2.1 Multiple collision cascade simulation

We model RIM by simulating multiple successive collision cascades initiated by 10keV PKAs. We begin by equilibrating the system at 100K and zero pressure for 5ps. Then, we select a PKA at random and assign it a velocity with random direction and magnitude corresponding to 10keV of kinetic energy. The model is then evolved in time under constant energy and volume for ~20ps with dynamically varying time steps to maintain numerical accuracy. Within the first 0.1-0.5ps of the simulation, the PKA dissipates most of its kinetic energy by scattering with surrounding atoms. Fully developed TSs form within 1-2ps of the initiation of a PKA. After 20ps, the TSs have quenched to near ambient temperature. At this time, we consider the collision cascade to have finished. We then bring the temperature back to 100K by velocity rescaling through a 5ps anneal. We then initiate another collision cascade by repeating the steps describe above. Using the SRIM code [90] and following the steps proposed by Stoller *et al.* [66], we estimate that one collision cascade in our simulation cell produces about $5 \cdot 10^{-4}$ displacements per atom (dpa), on average. We performed more than 10,000 collision cascades in most of our simulations, yielding a total dose of ~5 dpa.

6.2.2 Qualitative mixing history

Qualitative mixing histories were similar in all cases we studied. Figure 6-1 illustrates a typical mixing history, obtained using EAM1 and interface A, at four successive dose levels: 0, 1, 3.5, 5 dpa. Figure 6-1(a)-(d) show the distribution of Cu and Nb atoms at each dose, Figure 6-1(e)-(h) visualize the location of fcc, bcc, and amorphous atomic environments, determined using adaptive common neighbor analysis [177], and Figure 6-1(i)-(l) show composition profiles as a function of distance normal to the original location of the interface. The simulation begins with a perfectly sharp interface, as shown in Figure 6-1(a), (e), and (i). As the dose increases, the neighboring Cu and Nb gradually mix and the composition profile broadens. Numerous isolated impurity atoms may be seen in the crystalline Cu and Nb layers. Furthermore, an amorphous layer grows by consuming the neighboring fcc and bcc layers.

The amount of intermixing may be characterized by measuring the width of the composition profile, W_c, as a function of dose. W_c is determined as the distance between locations across the interface where the Cu composition is 20% and 80%. Figure 6-2 shows that W_c is proportional to the square root of dose, analogous to the variation of composition profiles with time in conventional Fickian diffusion. Figure 6-2 shows that the width of the amorphous layer, W_a, also increases as the square root of dose. Wa is determined as the distance between locations across the interface where the fraction of atoms with non-crystalline local structures is 50%. Since amorphous Cu-Nb only forms within a specific range of compositions [178], the growth of the amorphous layer is likely directly tied to the broadening of the composition profile.

After 3.5 dpa, Figure 6-1(g) shows that amorphous layers at neighboring interfaces form protrusions sufficiently wide to interact at isolated locations. Such protrusions are intermittent and may be either created or destroyed by successive collision cascades occurring in their vicinity. In this simulation, after 4 dpa, the size and frequency of protrusions becomes sufficiently high to form a persistent amorphous bridge across the intervening fcc layer, which subsequently amorphizes after an additional dose of 0.5 dpa, as shown in Figure 6-1(h).

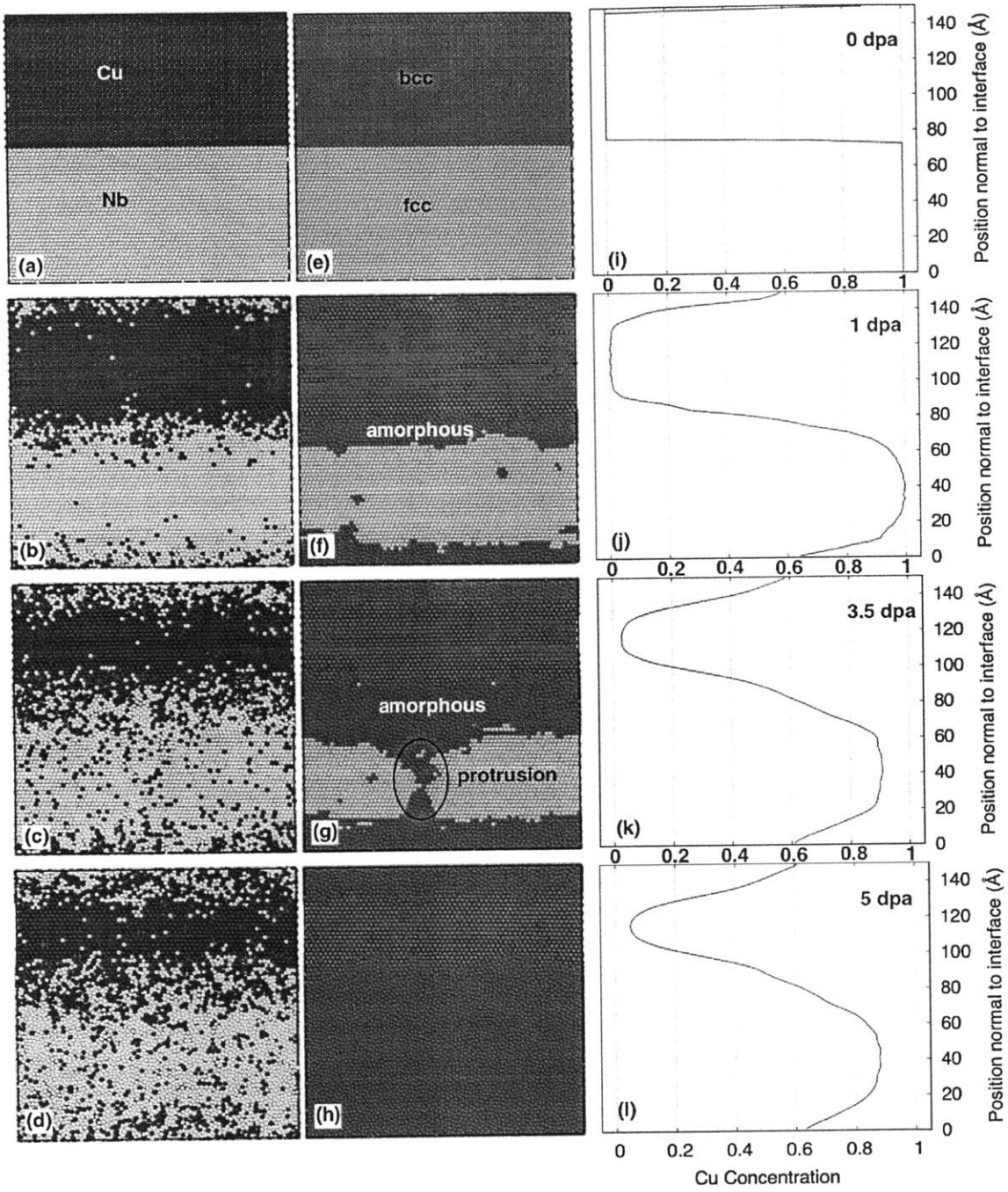

Figure 6-1: Cu-Nb bilayers colored by atom type (yellow: Cu; blue: Nb) are shown at 0, 1, 3.5, 5 dpa in (a), (b), (c) and (d), respectively. (e)-(f) show corresponding visualizations colored by local structure (green: fcc; red: bcc; gray: amorphous) while (i)-(i) show Cu concentration profiles.

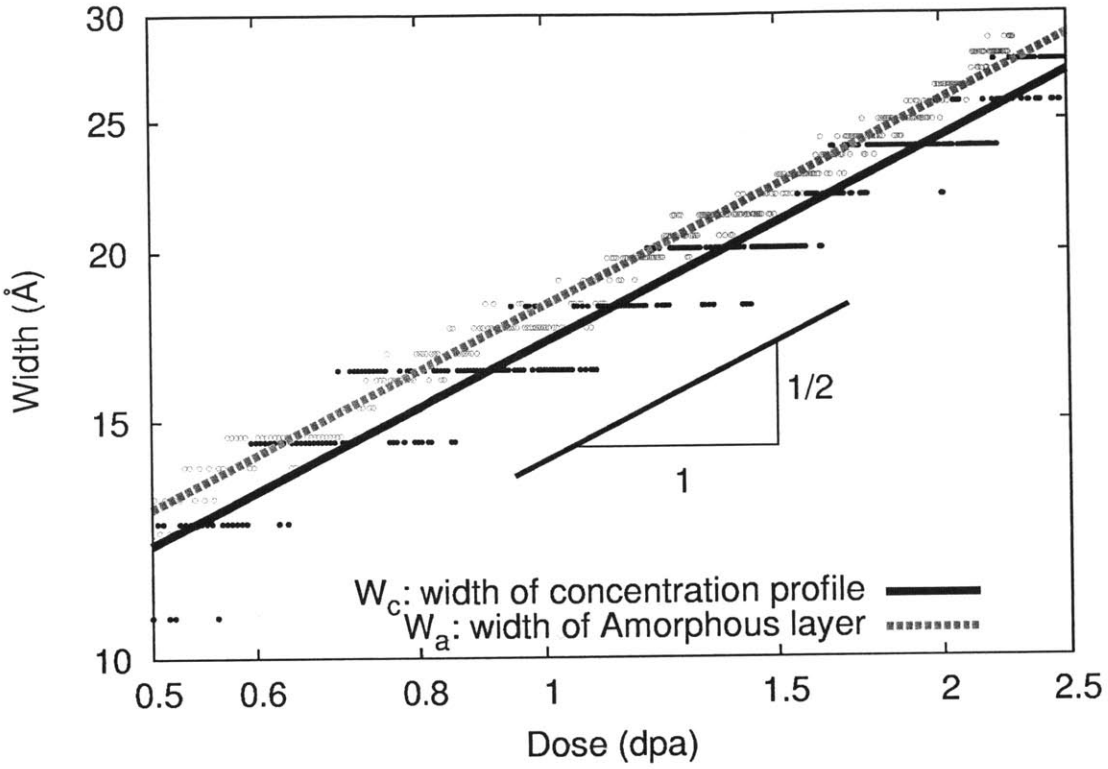

Figure 6-2: Log-log plot showing that concentration profile width, W_c, and amorphous layer width, W_a, increase in proportion to the square root of dose.

6.2.3 Mixing parameter

RIM rates may be characterized by the mixing parameter (MP): a quantity independent of dose as well as the energy and type of incident ions. The MP is defined as [78]

$$MP = \frac{D^{\text{eff}} t}{\phi F_D}, \tag{6.1}$$

where D^{eff} is the effective mixing interdiffusivity, t is irradiation time, ϕ is ion fluence, and F_D is the deposited nuclear energy per ion per unit depth. The MP therefore has units of $\text{Å}^5/\text{eV}$. The effective interdiffusion length, $\sqrt{D^{\text{eff}} t}$, may be obtained experimentally by fitting the measured composition profile across the interface to the solution of the diffusion equation.

By contrast, the usual way of measuring mixing in MD is to calculate the mean

squared displacement (MSD) [97]:

$$MP = \frac{\sum_i \left|\vec{r}_i(t) - \vec{r}_i(0)\right|^2}{6\rho_0 E_{Dn}}, \tag{6.2}$$

where $\vec{r}_i(t)$ is the position of atom i at time t, ρ_0 is atomic density, and E_{Dn} is the deposited energy. Similarly, MP can also be measured by MSD perpendicular to the interface [103]:

$$MP = \frac{\sum_i \left|z_i(t) - z_i(0)\right|^2}{2\rho_0 E_{Dn}}, \tag{6.3}$$

where $z_i(t)$ is the projection of the position of atom i at time t on the direction perpendicular to the interface. However, in our view, this approach does not give a measure of RIM that corresponds to the MP as defined in (6.1). For instance, when two atoms of the same type switch positions, MSD will increase. The method of analyzing MD simulations described above would therefore register an increment of mixing, even though the composition profile remains unaltered. Another illustration of the inadequacy of the MSD-based measure is that it may incorrectly indicate mixing even when in fact de-mixing occurs, for example when an impurity is displaced towards a region containing only atoms of its own type. Section 6.3.1 shows that MSD overestimates mixing rates, as expected.

We developed two methods of measuring RIM in MD simulations of flat interfaces that correspond directly to the MP. Instead of calculating MSD, we first compute the effective interdiffusivity, D^{eff}, in two different ways, and then derive the MP according to (6.1). The first method is to calculate the composition-independent D^{eff} based on an integral of the composition profile. Similar to experimental measurements, this approach determines the MP directly from the composition profile, except without having to fit to an error function.

Consider intermixing at an initially sharp interface at $x = 0$ with boundary conditions $c(\infty, t) = c^R$ and $c(-\infty, t) = c^L$. As shown in [133], at any given time t, the

flux and the composition-dependent interdiffusivity satisfy

$$\tilde{J} = -\tilde{D}(c)\frac{dc(x)}{dx} = \frac{1}{2t}\int_{c^R}^{c(x)} (x(c) - x_0)\, dc, \tag{6.4}$$

where x is a coordinate normal to the interface plane and x_0 is the position of the Matano plane,

$$x_0 = \frac{1}{c^L - c^R}\int_{c_R}^{c^L} x(c)dc. \tag{6.5}$$

The average, concentration-independent effective interdiffusivity may be computed by taking the integral of (6.4) and dividing by $\left(c^L - c^R\right)$:

$$D^{\text{eff}} = \frac{\int_{-\infty}^{\infty} \tilde{J}dx}{c^L - c^R}. \tag{6.6}$$

Following Dayananda [179, 180], we evaluate the integral in (6.6) by parts:

$$\int_{-\infty}^{\infty} \tilde{J}dx = \int_{-\infty}^{\infty} \tilde{J}d(x - x_0) = \tilde{J}(x - x_0)\Big|_{-\infty}^{\infty} - \int_{\tilde{J}(-\infty)}^{\tilde{J}(\infty)} (x - x_0)d\tilde{J}. \tag{6.7}$$

The first term on the right evaluates to zero because the mass flux at the two limits is zero. To evaluate the second term, we take the derivative of (6.4) with respect to c to find

$$d\tilde{J} = \frac{1}{2t}(x - x_0)dc. \tag{6.8}$$

Then, (6.7) becomes

$$\int_{-\infty}^{\infty} \tilde{J}dx = -\frac{1}{2t}\int_{c^L}^{c^R} (x(c) - x_0)^2\, dc. \tag{6.9}$$

Combing (6.1), (6.6), and (6.9), the MP may be expressed as

$$MP = \frac{D^{\text{eff}}t}{\phi F_D} = -\frac{\int_{c^L}^{c^R} (x(c) - x_0)^2\, dc}{2(c^L - c^R)\phi F_D}. \tag{6.10}$$

Equation (6.10) may be calculated by direct numerical integration of the composition

profile,

$$c(x) = \frac{n_1(x)}{n_1(x)\Omega_1 + n_2(x)\Omega_2}, \tag{6.11}$$

where $n_{1(2)}(x)$ is the number of type 1(2) atoms per unit distance at location x, measured perpendicular to the interface, and $\Omega_{1(2)}$ is the atomic volume of type 1(2) atoms, which is approximately constant in our case. To obtain a smooth composition profile from our MD simulations, we use a local convolution function to compute $n_{1(2)}(x)$:

$$n_{1(2)}(x) = \frac{\sum_{i=1}^{N_{1(2)}} \xi(x - x_i)}{\int \xi(x)dx}, \tag{6.12}$$

where

$$\xi(x - x_i) = \exp\left[-\frac{(x - x_i)^2}{B^2}\right], \tag{6.13}$$

$N_{1(2)}$ is the total number of type 1(2) atoms, and B is the smoothing length scale (we use $B = 2 \sim 4$Å).

Using this method, we calculate D^{eff} and from it the MP. One of its limitations, however, is that it is unable to assess the contributions of individual TSs to mixing because, even in a model as small as ours, the associated changes in the composition profile are too small to give a reliable estimate of the MP. Therefore, we propose a second way of determining the effective interdiffusivity as a weighted sum of intrinsic diffusivities:

$$D^{\text{eff}}(t) = c_2\Omega_2 D_1(t) + c_1\Omega_1 D_2(t), \tag{6.14}$$

where $c_{1(2)}$ is local concentration and $D_{1(2)}$ is the intrinsic diffusivity that relates flux of type 1(2) atoms to their concentration gradient by Ficks law in a local C-frame [133]. Assuming the intrinsic diffusivities are concentration independent, the average effective interdiffusivity is

$$D^{\text{eff}}(t) = \int_0^1 \left[c_2\Omega_2 D_1(t) + c_1\Omega_1 D_2(t)\right] d(c_1\Omega_1) = \frac{1}{2}\left(D_1(t) + D_2(t)\right). \tag{6.15}$$

Using the same boundary conditions as before, the composition-independent individ-

ual effective diffusivity for component 1(2) may be computed by taking the integral

$$D_{1(2)} = \frac{1}{(c^L - c^R)_{1(2)}} \int_{-\infty}^{\infty} x \frac{\partial c_{1(2)}}{\partial t} dx. \tag{6.16}$$

Using the definition of composition in (6.11), we may rewrite this equation in terms of $n_{1(2)}(x,t)$:

$$D_{1(2)} = \frac{1}{\Delta n_{1(2)}} \int_{-\infty}^{\infty} x \frac{\partial n_{1(2)}}{\partial t} dx, \tag{6.17}$$

where $\Delta n_{1(2)}(t) = n_{1(2)}(-\infty, t) - n_{1(2)}(\infty, t)$.

To evaluate the time derivative in (6.17), we re-express $n_{1(2)}(x,t)$ as the sum of Dirac delta functions

$$n_{1(2)}(x,t) = \sum_{i=1}^{N_{1(2)}} \delta(x - x_{i,1(2)}, t). \tag{6.18}$$

The change in $n_{1(2)}(x,t)$ due to a single cascade of during δt may be written as

$$n_{1(2)}(x, t+\delta t) = \sum_{i=1}^{N_{1(2)}} \delta\left(x - (x_{i,1(2)} + \delta x_{i,1(2)}), t\right). \tag{6.19}$$

where $\delta x_{i,1(2)}$ is the displacement of atom i. We then approximate

$$\frac{\partial n_{1(2)}}{\partial t} \approx \frac{n_{1(2)}(x, t+\delta t) - n_{1(2)}(x,t)}{\delta t}. \tag{6.20}$$

Thus, the intrinsic diffusivity is

$$D_{1(2)} \approx \frac{1}{\Delta n_{1(2)} \delta t} \int_{-\infty}^{\infty} x \left[n_{1(2)}(x, t+\delta t) - n_{1(2)}(x,t) \right] dx. \tag{6.21}$$

Combining (6.18), (6.19) and (6.21), we have

$$\begin{aligned} D_{1(2)} &\approx \frac{\int_{-\infty}^{\infty} x \sum_{i=1}^{N_{1(2)}} \left[\delta\left(x - (x_{i,1(2)} + \delta x_{i,1(2)}), t\right) - \delta\left(x - x_{i,1(2)}, t\right) \right] dx}{\Delta n_{1(2)}(t) \delta t} \\ &= \frac{Z_{1(2)}(t)}{\Delta n_{1(2)}(t) \delta t}, \end{aligned} \tag{6.22}$$

where $Z_{1(2}(t) = \sum_{i=1}^{N_{1(2)}} \delta x_i$ is defined the mixing displacement of type 1(2) atoms.

Finally, substituting (6.22) into (6.15), the effective interdiffusivity may be expressed as

$$D^{\text{eff}}(t) = \frac{1}{2}\left(D_1(t) + D_2(t)\right) \approx \frac{1}{2\delta t}\left(\frac{Z_1(t)}{\Delta n_1(t)} + \frac{Z_2(t)}{\Delta n_2(t)}\right). \tag{6.23}$$

Expression (6.23) may be evaluated for any time interval in the mixing process, including the entire simulation, individual cascades, or parts of individual cascades. The effective interdiffusivity given in (6.23), however, has been derived from changes of the concentration profile of the entire system. To evaluate the effective interdiffusivity inside single TS, (6.23) must be scaled by the volume fraction λ that a singe TS occupies:

$$D_{\text{TS}}^{\text{eff}}(t) \approx \frac{\delta t}{\lambda} D^{\text{eff}}(t) \approx \frac{1}{2\lambda}\left(\frac{Z_1(t)}{\Delta n_1(t)} + \frac{Z_2(t)}{\Delta n_2(t)}\right). \tag{6.24}$$

In our simulations, $\lambda \approx 0.037$. If the duration δt of each cascade is identical and the boundary conditions do not change, then the contributions of all cascades to the average effective interdiffusivity are additive. The system-average MP may then be computed as

$$MP = \frac{\sum D^{\text{eff}}(t)\delta t}{0.5\phi F_D} \approx \frac{1}{\phi F_D}\sum_{t_i}\left(\frac{Z_1(t)}{\Delta n_1(t)} + \frac{Z_2(t)}{\Delta n_2(t)}\right). \tag{6.25}$$

where the factor of 0.5 accounts for the fact that there are two interfaces in our model, but on average only half of the ion fluence contributes to intermixing at each interface. Furthermore, the uncertainty of the MP may be computed using this method by calculating the standard deviation of the average MP for thousands of TSs. Note that the MP calculated by this method excludes any atomic displacements that do not lead to mixing, so it should correspond more closely to experimental measurements than the usual MSD-based calculation.

6.3 Factors affecting average intermixing rates

6.3.1 Liquid phase thermodynamics

To assess the influence of liquid phase thermodynamics on average RIM rates, we performed multiple collision cascade simulations up to doses of ~5dpa using the three EAM potentials described in Chapter 4 and 5. All of these simulations were performed on interface A. Table 6.1 lists the MP values determined from these simulations via the two methods described in Section 6.2 and compares them with MPs determined by MSD calculations. MPs calculated based on the two methods in Section 6.2 are in excellent agreement with each other. The MSD-based methods overestimate RIM rates in all three cases, as expected. They will not be used further in the present study.

The experimentally determined MP for Cu-Nb at 6K is 7Å^5/eV [78], which is within the uncertainty of the value found using EAM1: 8.2 ± 1.6 Å^5/eV. Of the three potentials, EAM1 best reproduces the liquid portion of the experimental equilibrium phase diagram of Cu-Nb. By contrast, MPs computed using EAM2 and EAM3 respectively underestimate and overestimate the experimental MP. This result demonstrates that liquid phase properties do have an important influence on RIM. The mechanisms responsible for these differences will be investigated in detail in the following sections.

The experimentally determined MP at 6K for Cu-Mo, which has a liquid phase miscibility gap, is 2Å^5/eV [78]. This result cannot be compared directly with any of our simulations because of the differing solid-phase properties of the Cu-Mo and Cu-Nb systems. It is nevertheless interesting to note that the MP found using EAM2, which also has a large liquid phase miscibility gap, is 4.1 ± 2.2Å^5/eV, i.e. close to that of Cu-Mo.

6.3.2 Ballistic displacements

To assess the relative contribution of ballistic displacements and TSs to mixing, we perform simulations where TSs are generated without any ballistic displacements.

Table 6.1: Mixing parameter (MP) values, in units of $Å^5/eV$, for the three potentials determined by four different methods.

Method	From concentration profile Eq.(6.10)	From atomic displacement Eq.(6.25)	MSD Eq.(6.2)	MSD perpendicular to interface Eq.(6.3)
EAM1	8.3	8.2±1.6	15.3	13.2
EAM2	4.3	4.1±2.2	15.3	13.0
EAM3	25.5	23.6±2.3	24.9	26.1

The time history of average temperature and number of atoms inside TSs is nearly identical for all three potentials. Figure 6-3 shows an illustrative TS time history. In the first ~0.3 ps, atoms undergo ballistic displacements, raising the average TS temperature. After 0.3 ps, the TS begins to shrink and temperature gradually decreases. We perform a series of simulations in which each TS is initiated at a random location within the simulation cell by raising the average temperature to 4000K in a spherical region 70Å in diameter and centered on the selected location. The temperature and size of this spherical region are chosen to mimic a TS arising from a 10keV PKA at the moment when the TS is largest, as illustrated on Figure 6-3. The remainder of the simulation and the analysis of the results proceed exactly as previously described. In this way, we exclude the effect of ballistic mixing and simulate only the effect of TSs on mixing.

These TS-only simulations yield MPs of 8.6, 4.0, 24.8 $Å^5/eV$ in EAM1, EAM2 and EAM3, respectively. These values are nearly identical to those found in simulations that modeled complete collision cascades initiated by 10keV PKAs (Table 6.1). In addition, amorphous interfacial layers develop in the TS-only simulations, just as in the complete collision cascade simulations. Thus, we conclude that RIM in Cu-Nb occurs within TSs and the effect of ballistic mixing is negligible.

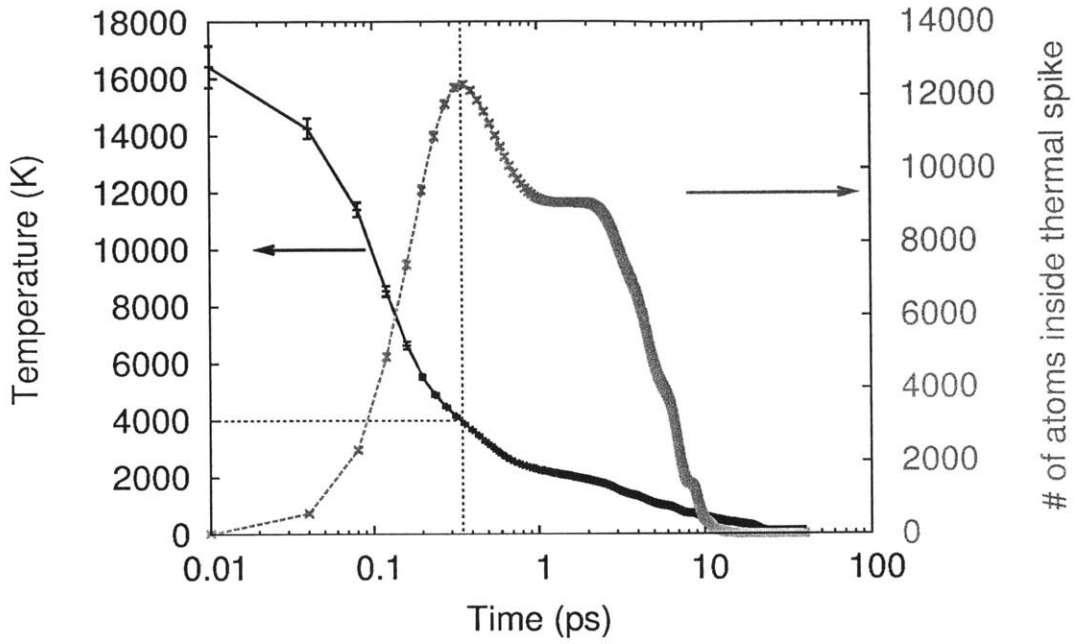

Figure 6-3: Time history of average temperature and number of atoms within a TS. At the moment when the TS is largest, its average temperature is ~4000K.

6.3.3 Interface crystallography

To assess the influence of interface crystallography on RIM, we performed multiple collision cascade simulations to ~5 dpa on the three interface structures described in Section 6.1, using potential EAM2 for all of them. MPs found for Interface A, B, and C are 4.3, 4.4, and 4.4 $Å^5/eV$, respectively. There is no significant difference between these three values, indicating that, in the absence of thermally activated recovery processes, RIM is independent of interface crystallography.

6.4 Cascade-level analysis of mixing

6.4.1 Contribution of individual cascade to mixing

As the dose increases, the structure of the Cu-Nb model changes drastically from a bilayer with atomically sharp interfaces to a system containing vacancies, self-interstitials, impurities, point defect clusters, amorphous layers, and interfaces with

continuous concentration gradients. Therefore, TSs occurring at different locations in the model may contribute differently to RIM. We attempted to characterize the contribution of individual cascades to mixing using a variety of analysis methods, including TS compactness [48], changes in atomic bond angle distributions [181, 182], Voronoi volume [183], short-range order [184, 166], and structural factors [167]. However, the method that yielded the clearest insights into local mixing processes was the second technique for computing interdiffusivity described in Section 6.2.3, Eq. (6.24).

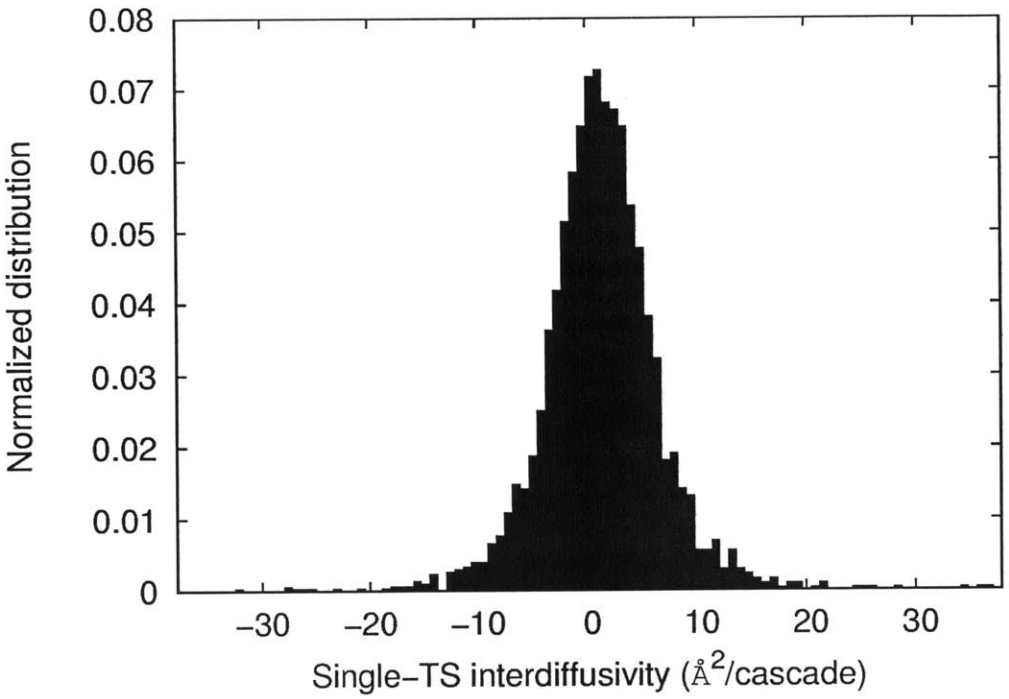

Figure 6-4: Distribution of single-TS interdiffusivities for the first 3000 collision cascades in Interface A modeled by EAM1.

Figure 6-4 shows a histogram of single-TS interdiffusivities computed for the first 3000 collision cascades (0 to 1.5 dpa) in our simulation of RIM using EAM1 and interface A. The distribution has a mean of $\sim$1.30Å^2/cascade with standard deviation $\sim$5.30Å^2/cascade. As stated in Section 6.3.1, this result agrees well with the average interdiffusivity computed directly from the concentration profile. However, Figure 6-4 also demonstrates that the distribution of individual TS interdiffusivities is rather

broad, with outliers up to six standard deviations away from the mean. Some single-TS interdiffusivities may even be negative when the mixing displacements defined in (6.22) are negative, even though the average interdiffusivity is positive. This is because the average interdiffusivity is the resultant of the many random walk processes that occur within individual TSs, each of which might deviate from the average to a greater or lesser extent. Therefore, assessing the contribution to mixing of cascades occurring at different locations requires averaging over many hundreds or thousands of cascades.

6.4.2 Collision cascade location

In our simulations, PKAs are chosen at random. However, the distance traveled by the PKA before initiating a TS may depend on the atomic structure of the model. Therefore, the distribution of TSs in the system might not be random. To assess the influence of TS location in mixing, we classified TSs into two types, as illustrated in Figure 6-5: Type I, which center on the interfaces, and Type II, which center on the crystalline Cu or Nb layers. A TS is considered Type II if more than half of the atoms in it are in a crystalline layer. Otherwise, it is classified as Type I.

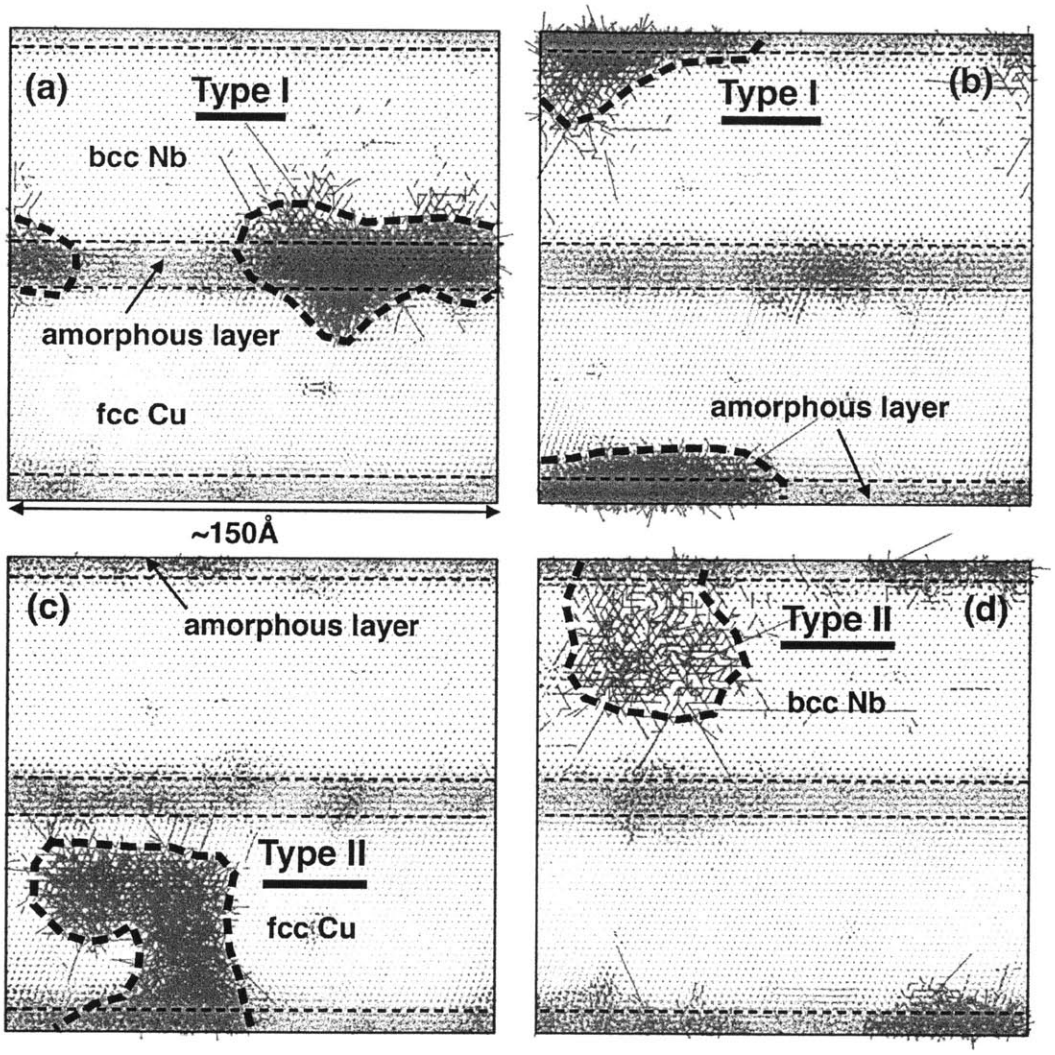

Figure 6-5: Displacement vector fields of collision cascades that initiate TSs at different locations: (a)(b) Type I, when a TS centers on an interface, and (c)(d) Type II, when the TS centers on a crystalline Cu or Nb layer. The dashed curves indicate TSs. Although (b) may appear to contain two TSs, this is actually just one TS under periodic boundary conditions.

Table 6.2: Average single-TS interdiffusivity ($Å^2$/cascade) for Type I, Type II, and all TSs and all three EAM potentials.

Potential	Type I	Type II	All
EAM1	1.43±0.23	1.14± 0.27	1.31±0.25
EAM2	-0.21±0.32	1.43±0.31	0.66±0.36
EAM3	4.81±0.22	2.01±0.36	3.76±0.37

When the amorphous layer is ~20Å thick and the crystalline layers are ~55Å thick, approximately 56% of the TSs are Type I. As dose increases, the amorphous layer thickness increases and the percentage of Type I cascades increases, as well. Thus, more TSs form near the interfaces than in the crystalline layers, even when the interfacial region constitutes a minority of the model volume. The likely reason for this is that some PKAs may channel through crystalline layers, but are less likely to pass through the interface because of the change in crystallography that occurs there as well as due to the amorphous layer.

We computed average single-TS interdiffusivities using (6.24) for Type I and II TSs that occurred within the first 2000 collision cascades (0 to 1 dpa) in our simulations of RIM at interface A using all three potentials. The outcomes are listed in Table 6.2. The effective interdiffusivity for Type I TSs follows the same trend as the average interdiffusivity for all TS, i.e. least for EAM2, greatest for EAM3, and intermediate for EAM1. The effective interdiffusivity of Type I TSs under EAM2 is close to zero. Unlike Type I TSs, effective interdiffusivities for Type II TSs are nearly equal for all three potentials. The variability in the average interdiffusivity for all TSs is therefore due to differences in interdiffusivity for Type I TSs. However, mixing in Type II TSs is not negligible. In fact, it accounts for the majority of the effective interdiffusivity in EAM2.

6.4.3 Time history of mixing inside thermal spikes

To learn about the mechanisms of mixing within TSs, we analyzed the detailed time history of mixing within 100 TSs for simulation using all three EAM potentials. For

EAM1 and EAM2, we obtained these 100 time histories from TSs occurring at a dose of ~1 dpa while for EAM3 we obtained them from at a dose of~0.2 dpa. This way, the amorphous layer thickness for each potential was ~15Å and the proportion of Type I and Type II TS was approximately the same. To understand the roles of Cu and Nb atoms in mixing, we measure the average mixing displacement of both Cu and Nb atoms inside the TS, defined in (6.22) as $Z_{1(2)} = \sum_{i=1}^{N_{1(2)}} \delta x_i$.

Figures 6-6(a) and (b) show mixing displacements of Cu and Nb atoms for Type I and Type II TSs, respectively, averaged over the 100 TSs. The thickness of the plotted curves in Figure 6-6 equals two times the uncertainty of the average mixing displacements. Although in some cases the uncertainties are large, some trends may nevertheless be discerned. In all cases, mixing occurs within the first 1 or 2 ps of the TS, followed by gradual and incomplete de-mixing over the following ~20ps. Mixing displacements are largest for Cu atoms in Type I cascades. The final mixing displacement values at the end of the TS are different for the three potentials and follow the mixing trends described previously: greatest for EAM3, least for EAM2, and intermediate for EAM1.

The mixing displacements for Nb in Type I TSs are initially negative, as if uphill diffusion were taking place. Moreover, after the first ~5ps of the TS, there are large fluctuations reminiscent of ringing in all the mixing displacement curves shown in Figure 6-6(a) and (b). Both the negative mixing displacements for Nb in Figure 6-6(a) and the aforementioned fluctuations are in fact due to the pressure pulse generated from the initial expansion of the hot TS core. The pulse reflects from the surrounding matrix atoms, giving rise to periodic fluctuations in the mixing displacement curves. However, because these displacements are in fact reversible, elastic displacements in the liquid, they should not be counted as truly contributing to mixing. To remove them from our calculation, we relax every structure in every TS to its closest inherent structure by minimizing its potential energy using the conjugate gradient method.

Figures 6-6(c) and (d) show mixing displacements re-calculated in the relaxed configurations. As expected, the Nb mixing displacements in Type I TSs are positive. The pressure-induced periodic oscillations are greatly reduced, but not entirely

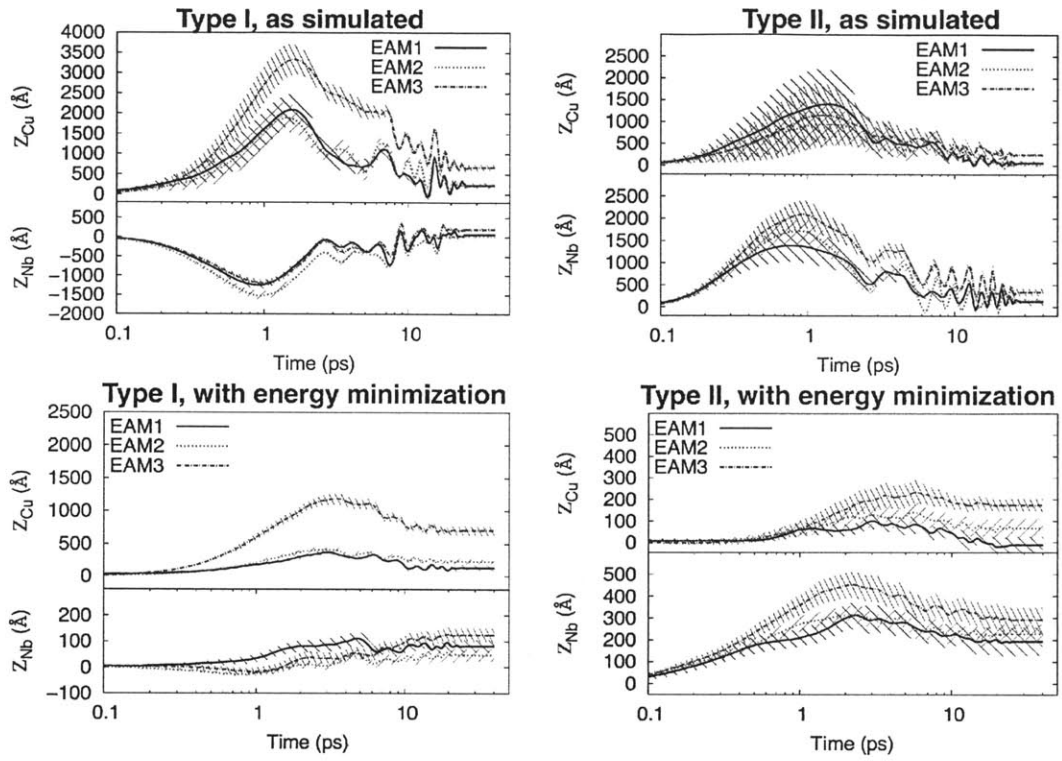

Figure 6-6: Mixing displacements for Cu and Nb atoms averaged over 100 TSs in simulations using all three EAM potentials. As-simulated (a) Type I and (b) Type II. (c) Type I and (d) Type II TSs after energy minimization. The width of the plots equals twice the standard deviation of the average mixing displacements.

removed, suggesting that some reversible mixing may occur during these pressure oscillations. Peak mixing displacements are also smaller in the relaxed configurations, showing that part of these displacements in the as-simulated configurations is also due to the initial pressure pulse. The standard deviations of the mixing displacements are smaller in the relaxed configurations than in the as-simulated ones, likely because the latter do not include the random atomic displacements associated with non-zero temperature.

Mixing displacements in the relaxed structures are qualitatively similar to those in the as-simulated configurations, but yield finer insight into the dependence of mixing on TS type and EAM potential due to their smaller standard deviations. All three potentials give rise to relatively small, nearly equal mixing displacements in Type II TSs for both Cu and Nb atoms. For Type I TSs, mixing is followed by incomplete

de-mixing in the case of Cu atoms. However, Nb atoms in Type I TSs only exhibit gradual mixing and no de-mixing for any of the three potentials.

6.5 Mechanisms of mixing in thermal spikes

6.5.1 Liquid phase interdiffusion

Liquid phase interdiffusivity has been calculated in Chapter 5 using two different methods, both yielding excellent agreement. To illustrate the relation between liquid phase interdiffusivity and RIM, Figure 6-7 plots average single-TS interdiffusivities determined from RIM simulations against liquid phase interdiffusivites obtained by direct MD of liquid phase interdiffusion. There is a nearly linear relationship between these two quantities with a proportionality factor of 1.3ps/cascade, i.e. approximately equal to the period of time in which mixing occurs within individual TSs, as shows in Section 4.3. Thus, liquid phase interdiffusion is able to account quantitatively for RIM rates.

The linear relation between liquid phase interdiffusivities and single-TS interdiffusivities is even more apparent for Type I TSs, confirming the importance of liquid phase behavior in RIM. However, these two quantities are not proportional to each other because the total effective interdiffusivity is also affected by de-mixing in the later stages of TSs, as shown in Section 4.3. By contrast, the single-TS interdiffusivities of Type II TSs are approximately independent of average liquid interdiffusivity. The reason for this is that, in Type II TSs, atom fractions are either close to 0 or 1. According to (5.27), the composition-dependent liquid phase interdiffusivity will then depend primarily on s_3 and $D^*_{1(2)}$, which are very similar for all three potentials, as shown in Table 5.1. Therefore, single-TS interdiffusivities of Type II TSs are nearly equal for all three potentials.

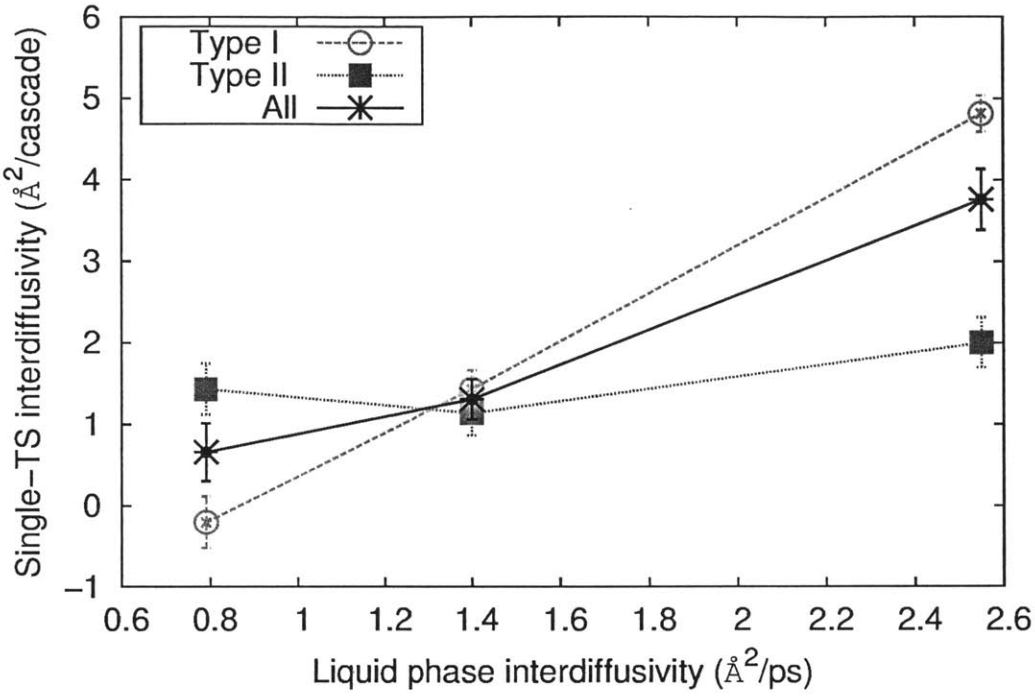

Figure 6-7: Correlations between single-TS interdiffusivity and liquid phase interdiffusivity for Type I, Type II, and all TSs.

6.5.2 De-mixing by solute segregation to the liquid

After mixing during the first 2-3ps of a TSs, the total mixing displacement begins to decrease, signaling de-mixing. The existence of a liquid phase miscibility gap in EAM2 suggests that de-mixing might occur by liquid phase separation. However, we also observe de-mixing in TSs modeled by EAM1 and EAM3, neither of which has a liquid phase miscibility gap. We therefore search for other mechanisms that may be responsible de-mixing in TSs.

Lopasso and Caro [185, 186] reported that radiation-induced solute segregation in a homogenous equilibrium Au-Ni solid solution is due to thermo-migration inside TSs. Caro *et al.* built a rigorous analytic model to study the heat and mass transport in nanoscale phase transitions induced by collision cascades [187]. Since temperature gradients from the center of a TS to its surroundings are very large in our simulationson the order of $10^{13} - 10^{14}$K/m – we investigate whether thermo-migration might

account for de-mixing in our simulations. We measured the heat of transport in Cu and Nb and used it to develop a one-dimensional continuum mixing model that incorporates both thermo-migration and interdiffusion [133]. However, we found that this model cannot explain the large amount of de-mixing shown in Section 5.4.3.

Figure 6-6 shows that de-mixing initiates after 2-3 ps, when the edges of the liquid TS core begin to crystallize. We therefore hypothesize that de-mixing occurs by segregation of solid phase impurities into the receding liquid, in analogy to zone refining [188]. To test this hypothesis, we calculate solute displacements at a moving liquid-solid interface using MD. We start from a Nb liquid-solid structure co-existing in thermal equilibrium at ~3000K with 5% Cu impurities distributed uniformly throughout the model, as shown in Figure 6-8(a). Then, heat is gradually removed by reducing atomic kinetic energies while conserving the aggregate linear momentum. In response, the solid phase grows at the expense of the liquid. For each potential, the rate of heat removal is adjusted to yield a solid-liquid interface velocity of ~1Å/ps, which approximately matches the TS shrinkage rate.

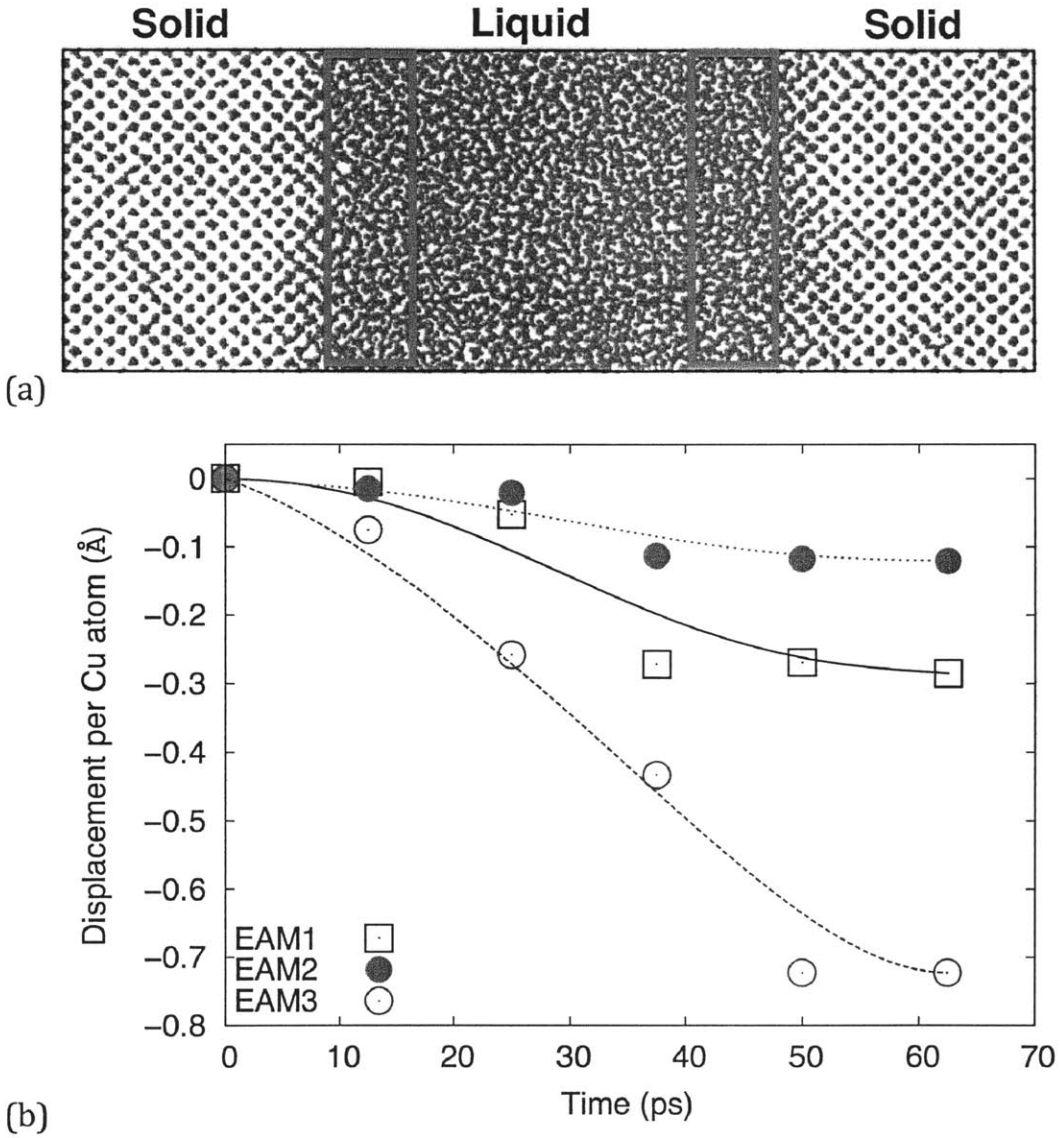

Figure 6-8: (a) Initial state of a MD simulation of solidification of a Cu-Nb liquid. Cu is red and Nb blue. (b) Average displacement per atom for Cu atoms within liquid regions that crystallized in the course of the simulation [indicated by red boxes in (a)]. Negative values denote movement away from the solid and towards the liquid.

During the simulation, Cu impurities segregate from the solid to the liquid and are swept deeper into the liquid by the moving solid-liquid interface. The phenomenon may account for the partial de-mixing of Cu atoms in TSs seen in Figure 6-6. We compute the average displacement per atom of Cu impurities perpendicular to the solid-liquid interface and plot them as a function of time in Figure 6-8(b). We also perform a similar MD simulation for a Cu solid-liquid interface with 2% Nb impurities. However, we find nearly no tendency for Nb to segregate preferentially to the liquid. This finding also agrees with Figure 6-6, which shows no de-mixing of Nb atoms in TSs.

After ~50ps, the average displacement per Cu impurity obtained from MD is 0.27Å for EAM1, 0.13Å for EAM2, and 0.72Å for EAM3. When the amorphous layer is ~15Å thick, the concentration of Cu impurities in the bcc Nb crystal is ~13%. For each potential, a typical TS contains about 6000 Cu atoms (and ~3000 Nb atoms). Thus, assuming that ~13% of these atoms contribute to de-mixing, we estimate that the de-mixing displacement of Cu per TSs is ~210Å for EAM1, ~101Å for EAM2, and ~546Å for EAM3. These estimates are in qualitative agreement with the de-mixing displacements shown in Figure 6-6.

6.5.3 Analytic model of radiation-induced mixing

For immiscible metal pairs, RIM occurs inside the liquid cores of TSs. It begins with mixing by liquid phase interdiffusion. Interdiffusivity depends on local composition, giving rise to different rates of RIM near interfaces and inside crystalline layers with low impurity concentrations. As shown in Section 6.5.1, liquid phase interdiffusivity may be reliably calculated from the free energy of the liquid phase.

Interdiffusion in TSs is followed by partial de-mixing by segregation of impurities to the liquid during solidification of the TS core. We attempted to develop analytical expressions describing this process based on existing models of zone refining [188]. However, these models were not able to account for the MD simulation results in Section 6.4.3 because they assume quasi-static segregation under local thermal equilibrium. This assumption is unlikely to hold for the rapid rates of quenching (10^{14}

K/s) and solid-liquid interface motion (~102 m/s) characteristic of TSs.

The development of a complete, mechanistically-informed analytical expression for mixing parameters (MPs) describing RIM in low solubility metals therefore requires further study of the non-equilibrium segregation of impurities during rapid TSs crystallization. Nonetheless, Figure 6-7 shows a linear relation between single-TS and liquid phase interdiffusivities. Therefore, we write the following phenomenologically motivated expression for MPs determined in our study:

$$MP = \frac{D^{\text{eff}}t}{\phi F_D} \approx \frac{\kappa V_{mboxTS}\bar{D}}{E_D}. \tag{6.26}$$

Here, $\bar{D}$ is the average liquid phase interdiffusivity at 4000K, V_{mboxTS} is the average volume of TSs, E_D is the deposited energy per TS, and κ is the proportionality factor between single-TS and liquid phase interdiffusivity in Figure 6-7, namely ~1.3ps/cascade.

Chapter 7

Radiation-Induced Mixing in Multilayers

In this Chapter, molecular dynamics (MD) is used to study radiation-induced mixing in Cu-Nb multilayer composite with individual layer thicknesses in the nanometer range. When the layer thickness is down to a few nanometers, a single large thermal spike initiated by energetic heavy ion or neutron may overlap a few alternating layers, which may lead to enhanced intermixing across interfaces and promote morphological instabilities in these materials.

7.1 Molecular dynamics simulation

We carry out our investigation in atomic models of Cu-Nb multilayers, such as the one shown in Figure 7-1(a). Composites with four different individual layer thicknesses are investigated: 10Å, 18Å, 32Å and 37Å. Our models reproduce the crystallography of magnetron sputtered Cu-Nb multilayers, where Cu and Nb are in the Kurdjumov-Sachs orientation relation and the interfaces between them lie along closest packed planes ({111} in Cu and {110} in Nb) [174]. The simulation cells are cubic with ~300Å edge lengths and contain approximately 1.9 million atoms, each. We use the Cu-Nb embedded atom method (EAM) potential constructed in Chapter 4, namely EAM1.

Collisions of neutrons or heavy ions with atoms in the multilayer are modeled by imparting a large kinetic energy – several tens of keV or more – to randomly selected Cu or Nb "primary knock-on atoms" (PKAs). The initial structure is first equilibrated at 300K and zero pressure for 5ps, followed by initiation of a 100keV PKA with a randomly selected velocity direction. The system is then allowed to evolve under constant energy and volume for up to 200ps with dynamically varying time steps to maintain both high numerical accuracy and simulation efficiency. Ten such simulations are conducted for each layer thickness independently. For 100keV PKAs, electronic stopping in Cu and Nb accounts for only about 10% of the stopping power [41] and is therefore ignored.

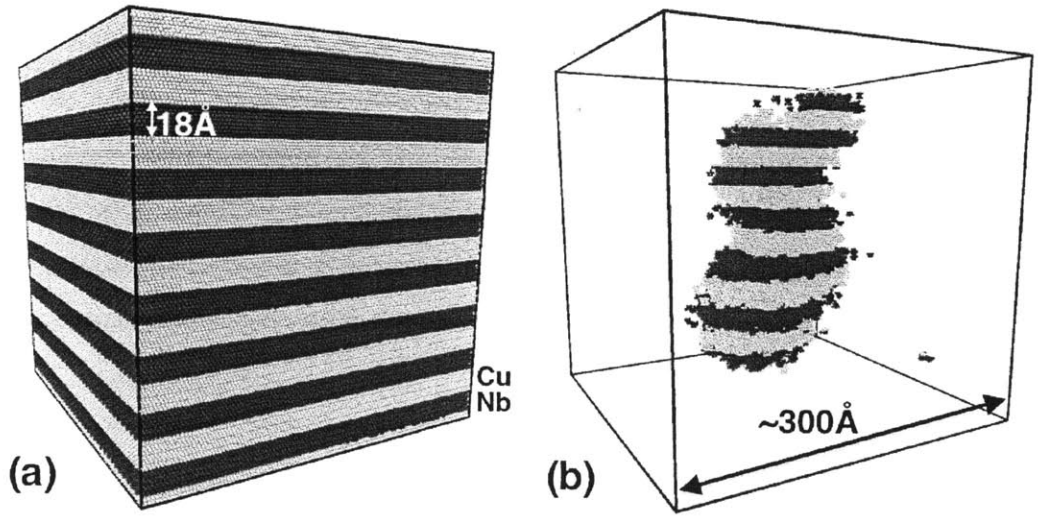

Figure 7-1: (a) An atomic model of a Cu-Nb multilayer nanocomposite with 18Å-thick layers. (b) A collision cascade initiated by a 100keV PKA spans multiple layers.

As a PKA moves through the multilayer, it initiates a collision cascade, dissipating its kinetic energy through numerous collisions with surrounding atoms until it comes to rest. These collisions may lead to breakdown of the layered morphology of the composite by displacing atoms ballistically over distances larger than a layer thickness, or by creating transient pockets of molten material where rapid interdiffusion takes place (as shown in Chapter 6). To identify collision cascade-affected regions, we subdivide the system into cubic voxels with ~6Å edge length and calculate the

local temperature by averaging the kinetic energy of all atoms in each voxel. In our simulations, regions where dissipation of PKA energy leads to local temperatures exceeding 1000K (i.e. more than three times the ambient temperature) are connected and have characteristic dimensions of 100-200Å, spanning multiple layers of Cu and Nb, as shown in Figure 7-1(b).

7.2 Results

After a collision cascade has come to completion, we search for intermixed regions where originally atomic sharp interfaces break down. To determine whether a layer has pinched off, we determine the concentration of impurities in cylindrical regions with a basal diameter of 10Å and spanning the entire thickness of the layer. If, at any location within a layer, there is a single cylinder across which the concentration of impurities is everywhere greater than a certain cutoff (i.e. 10%, 20%, 30%), we consider the layer as having pinched off. Figure 7-2(a) shows an example of a location where a layer is identified as having pinched off according to this criterion. By contrast, in Figure 7-2(b) isolated impurities have been created, but no pinch-off occurred. Figure 7-2(c) plots compositions across cylinders spanning these two regions, illustrating how the pinch-off criterion is applied quantitatively.

By analyzing all layers in all the simulations, we obtained the number of pinched-off layers as a function of layer thickness under various concentration cutoffs, shown in Figure 7-3. When the layer thickness increases, the number of breakdown layers decreases, indicating thicker layer tends to be more stable.

To better understand the morphological stability of Cu-Nb multilayers under neutron and heavy ion irradiation, we interpret our results in light of current understanding of radiation-induced mixing. The dissipation of energy by a PKA may be roughly divided into two stages: the ballistic phase and the thermal spike. In simulations such as ours, the ballistic phase and thermal spike may be readily distinguished by the number of atoms participating in a collision cascade as a function of time, as shown in Figure 7-4. We calculated the number of atoms inside each collision cascade

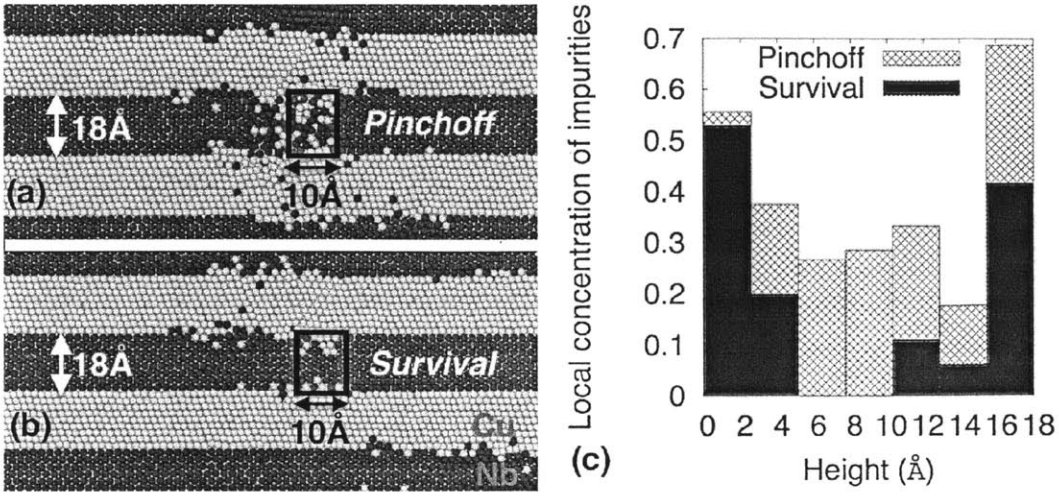

Figure 7-2: Locations in cascade-affected regions where a layer has (a) pinched off and (b) survived. (c) Local concentration of impurities as a function of distance from the bottom interface in the two regions marked with rectangles in (a) and (b).

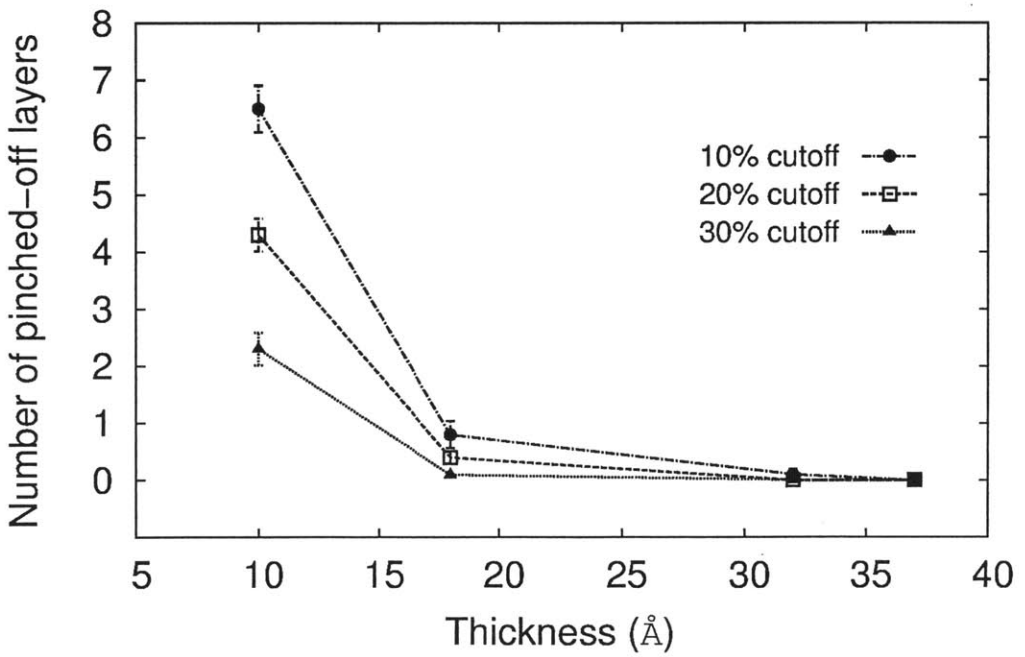

Figure 7-3: Number of pinched-off layers decreases as layer thickness increases at different impurities concentration cutoffs.

by summing up all the atoms in voxels with temperatures exceeding 1000K. After about 0.2~0.5ps, the collision cascade reaches its maximum size, indicating the end

of the ballistic phase. During the thermal spike, the number of atoms in the cascade decreases as kinetic energy is conducted away to the surrounding material.

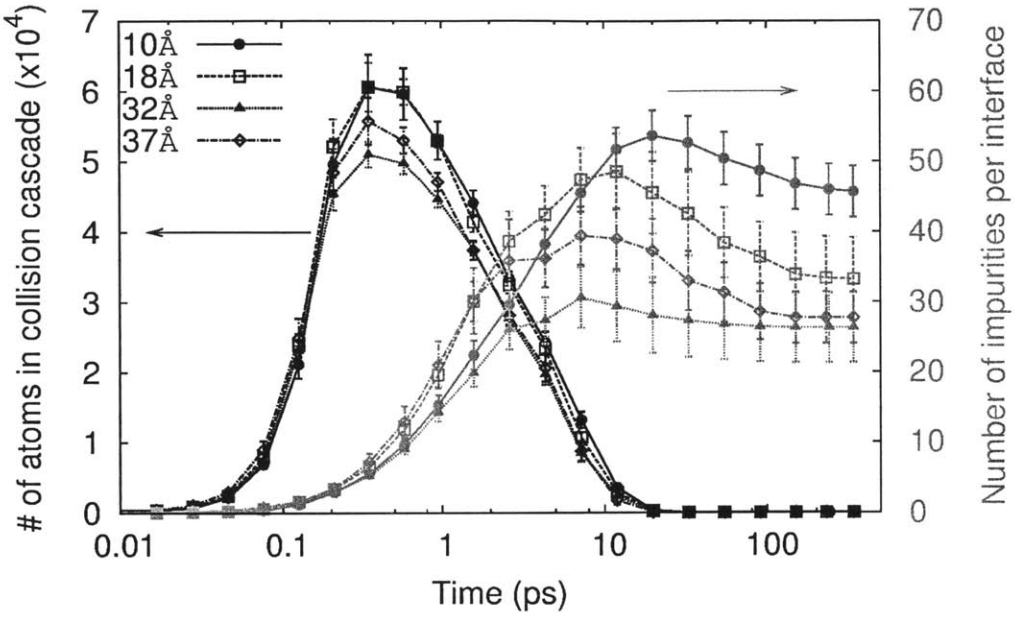

Figure 7-4: Average number of atoms inside collision cascades and average number of impurities per interface as a function of layer thickness.

The total amount of mixing as a function of time is quantified by the number of impurities (Cu in Nb layers or Nb in Cu layers) per interface in the model and is also plotted in Figure 7-4. It shows that limited intermixing occurs during the ballistic phase and most mixing occurs within the thermal spike. The mixing rate decreases over time and eventually even becomes negative, giving rise to limited local de-mixing. These findings indicate that mixing in Cu-Nb multilayers does not take place by ballistic displacements, but rather by interdiffusion within the liquid cores of thermal spikes, which agrees with the intermixing at isolated interfaces as discussed in Chapter 6.

If mixing across each interface were independent of mixing at neighboring interfaces, the number of impurities per interface would be a constant independent of layer thickness. This is indeed the case for layer thicknesses of 32Å and 37Å. Figure 7-4, however, demonstrates that for layer thicknesses below 32Å, the number of impuri-

ties per interface after a thermal spike does depend on layer thickness: nanolayered composites with thinner layers exhibit more intermixing per interface than those with thicker layers. Thus, mixing across an interface in a nanocomposite with sufficiently thin layers is not independent of mixing across neighboring interfaces, but rather is enhanced by it. This enhancement likely arises from the overlap of regions of interdiffusion formed at neighboring interfaces during a thermal spike. Using molecular dynamics, we calculated interdiffusivity in liquid Cu-Nb at temperatures characteristic of thermal spikes and computed that the characteristic interdiffusion distance over the lifetime of a thermal spike is $\sim$10Å. Thus, regions of interdiffusion at neighboring interfaces are expected to overlap in the multilayer models with layer thicknesses of 18Å and 10Å.

Chapter 8

Recovery of Intermixed Interfaces

In this Chapter, microstructure evolution of multilayer after collision cascade is modeled by phase field method. We show that the survival probability of Cu-Nb layered structures approaches unity for individual layer thicknesses above 2-4 nm. This finding suggests that it is possible to synthesize Cu-Nb multilayered nanocomposites that are both radiation resistant and morphologically stable under neutron or heavy ion bombardment.

8.1 Phase field simulation setup

Chapter 7 shows the initial intermixing in Cu-Nb multilayers under collision cascades. After the collision cascade finishes, the microstructure of the system would evolve governed by thermally activated diffusion process. Since the multilayer is consisting of metals with low solid solubility, the intermixed region will de-mix and undergo phase separation. The initially pinched-off layer after collision cascade may self-heal, or pinched-off region may grow and destabilize the laminar microstructure, which eventually lead to spherodization and complete phase separation.

To determine whether a layer has pinched off, we simulate microstructure evolution after collision cascades using the phase field method [131]. We solved for the local volumetric concentration of Cu, ϕ, modeled as a conserved order parameter using Cahn-Hilliard equations [134] implemented in 3-D in the COMSOL finite element

method (FEM) code [137]. The local free energy density function we used has a double well form,

$$f(\phi) = 4\Delta f \phi^2 (1-\phi)^2, \tag{8.1}$$

where Δf is the average of the free energies of mixing of Cu and Nb in FCC and BCC crystal structures at 600K [173]. Interface thickness is set to be $\sim$2Å: comparable to the spacing between Cu {111} and Nb {110} planes and small enough to allow for convergence with respect to mesh element size. We ignore the elastic energy from the lattice mismatch between Cu and Nb as well as local distortions due to defects and defect clusters created during collision cascades. Since we are interested only in the final state of the multilayers (pinched off or not), we performed all simulations in reduced time units. Ten independent phase field simulations were preformed for each layer thickness, using their corresponding structures after collision cascade as initial local volumetric concentration.

Cu and Nb do not form compounds and have extremely low mutual solid solubility [173]. Therefore, equilibrium Cu-Nb interfaces are atomically sharp [169] and isolated Cu or Nb impurities created by irradiation de-mix over time scales governed by their diffusivities and the layer thickness. Therefore, in our analysis we adopt layer pinch-off as the criterion for onset of morphological instability. Pinch-off is known to initiate spherodization of Cu-Nb multilayers under high temperature annealing [15]. It occurs when neighboring interfaces come into contact, forming a bridge between neighboring Cu or Nb layers.

8.2 Results

An example of our phase field simulations is shown in Figure 8-1. The initial concentration field, illustrated in Figure 8-1(b), is obtained from atomic structures created by MD collision cascade simulations, such as that in Figure 8-1(a). Pinchoff channels connecting some cascade-affected layers (mostly Nb) are formed during the phase field simulation while other layers return to their initial, flat morphology, as shown in

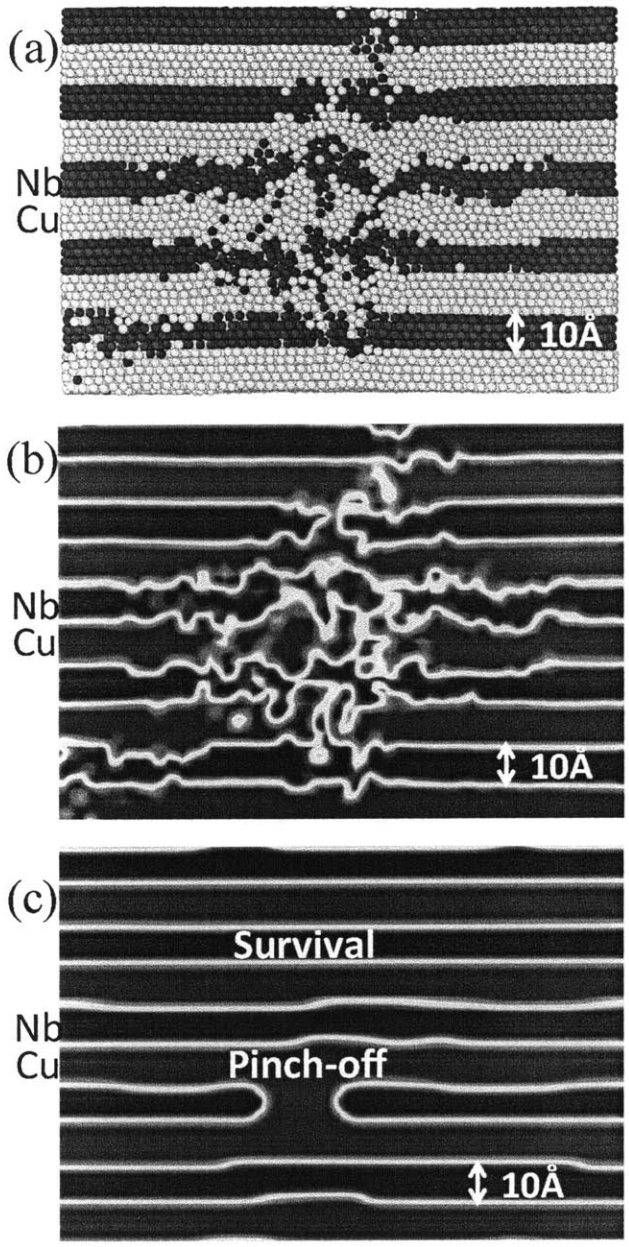

Figure 8-1: (a) Cu and Nb atoms intermixed in a 10 multilayer at the end of a 100keV collision cascade. (b) Initial concentration distribution used in phase field model, extracted from the atomic structure in (a). (c) During a phase field simulation, one Nb layer is pinched off by two neighboring Cu layers, while other layers maintain stable.

Figure 8-1(c). The width of pinchoff channels continues to increase with time, consistent with onset of the breakdown of layered morphology and eventual spherodization

[15, 189]. No cases of precipitate formation inside layers were found.

A multilayer is considered to have survived if no layers in it have pinched off. Layer pinchoff frequency and multilayer survival probability as a function of layer thickness is summarized in Figure 8-2. Phase field simulations indicate that only ~30% of 10Å multilayers survived after one collision cascade, while all other thicker layers above 18Å are morphologically stable. For a threshold impurity concentration of 30%, the occurrence frequency and survival probability obtained this way are close to those predicted by the phase field method. Thresholds of 20% and 10% may be viewed as providing more conservative estimates of layer thicknesses that are stable against pinchoff. Therefore, referring to Figure 8-2, we conclude that nanolayered composites of low solubility elements with layer thicknesses above 2-4 nm are likely to remain morphologically stable even when subjected to high-energy collisions with incoming neutrons or heavy ions.

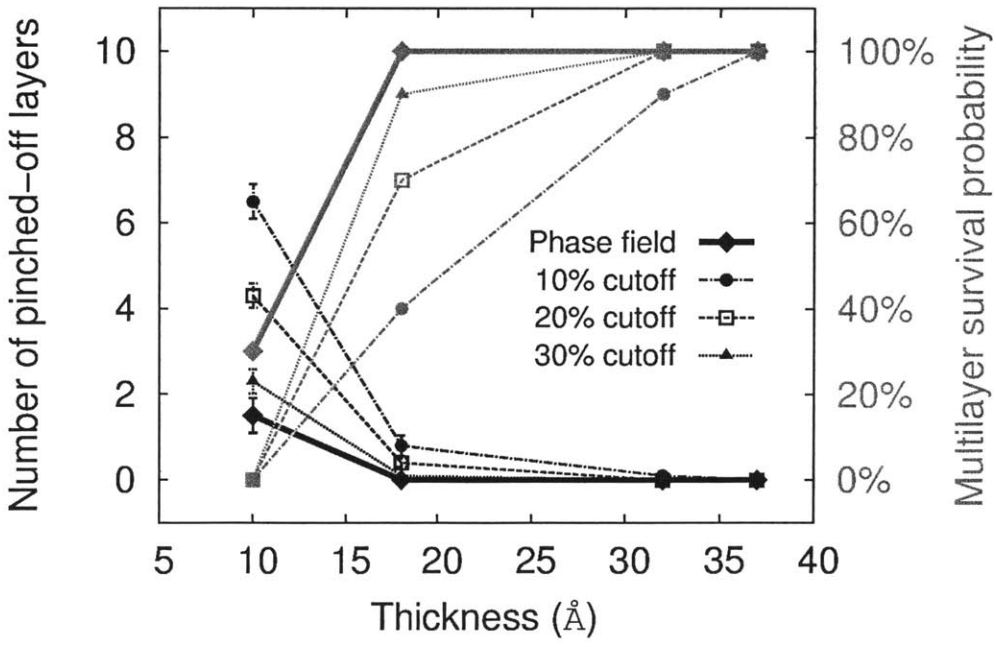

Figure 8-2: Frequency of layer pinchoff and multilayer survival probability as a function of layer thickness determined by phase field modeling as well as with different cutoff concentrations.

Chapter 9

Discussions and Conclusions

This Chapter first discusses various topics in liquid phase properties and radiation-induced mixing extended from this study. Then, the key contribution of this thesis is summarized. Lastly, insights on how to better design future radiation damage tolerant nanocomposites are presented.

9.1 Discussions

9.1.1 Liquid phase properties

In this study, we developed a Cu-Nb EAM potential (EAM1) that topologically reproduces the complete experimental phase diagram. We fitted the EAM potential to enthalpies of mixing at 0K for bcc and fcc random solid solutions across the whole composition range from first-principles calculations. The potential reproduces the liquid part of the phase diagram well despite being fitted only to $T = 0K$ properties, suggesting the possibility of some transferability of the potential to states that were not included in the fit. This potential may be used to study Cu-Nb systems whose response depends on equilibrium thermodynamic properties over their full composition range and over all temperatures.

We also computed the equilibrium binary phase diagrams of two other previously developed Cu-Nb EAM potentials and found one (EAM2) has a wide liquid misci-

bility gap while the other (EAM3) has complete liquid miscibility. Of these three potentials, the new one developed in this work (EAM1) is in best agreement with the experimental phase diagram. Because the Cu-Nb potentials we studied have widely differing liquid phase thermodynamics and structures, all three may be useful in studying the effect of liquid thermodynamics on properties of binary systems, such as radiation-induced mixing presented in Chapter 6. There is another Cu-Nb potential of Finnis-Sinclair type constructed by Wang *et al.* Their MD simulations show the formation of amorphous Cu-Nb for 15-72 at% Nb [190]. However, we did not investigate that potential in this work.

Relationships between excess volume, enthalpy of mixing, and liquid phase miscibility were discussed in a recent paper for Lennard-Jones (LJ) systems [165]. The authors found that excess volume is very sensitive to the attractive part of LJ potentials and miscibility gaps may be found in liquids with either positive or negative excess volumes. There is therefore no direct correlation between excess volume and liquid miscibility.

Similarly, in our study, EAM2 has a positive enthalpy of mixing and a liquid phase miscibility gap. EAM3 has full liquid phase solubility and at least part of its enthalpy of mixing curve dips below zero. In contrast to the LJ study, however, EAM1 has both positive enthalpy of mixing and full liquid phase miscibility. In EAM1, the positive enthalpy of mixing is not large enough to overcome the entropy contribution to form liquid miscibility gap at high temperature, and as a result, the critical temperature of a metastable liquid miscibility gap may fall below the liquidus line. Indeed, some Cu-based alloys with positive enthalpy of mixing may have metastable miscibility gaps in undercooled binary liquids [191], such as Cu-Co [192, 171] and Cu-Fe [193, 194]. Munitz *et al.* suggested that a metastable liquid miscibility gap may also be present in Cu-Nb with a critical temperature about 200C lower than the liquidus line [27]. In our study, we have not found any evidence of such a metastable miscibility gap in EAM1, however, and the possibility of a metastable miscibility gap below the solidus in Cu-Nb system appears to be of academic interest.

The enthalpies of mixing in the liquid phase for the three potentials are very

different. Although EAM2 and EAM3 are fitted to the same targets, EAM2 predicts a large positive heat of mixing in the liquid while EAM3 leads to small heats of mixing (and even negative ones in Nb rich liquids). This implies that the usual way of fitting cross potentials to fictitious compounds for immiscible systems may lead to unpredictable liquid phase properties. EAM1 is fitted to heats of mixing in solid solutions across the whole composition range, which may better mimic the chemical environment in Cu-Nb liquids. The resulting phase diagram indeed has the best agreement with the experimental phase diagram.

We found that the thermodynamic equilibrium liquid predicted by potential EAM1 is compositionally patterned. Its entropy of mixing is lower than that of the more randomly mixed liquid predicted by EAM3. To determine how much configurational entropy contributes to the difference, we estimate its value using the cluster variation method [195], taking into account contributions of first two nearest neighbor shells to the pair-probability functions [196]. We found that the configurational entropy accounts for about 8% of the difference for the entropy of mixing between EAM1 and EAM3. Thus, the main contribution may still come from the vibrational entropy contribution.

There is much evidence in the literature for medium and short-range structuring of liquids at equilibrium. For example, a neutron diffraction study of liquid Li-Pb alloys showed a preference for unlike nearest neighbors and the distance between neighboring unlike atoms [197]. Recently, Frolov and Mishin found stable "nanocolloidal" structures in a Cu-Ta system described by a semi-empirical interatomic potential [198]. They claimed that this structure arises due to a negative liquid-phase interface free energy. Bose *et al.* studied vapor deposited amorphous Cu-Nb alloy thin films and found nanoscale clustering of Cu- and Nb-rich regions with a length scale of ~2-3nm [199]. Roik *et al.* reported an X-ray diffraction study of Al-Cu melts and found medium range order existing in liquid Al-Cu binary alloy [200]. The compositionally patterned liquid structure predicted by our newly constructed potential may also be investigated by neutron or X-ray diffraction studies on Cu-Nb melts. A rise in $S_{cc}(q)$ at small wavenumber as well as a small peak near $q \approx 0.27\text{Å}^{-1}$ is expected if our

prediction is correct.

9.1.2 Radiation-induced mixing

We have shown that radiation-induced mixing (RIM) occurs by liquid phase interdiffusion in thermal spikes (TSs) followed by partial de-mixing. There is ample evidence that RIM is directly proportional to liquid phase heats of mixing in materials with negative heats of mixing [78, 75, 22, 45]: the lower the heats of mixing, the faster the RIM rate. Our study shows that mixing in immiscible metal pairs is proportional to liquid phase interdiffusivity, which also depends on the free energies of mixing through parameters s_2 and s_3 in Eq. (5.27). For EAM3, s_2 is large and positive at 4000K and therefore so is the mixing parameter (MP). By contrast, s_2 is much smaller in EAM2 at the same temperature and so is its MP. Parameter s_3 and self-diffusivities are almost the same for all three potentials.

In addition, we find that partial de-mixing occurs in TSs, after the initial liquid interdiffusion phase. Contrary to the hypothesis of de-mixing by phase separation in the liquid [78], we observe that de-mixing occurs in all three of the potentials we studied, regardless whether or not they exhibit a liquid phase miscibility gap. Our hypothesis that de-mixing in TSs occurs by solute segregation during solidification of the TS core is in qualitative agreement with our TS simulations. However, because this process likely occurs far from thermal equilibrium, conventional models for zone refining do not describe it well. Further work is required to fully understand it.

We showed that effective interdiffusivities differ for TSs occurring at interfaces (Type I) and in crystalline layers containing a low concentration of impurities (Type II). For EAM2, which has a liquid phase miscibility gap, the effective interdiffusivity for Type I TSs is close to zero while that of Type II TSs is positive. This finding suggests that MPs of layered composites made of metals with liquid phase miscibility gaps may decrease as the layer thickness decreases because the fraction of Type I cascades would increase. We investigated this possibility by carrying out multiple collision cascade simulations on Cu-Nb multilayer models, similar to simulations presented in Chapter 6. However, we found that the MP increased with decreasing

layer thickness, both when EAM2 and when EAM1 or EAM3 were used. The reason why no decrease in MP was seen for EAM2 is that when layer thickness decreases, individual TSs may cover several interfaces. Zones of liquid phase interdiffusion at neighboring interfaces then also overlap, leading to a synergistic increase in mixing beyond what was seen in the present study.

Our work also shows that low temperature heavy ion and neutron irradiation may lead to the formation of amorphous interfacial layers. Indeed, amorphization of Cu-Nb multilayers under ion irradiation has been reported [190, 201]. We find that the structures of amorphous layers in our simulations depend on the atomic potential. For EAM1 and EAM2, these layers are compositionally patterned, as in Ref. [178, 202]. On the other hand, Cu and Nb are almost ideally mixed in the amorphous layer for EAM3. These trends in amorphous layer structure reflect the liquid phase structure exhibited by these three potentials. This finding suggests that the liquid droplet at the core of a TSs may undergo vitrification, rather than crystallization, as it quenches back to ambient temperature. Compositional patterning in the amorphous layers does not appear to influence MPs for RIM.

With increasing dose, the amorphous layer grows by consuming fcc and bcc layers at different rates for the three EAM potentials. For example, EAM1 has nearly equal growth rates on both the fcc and bcc side, EAM2 has faster amorphous layer growth towards the fcc layer, and EAM3 has a higher growth rate towards the bcc layer. For EAM1 and EAM2, complete amorphization occurs first in the fcc layer while for EAM3 it occurs in the bcc layer first. The growth rate of the amorphous layer likely depends on the minimum impurity concentration required to stabilize the amorphous state [178].

This work led to an analytical expression for the MPs found for the three model systems investigated in this study. This expression incorporates mechanistic insight into the factors that influence liquid phase interdiffusivity, such as the heats and entropies of mixing. However, de-mixing is treated empirically, since reliable expressions describing non-equilibrium solute segregation at a rapidly moving solidification front are not available. Improved expressions require further investigations of this process.

Our simulations model RIM in the low temperature limit, where thermally activated recovery processes may be neglected. At elevated temperatures, radiation-induced mixing in immiscible metals is the result of competition between intermixing by the mechanisms described here and de-mixing controlled by thermally activated diffusion over much longer times. Other modeling methodssuch as kinetic Mote Carlo (kMC) [203, 204], accelerated molecular dynamics (AMD) [205, 35], or atomisticially-informed phase field simulations in Chapter 8are therefore required to study thermally activated de-mixing. High ambient temperature may also affect mixing and de-mixing within TSs, e.g. by reducing the TS quench rate [48]. These effects may be studied using the same direct MD methods described in the present study.

This work illustrates a unique capability of materials modeling: the ability to investigate the influence of a limited set of material parameters on a property of interest while keeping other parameters fixed. In experimental investigations, solid and liquid phase behavior cannot be varied independently, making it difficult to unambiguously attribute differing MP values to specific mechanisms, such as liquid phase interdiffusion. By contrast, the present study investigates RIM using several interatomic potentials, all of which have the same solid-phase behavior, but different liquid phase properties, giving us the opportunity to establish the role of liquid phase properties in RIM unambiguously.

9.2 Summary of the thesis

This thesis investigated radiation-induced mixing at interfaces between immiscible metals based on computer simulations, using Cu-Nb as a model system. The main conclusion of this thesis is:

1. An interatomic potential in EAM form is constructed to reproduce experimental Cu-Nb phase diagram.

2. Three Cu-Nb potentials with the same solid phase behaviors but distinct liquid phase properties serve as a clear and convenient set of model systems to study

liquid phase properties effect unambiguously.

3. For low solubility metals under heavy ion or neutron irradiation, mixing occurs inside thermal spikes, while the contribution from ballistic displacement is negligible.

4. For isolated interfaces, radiation-induced mixing is approximately proportional to liquid phase interdiffusivity.

5. For multilayer nanocomposites with layer thickness below 2 nm, enhanced intermixing occurs due to overlap of interdiffusion zone inside thermal spike.

6. Mixing initially occurs by liquid phase interdiffusion inside the liquid core of a thermal spike, followed by partial de-mixing due to segregation of impurities into the liquid phase during solidification of the thermal spike.

7. With the absence of thermally activated processes (i.e. under cryogenic temperature), radiation-induced mixing is independent of interface crystallography.

8. Under cryogenic temperature, an amorphous layer form and widens in proportion to the square root of dose.

9. When thermally activated recovery processes are dominate, Cu-Nb multilayer nanocomposites are morphologically stable when layer thickness is above 2-4nm.

9.3 Insights on designing future radiation-resistant nanocomposites

Since the mixing rate under thermal spike is governed by the liquid phase interdiffusivity at high temperature (2-4 times the melting temperature), it is desirable to choose low solubility metals with small liquid phase interdiffusivity as constituents for designing future morphologically stable radiation-tolerant nanocomposites. In addition, the microstructural length scale should be larger than twice the size of the interdiffusion zone inside thermal spikes.

This thesis also opens a few possible research directions about better understanding radiation-induced mixing in general and morphological stability of more complex microstructures. Here lists a few topics that remain to be further investigated:

1. Is de-mixing inside thermal spike also true in other systems? What controls de-mixing mechanism, and how one may increase the amount of de-mixing?

2. Modeling of the recovery process of intermixed interface can be improved by long-time atomistic simulations such as on-the-fly kinetic Monte Carlo methods. How to effectively and accurately simulate migration of defect clusters and evolution of complex intermixed interfacial structures is very important and challenging.

3. The properties of intermixed interfaces such as free energies, mechanical properties, and sink efficiencies need to be further studied.

4. How radiation affects the morphological stability of triple junctions of grain boundaries and interphase interface is unclear. Mixing and de-mixing at triple junctions or quadruple nodes may be investigated via molecular dynamics simulations.

5. How mixing is affected in ternary or quaternary systems, for instance one of the neighboring materials is an alloy. How compound formation would affect mixing and sink efficiencies.

6. How radiation-induced mixing coupled with other conditions such as mechanical deformations or radiation-induced segregation would affect morphological stability of multilayer nanocomposites.

7. Investigate possible ways to tune the physical properties governing mixing and microstructure stability. For example, solutes may lower liquid phase interdiffusivity, increase rate of thermally activated recovery process, or increase thermodynamic recovery driving force by reducing interface energy, all of which

would be helpful to limit the amount of mixing and extend the morphological stability.

Appendix A

Summary of fitting parameters in interatomic potential

The cross-element pairwise interaction V_{CuNb} use in EAM1 consists of 10 coefficients, as expressed in Eq. (4.8). The coefficients $c_i (i = -7 \sim 2)$ are listed in Table A.1.

The coefficients a_0, a_1, a_2, a_3 of splines that connect the Cu-Cu, Nb-Nb and Cu-Nb pair interaction potentials with ZBL short-range repulsive potential are given in Table A.2. Parameters b_2, b_3 in Eq. (4.13) for adjusting Cu and Nb electron density function are also listed in Table A.3.

Table A.1: Coefficients in the Cu-Nb pairwise interaction function, V_{CuNb}.

i	-7	-6	-5	-4	-3
c_i	-53928.7	192315	298102	263305	-145873
i	-2	-1	0	1	2
c_i	52535.7	-12297.9	1804.36	-150.613	5.45298

Table A.2: Coefficients of splines used to join the pairwise interaction to ZBL potentials.

	a_0	a_1	a_2	a_3
$\phi_{CuCu}(r)$	82.7384	-318.705	248.702	122.239
$\phi_{NbNb}(r)$	-52.4414	297.088	-689.451	655.22
$\phi_{CuNb}(r)$	18.388	-29.0737	-185.898	364.964

Table A.3: Coefficients of splines used to force electron density functions to approach zero.

	b_2	b_1
$\rho_{Cu}(r)$	0.262187	-0.108958
$\rho_{Nb}(r)$	0.416659	-0.167387

Bibliography

[1] G. S. Was, *Fundamentals of radiation materials science.* metals and alloys, Springer Verlag, 2007.

[2] S. J. Zinkle and G. S. Was, "Materials challenges in nuclear energy," *Acta Materialia*, vol. 61, pp. 735–758, Feb. 2013.

[3] S. J. Zinkle, "Fusion materials science: Overview of challenges and recent progress," *Physics of Plasmas*, vol. 12, no. 5, p. 058101, 2005.

[4] T. Allen, H. Burlet, R. K. Nanstad, M. Samaras, and S. Ukai, "Advanced Structural Materials and Cladding," *Mrs Bulletin*, vol. 34, 2009.

[5] S. J. Zinkle and J. T. Busby, "Structural materials for fission & fusion energy," *Materials Today*, vol. 12, pp. 12–19, Nov. 2009.

[6] D. Butler, "Energy: Nuclear power's new dawn," *Nature*, vol. 429, no. 6989, pp. 238–240, 2004.

[7] M. J. Demkowicz, P. Bellon, and B. D. Wirth, "Atomic-scale design of radiation-tolerant nanocomposites," *MRS Bulletin*, vol. 35, no. 12, pp. 992–998, 2010.

[8] R. L. Klueh and A. T. Nelson, "Ferritic/martensitic steels for next-generation reactors," *Journal Of Nuclear Materials*, vol. 371, pp. 37–52, Sept. 2007.

[9] R. Lindau, A. Möslang, M. Rieth, M. Klimiankou, E. Materna-Morris, A. Alamo, A. A. F. Tavassoli, C. Cayron, A. M. Lancha, P. Fernandez, N. Baluc, R. Schäublin, E. Diegele, G. Filacchioni, J. W. Rensman, B. v. d. Schaaf, E. Lucon, and W. Dietz, "Present development status of EUROFER and ODS-EUROFER for application in blanket concepts," *Fusion Engineering and Design*, vol. 75-79, pp. 989–996, Nov. 2005.

[10] G. R. Odette, M. J. Alinger, and B. D. Wirth, "Recent developments in irradiation-resistant steels," *Annu. Rev. Mater. Res.*, vol. 38, pp. 471–503, 2008.

[11] A. Misra, M. J. Demkowicz, X. Zhang, and R. G. Hoagland, "The radiation damage tolerance of ultra-high strength nanolayered composites," *JOM*, vol. 59, no. 9, pp. 62–65, 2007.

[12] W. Han, M. J. Demkowicz, N. A. Mara, and E. Fu, "Design of Radiation Tolerant Materials Via Interface Engineering," *Advanced Materials*, vol. 25, pp. 6975–6979, Dec. 2013.

[13] M. Demkowicz, R. Hoagland, and J. Hirth, "Interface Structure and Radiation Damage Resistance in Cu-Nb Multilayer Nanocomposites," *Physical Review Letters*, vol. 100, p. 136102, Apr. 2008.

[14] S. Zheng, I. J. Beyerlein, J. S. Carpenter, K. Kang, J. Wang, W. Han, and N. A. Mara, "High-strength and thermally stable bulknanolayered composites due to twin-inducedinterfaces," *Nature Communications*, vol. 4, pp. 1696–8, 2013.

[15] A. Misra and R. G. Hoagland, "Effects of elevated temperature annealing on the structure and hardness of copper/niobium nanolayered films," *Journal of Materials Research*, vol. 20, pp. 2046–2054, Aug. 2005.

[16] A. Misra, R. Hoagland, and H. Kung, "Thermal stability of self-supported nanolayered Cu-Nb films," *Philosophical Magazine*, vol. 84, pp. 1021–1028, Apr. 2004.

[17] X. Zhang, E. G. Fu, A. Misra, and M. J. Demkowicz, "Interface-enabled Defect Reduction in He Ion Irradiated Metallic Multilayers," *Jom*, vol. 62, no. 12, pp. 75–78, 2010.

[18] M. J. Demkowicz, D. Bhattacharyya, I. Usov, Y. Q. Wang, M. Nastasi, and A. Misra, "The effect of excess atomic volume on He bubble formation at fcc-bcc interfaces," *Applied Physics Letters*, vol. 97, no. 16, p. 161903, 2010.

[19] M. J. Demkowicz, A. Misra, and A. Caro, "The role of interface structure in controlling high helium concentrations," *Current Opinion in Solid State & Materials Science*, vol. 16, pp. 101–108, June 2012.

[20] A. Kashinath, A. Misra, and M. J. Demkowicz, "Stable Storage of Helium in Nanoscale Platelets at Semicoherent Interfaces," *Physical Review Letters*, vol. 110, p. 086101, Feb. 2013.

[21] R. Enrique and P. Bellon, "Compositional patterning in immiscible alloys driven by irradiation," *Physical Review B*, vol. 63, p. 134111, Mar. 2001.

[22] W. Johnson, Y. Cheng, M. Van Rossum, and M. Nicolet, "When is thermodynamics relevant to ion-induced atomic rearrangements in metals?," *Nuclear Instruments & Methods In Physics Research Section B-Beam Interactions With Materials And Atoms*, vol. 7, pp. 657–665, 1985.

[23] N. Li, E. G. Fu, H. Wang, J. J. Carter, L. Shao, S. A. Maloy, A. Misra, and X. Zhang, "He ion irradiation damage in Fe/W nanolayer films," *Journal Of Nuclear Materials*, vol. 389, pp. 233–238, May 2009.

[24] N. Li, M. S. Martin, O. Anderoglu, A. Misra, L. Shao, H. Wang, and X. Zhang, "He ion irradiation damage in Al/Nb multilayers," *Journal of Applied Physics*, vol. 105, no. 12, p. 123522, 2009.

[25] L. Zhang and M. J. Demkowicz, "Morphological stability of Cu-Nb nanocomposites under high-energy collision cascades," *Applied Physics Letters*, vol. 103, no. 6, p. 061604, 2013.

[26] H. L. Knoedler, G. E. Lucas, and C. G. Levi, "Morphological stability of copper-silver multilayer thin films at elevated temperatures," *Metallurgical and Materials Transactions A*, vol. 34, no. 5, pp. 1043–1054, 2003.

[27] A. Munitz, M. Bamberger, A. Venkert, P. Landau, and R. Abbaschian, "Phase selection in supercooled Cu–Nb alloys," *Journal of Materials Science*, vol. 44, pp. 64–73, Dec. 2008.

[28] P. Krasnochtchekov, R. Averback, and P. Bellon, "Phase separation and dynamic patterning in Cu1?xCox films under ion irradiation," *Physical Review B*, vol. 72, p. 174102, Nov. 2005.

[29] Y. T. Cheng, G. W. Auner, M. H. Alkaisi, K. R. Padmanabhan, and M. M. Karmarkar, "Thermodynamic and Ballistic Aspects of Ion Mixing," *Nuclear Inst. and Methods in Physics Research, B*, no. B59/60, pp. 509–516, 1991.

[30] M. Nastasi and J. W. Mayer, "Ion beam mixing in metallic and semiconductor materials," *Materials Science and Engineering: R: Reports*, vol. 12, no. 1, pp. 1–52, 1994.

[31] C. Fu, M. Krčmar, G. Painter, and X.-Q. Chen, "Vacancy Mechanism of High Oxygen Solubility and Nucleation of Stable Oxygen-Enriched Clusters in Fe," *Physical Review Letters*, vol. 99, p. 225502, Nov. 2007.

[32] R. Stoller, "The role of cascade energy and temperature in primary defect formation in iron," *Journal Of Nuclear Materials*, vol. 276, pp. 22–32, 2000.

[33] K. Nordlund and R. S. Averback, "Point defect movement and annealing in collision cascades," *Physical Review B*, vol. 56, no. 5, pp. 2421–2431, 1997.

[34] R. S. Averback and T. de la Rubia, "Displacement damage in irradiated metals and semiconductors," *Solid State Physics, Vol 51*, vol. 51, pp. 281–402, 1998.

[35] X. M. Bai, A. F. Voter, R. G. Hoagland, M. Nastasi, and B. P. Uberuaga, "Efficient Annealing of Radiation Damage Near Grain Boundaries via Interstitial Emission," *Science*, vol. 327, pp. 1631–1634, Mar. 2010.

[36] M. T. Robinson, "Basic physics of radiation damage production," *Journal Of Nuclear Materials*, vol. 216, pp. 1–28, 1994.

[37] M. Nastasi, J. Mayer, and J. K. Hirvonen, *Ion-Solid Interactions.* Fundamentals and Applications, Cambridge University Press, Mar. 1996.

[38] W. E. Meyerhof, "Elements of Nuclear Physics." Tata McGraw-Hill Education, New York, 1989.

[39] S. Yip, "Lecture Notes of 22.101," *MIT*, pp. 1–10, 2007.

[40] J. D. Jackson, *Classical Electrodynamics.* Wiley, Aug. 1998.

[41] J. F. Ziegler, *The stopping and range of ions in solids.* Pergamon Pr, 1985.

[42] M. Toulemonde, C. Dufour, A. Meftah, and E. Paumier, "Transient thermal processes in heavy ion irradiation of crystalline inorganic insulators," *Nuclear Inst. and Methods in Physics Research, B*, vol. 166, pp. 903–912, Apr. 2000.

[43] A. Chettah, Z. G. Wang, M. Kac, H. Kucal, A. Meftah, and M. Toulemonde, "Melting of Au and Al in nanometer Fe/Au and Fe/Al multilayers under swift heavy ions: A thermal spike study," *Nuclear Instruments & Methods In Physics Research Section B-Beam Interactions With Materials And Atoms*, vol. 245, pp. 150–156, Apr. 2006.

[44] D. Bodansky, *Nuclear energy: principles, practices, and prospects.* Springer Verlag, 2004.

[45] M. Nastasi and J. W. Mayer, "Ion beam mixing and liquid interdiffusion," *Radiation Effects and Defects in Solids*, vol. 130-131, pp. 367–385, July 1994.

[46] R. Stoller, G. Odette, and B. Wirth, "Primary damage formation in bcc iron," *Journal Of Nuclear Materials*, vol. 251, pp. 49–60, 1997.

[47] A. F. Calder, D. J. Bacon, A. V. Barashev, and Y. Osetsky, "On the origin of large interstitial clusters in displacement cascades," *Philosophical Magazine*, vol. 90, pp. 863–884, Mar. 2010.

[48] S. A. Skirlo and M. J. Demkowicz, "The role of thermal spike compactness in radiation-induced disordering and Frenkel pair production in Ni3Al," *Scripta Materialia*, vol. 67, pp. 724–727, Oct. 2012.

[49] J. A. Brinkman, "On the Nature of Radiation Damage in Metals," *Journal of Applied Physics*, vol. 25, no. 8, p. 961, 1954.

[50] F. Seitz and J. S. Koehler, "Displacement of Atoms During Irradiation," *Solid state physics: Advances in Research and Applications*, vol. 2, pp. 305–448, Nov. 1956.

[51] G. H. Vineyard, "Thermal spikes and activated processes," *Radiation Effects and Defects in Solids*, vol. 29, no. 4, pp. 245–248, 1976.

[52] T. D. de la Rubia, R. S. Averback, R. Benedek, and W. E. King, "Role of thermal spikes in energetic displacement cascades," *Physical Review Letters*, vol. 59, no. 17, p. 1930, 1987.

[53] D. N. Seidman, R. S. Averback, and K. Benedek, "Displacement cascades. Dynamics and atomic structure," *Physica Status Solidi (b)*, vol. 144, no. 1, pp. 85–104, 1987.

[54] R. Stoller and L. Greenwood, "Subcascade formation in displacement cascade simulations: Implications for fusion reactor materials," *Journal Of Nuclear Materials*, vol. 271, pp. 57–62, 1999.

[55] E. Zarkadoula, S. L. Daraszewicz, D. M. Duffy, M. A. Seaton, I. T. Todorov, K. Nordlund, M. T. Dove, and K. Trachenko, "The nature of high-energy radiation damage in iron," *Journal of Physics: Condensed Matter*, vol. 25, p. 125402, Feb. 2013.

[56] R. H. Silsbee, "Focusing in Collision Problems in Solids," *Journal of Applied Physics*, vol. 28, no. 11, p. 1246, 1957.

[57] W. E. King and R. Benedek, "Computer simulation study of the displacement threshold-energy surface in Cu," *Physical Review B (Condensed Matter)*, vol. 23, p. 6335, June 1981.

[58] A. J. E. Foreman, W. J. Phythian, and C. A. English, "The molecular dynamics simulation of irradiation damage cascades in copper using a many-body potential," *Philosophical Magazine A*, vol. 66, pp. 671–695, Nov. 1992.

[59] D. de la Rubia, R. S. Averback, H. Hsieh, and R. Benedek, "Molecular dynamics simulation of displacement cascades in Cu and Ni: Thermal spike behavior.," *Journal of Materials Research*, vol. 4, no. 3, pp. 579–586, 1989.

[60] C. Lehmann and G. Leibfried, "Long-Range Channeling Effects in Irradiated Crystals," *Journal of Applied Physics*, vol. 34, no. 9, p. 2821, 1963.

[61] M. T. Robinson and O. S. Oen, "Computer studies of the slowing down of energetic atoms in crystals," *Physical Review*, vol. 132, no. 6, p. 2385, 1963.

[62] D. S. Gemmell, "Channeling and Related Effects in the Motion of Charged Particles Through Crystals," 1974.

[63] M. J. Norgett, M. T. Robinson, and I. M. Torrens, "A proposed method of calculating displacement dose rates," *Nuclear Engineering and Design*, vol. 33, no. 1, pp. 50–54, 1975.

[64] B. Fu, B. Xu, W. Lai, Y. Yuan, H. Xu, C. Li, Y. Jia, and W. Liu, "Journal of Nuclear Materials," *Journal Of Nuclear Materials*, vol. 441, pp. 24–28, Oct. 2013.

[65] G. H. Kinchin and R. S. Pease, "The displacement of atoms in solids by radiation," *Reports on Progress in Physics*, vol. 18, no. 1, p. 1, 1955.

[66] R. E. Stoller, M. B. Toloczko, G. S. Was, A. G. Certain, S. Dwaraknath, and F. A. Garner, "Nuclear Instruments and Methods in Physics Research B," *Nuclear Inst. and Methods in Physics Research, B*, vol. 310, pp. 75–80, Sept. 2013.

[67] R. S. Averback, "Fundamental aspects of ion beam mixing," *Nuclear Instruments & Methods In Physics Research Section B-Beam Interactions With Materials And Atoms*, vol. 15, no. 1-6, pp. 675–687, 1986.

[68] E. Ma, "Alloys created between immiscible elements," *Progress In Materials Science*, vol. 50, no. 4, pp. 413–509, 2005.

[69] S. W. Chee, B. Stumphy, N. Q. Vo, R. S. Averback, and P. Bellon, "Dynamic self-organization in Cu alloys under ion irradiation," *Acta Materialia*, vol. 58, pp. 4088–4099, July 2010.

[70] P. R. Okamoto, N. Q. Lam, and L. E. Rehn, "Physics of crystal-to-glass transformations," *Solid state physics*, vol. 52, pp. 1–135, 1999.

[71] Y. T. Cheng, "Relationships between cohesive energy, Debye temperature, and the onset of temperature-dependent ion mixing," *Physical Review B (Condensed Matter)*, vol. 40, no. 10, pp. 7403–7405, 1989.

[72] J. Pacaud, G. Gladyszewski, C. Jaouen, A. Naudon, P. Goudeau, and J. Grilhe, "Low temperature mixing in Cu/W superlattices irradiated with light and heavy ions," *Journal of Applied Physics*, vol. 73, no. 6, pp. 2786–2793, 1993.

[73] S. M. Myers, "Ion-beam-induced migration and its effect on concentration profiles," *Nuclear Instruments and Methods*, vol. 168, no. 1, pp. 265–274, 1980.

[74] P. Sigmund and A. Gras-Marti, "Theoretical aspects of atomic mixing by ion beams," *Nuclear Instrumentsand Methods*, pp. 25–41, June 1981.

[75] Y. Cheng, M. Vanrossum, M. Nicolet, and W. Johnson, "Influence of Chemical Driving Forces in Ion Mixing of Metallic Bilayers," *Applied Physics Letters*, vol. 45, no. 2, pp. 185–187, 1984.

[76] A. Miedema, "The heat of formation of alloys," *Philips Technical Review*, vol. 36, no. 8, pp. 217–231, 1976.

[77] M. Van Rossum, Y. T. Cheng, M.-A. Nicolet, and W. L. Johnson, "Correlation between cohesive energy and mixing rate in ion mixing of metallic bilayers," *Applied Physics Letters*, vol. 46, no. 6, p. 610, 1985.

[78] R. S. Averback, D. Peak, and L. J. Thompson, "Ion-beam mixing in pure and in immiscible copper bilayer systems," *Appl Phys A*, vol. 39, pp. 59–64, 1986.

[79] D. Peak and R. S. Averback, "Influences of thermal spikes in ion beam mixing," *Nuclear Inst. and Methods in Physics Research, B*, vol. 7, pp. 561–565, 1985.

[80] M. J. Demkowicz and R. G. Hoagland, "Simulations of Collision Cascades in Cu-Nb Layered Composites Using An EAM Interatomic Potential," *International Journal of Applied Mechanics*, vol. 1, no. 03, pp. 421–442, 2009.

[81] R. Zhang, J. Wang, X. Liu, I. J. Beyerlein, and T. C. Germann, "Nonequilibrium molecular dynamics simulations of shock wave propagation in nanolayered Cu/Nb nanocomposites," in *SHOCK COMPRESSION OF CONDENSED MATTER - 2011: Proceedings of the Conference of the American Physical Society Topical Group on Shock Compression of Condensed Matter*, pp. 1251–1254, AIP.

[82] J. H. Li, X. D. Dai, S. H. Liang, K. P. Tai, Y. Kong, and B. X. Liu, "Interatomic potentials of the binary transition metal systems and some applications in materials physics," *Physics Reports*, vol. 455, p. 1, 2008.

[83] S. Ryu and W. Cai, "A gold–silicon potential fitted to the binary phase diagram," *Journal of Physics: Condensed Matter*, vol. 22, p. 055401, Jan. 2010.

[84] J. Hoyt, J. Garvin, E. Webb III, and M. Asta, "An embedded atom method interatomic potential for the Cu–Pb system," *Modelling and Simulation in Materials Science and Engineering*, vol. 11, p. 287, 2003.

[85] P. L. Williams, Y. Mishin, and J. C. Hamilton, "An embedded-atom potential for the Cu–Ag system," *Modelling and Simulation in Materials Science and Engineering*, vol. 14, pp. 817–833, May 2006.

[86] M. T. Robinson and I. M. Torrens, "Computer simulation of atomic-displacement cascades in solids in the binary-collision approximation," *Physical Review B*, vol. 9, no. 12, p. 5008, 1974.

[87] M. T. Robinson, "The binary collision approximation: Background and introduction," *Radiation Effects and Defects in Solids*, vol. null, pp. 3–20, July 1994.

[88] M. Hou, A. Souidi, and C. S. Becquart, "Replacement collision sequence studies in iron," *Nuclear Inst. and Methods in Physics Research, B*, vol. 196, no. 1, pp. 31–38, 2002.

[89] C. Becquart, A. Souidi, and M. Hou, "Relation between the interaction potential, replacement collision sequences, and collision cascade expansion in iron," *Physical Review B*, vol. 66, p. 134104, Oct. 2002.

[90] J. F. Ziegler, M. D. Ziegler, and J. P. Biersack, "Nuclear Instruments and Methods in Physics Research B," *Nuclear Inst. and Methods in Physics Research, B*, vol. 268, pp. 1818–1823, June 2010.

[91] M. T. Robinson, "Computer simulation studies of high-energy collision cascades," *Nuclear Inst. and Methods in Physics Research, B*, vol. 67, no. 1, pp. 396–400, 1992.

[92] M. T. Robinson, "The temporal development of collision cascades in the binary-collision approximation," *Nuclear Inst. and Methods in Physics Research, B*, vol. 48, no. 1, pp. 408–413, 1990.

[93] K. Nordlund, "Molecular dynamics simulation of ion ranges in the 1–100 keV energy range," *Computational Materials Science*, vol. 3, no. 4, pp. 448–456, 1995.

[94] J. B. Gibson, A. N. Goland, M. Milgram, and G. H. Vineyard, "Dynamics of radiation damage," *Physical Review*, vol. 120, no. 4, p. 1229, 1960.

[95] L. Bukonte, F. Djurabekova, J. Samela, K. Nordlund, S. A. Norris, and M. J. Aziz, "Nuclear Instruments and Methods in Physics Research B," *Nuclear Inst. and Methods in Physics Research, B*, vol. 297, pp. 23–28, Feb. 2013.

[96] R. E. Baumer, "Atomistic Simulations of Radiation Damage in Amorphous Metal Alloys," *MIT PhD Thesis*, 2013.

[97] K. Nordlund, J. Tarus, J. Keinonen, M. Ghaly, and R. S. Averback, "Heat spike effects on ion beam mixing," *Nuclear Inst. and Methods in Physics Research, B*, vol. 164, pp. 441–452, Apr. 2000.

[98] H. Gades and H. Urbassek, "Model study of keV-ion mixing of metallic interfaces: Influence of materials properties and deposited energy," *Physical Review B*, vol. 51, no. 20, p. 14559, 1995.

[99] K. Nordlund and R. S. Averback, "Inverse Kirkendall mixing in collision cascades," *Physical Review B*, vol. 59, no. 1, pp. 20–23, 1999.

[100] P. Sule, M. Menyhard, and K. Nordlund, "What is the real driving force of bilayer ion beam mixing?," *Nuclear Instruments & Methods In Physics Research Section B-Beam Interactions With Materials And Atoms*, vol. 226, no. 4, pp. 517–530, 2004.

[101] P. Süle and M. Menyhárd, "Strong mass effect on ion-beam mixing in metal bilayers: A ballistic picture," *Physical Review B*, vol. 71, p. 113413, Mar. 2005.

[102] P. Süle, L. Kotis, L. Toth, M. Menyhard, and W. Egelhoff Jr, "Asymmetric intermixing in Co/Ti bilayer," *Nuclear Instruments & Methods In Physics Research Section B-Beam Interactions With Materials And Atoms*, vol. 266, no. 6, pp. 904–910, 2008.

[103] P. Süle, "Anomalous atomic transport in driven systems: Ion-sputtering induced enhanced intermixing and cratering in Pt/Ti," *Nuclear Inst. and Methods in Physics Research, B*, vol. 268, pp. 1404–1411, May 2010.

[104] K. Nordlund, M. Ghaly, R. S. Averback, M. Caturla, T. Diaz de La Rubia, and J. Tarus, "Defect production in collision cascades in elemental semiconductors and fcc metals," *Physical Review B (Condensed Matter and Materials Physics)*, vol. 57, p. 7556, Apr. 1998.

[105] N. Mara, A. Misra, R. Hoagland, A. Sergueeva, T. TAMAYO, P. Dickerson, and A. Mukherjee, "High-temperature mechanical behavior/microstructure correlation of Cu/Nb nanoscale multilayers," *Materials Science and Engineering A*, vol. 493, pp. 274–282, Oct. 2008.

[106] A. Misra, J. P. Hirth, and H. Kung, "Single-dislocation-based strengthening mechanisms in nanoscale metallic multilayers," *Philosophical Magazine A*, vol. 82, no. 16, pp. 2935–2951, 2002.

[107] N. Sridhar, J. Rickman, and D. Srolovitz, "Multilayer film stability," *Journal of Applied Physics*, vol. 82, p. 4852, 1997.

[108] N. Sridhar, J. Rickman, and D. Srolovitz, "Microstructural stability of stressed lamellar and fiber composites," *Acta Materialia*, vol. 45, no. 7, pp. 2715–2733, 1997.

[109] M. A. Zaeem and S. D. Mesarovic, "Computational Materials Science," *Computational Materials Science*, vol. 50, pp. 1030–1036, Jan. 2011.

[110] B. G. Chirranjeevi, T. A. Abinandanan, and M. P. Gururajan, "A phase field study of morphological instabilities in multilayer thin films," *Acta Materialia*, vol. 57, pp. 1060–1067, Feb. 2009.

[111] H. Nakajima, K. Nonaka, Y. Obi, and H. Fujimori, "Interdiffusion in Fe/Cr multilayer thin films," *Journal of magnetism and magnetic materials*, vol. 126, no. 1, pp. 176–179, 1993.

[112] Z. Erdelyi, "Transient Interface Sharpening in Miscible Alloys," *Science*, vol. 306, pp. 1913–1915, Dec. 2004.

[113] Z. Erdélyi, I. Szabó, and D. Beke, "Interface Sharpening instead of Broadening by Diffusion in Ideal Binary Alloys," *Physical Review Letters*, vol. 89, p. 165901, Oct. 2002.

[114] J.-M. Roussel and P. Bellon, "Interface sharpening and broadening during annealing of Cu/Ni multilayers: A kinetic Monte Carlo study," *Physical Review B*, vol. 73, p. 085403, Feb. 2006.

[115] D. Josell, W. Carter, and J. Bonevich, "Stability of multilayer structures: Capillary effects," in *Nanostructured Materials*, pp. 387–390, Natl Inst Stand & Technol, Gaithersburg, MD 20899 USA, 1999.

[116] J. Kampe and T. Courtney, "Shape instabilities of plate-like structures–I. Experimental observations in heavily cold worked in situ composites," *Acta Metallurgica*, pp. 1–11, Dec. 2002.

[117] G. Sharma, R. V. Ramanujan, and G. P. Tiwari, "Instability mechanisms in lamellar microstructures," *Acta Materialia*, vol. 48, no. 4, pp. 875–889, 2000.

[118] A. Lewis, D. Josell, and T. Weihs, "Stability in thin film multilayers and microlaminates: the role of free energy, structure, and orientation at interfaces and grain boundaries," *Scripta Materialia*, vol. 48, no. 8, pp. 1079–1085, 2003.

[119] J. Wang and P. M. Anderson, "Pinch-off maps for the design of morphologically stable multilayer thin films with immiscible phases," *Acta Materialia*, vol. 53, pp. 5089–5099, Nov. 2005.

[120] H. Wan, Y. Shen, J. Wang, Z. Shen, and X. Jin, "A predictive model for microstructure evolution in metallic multilayers with immiscible constituents," *Acta Materialia*, vol. 60, pp. 6869–6881, Nov. 2012.

[121] H. Wan, Y. Shen, X. He, and J. Wang, "Modeling of Microstructure Evolution in Metallic Multilayers with Immiscible Constituents," *Jom*, vol. 65, pp. 443–449, Jan. 2013.

[122] E. G. Fu, A. Misra, H. Wang, L. Shao, and X. Zhang, "Interface enabled defects reduction in helium ion irradiated Cu/V nanolayers," *Journal Of Nuclear Materials*, vol. 407, pp. 178–188, Dec. 2010.

[123] M. Daw, S. Foiles, and M. Baskes, "The Embedded-Atom Method - A review of theory and applications," *Materials Science Reports*, vol. 9, no. 7-8, pp. 251–310, 1993.

[124] D. P. Bertsekas, "Nonlinear programming," 1995.

[125] W. H. Press, *Numerical Recipes 3rd Edition.* The Art of Scientific Computing, Cambridge University Press, Sept. 2007.

[126] D. Frenkel, "Understanding molecular simulation: from algorithms to applications." Academic Pr, 2002.

[127] S. Plimpton, "Fast parallel algorithms for short-range molecular dynamics," *Journal of Computational Physics*, vol. 117, no. 1, pp. 1–19, 1995.

[128] A. Stukowski, "Visualization and analysis of atomistic simulation data with OVITO–the Open Visualization Tool," *Modelling and Simulation in Materials Science and Engineering*, vol. 18, p. 015012, Dec. 2009.

[129] J. Li, "AtomEye: an efficient atomistic configuration viewer," *Modelling and Simulation in Materials Science and Engineering*, vol. 11, no. 2, p. 173, 2003.

[130] B. Sadigh, P. Erhart, A. Stukowski, A. Caro, E. Martinez, and L. Zepeda-Ruiz, "Scalable parallel Monte Carlo algorithm for atomistic simulations of precipitation in alloys," *Physical Review B*, vol. 85, p. 184203, May 2012.

[131] L.-Q. Chen, "Phase-field models for microstructure evolution," *Annu. Rev. Mater. Res.*, vol. 32, pp. 113–140, Aug. 2002.

[132] Y. Wang and J. Li, "Phase field modeling of defects and deformation," *Acta Materialia*, vol. 58, no. 4, pp. 1212–1235, 2010.

[133] R. W. Balluffi, S. M. Allen, W. C. Carter, and R. A. Kemper, *Kinetics of materials*. Wiley-Interscience, 2005.

[134] J. W. Cahn and J. E. Hilliard, "Free energy of a nonuniform system. I. Interfacial free energy," *Journal Of Chemical Physics*, vol. 28, no. 2, p. 258, 1958.

[135] J. Cahn, "Free energy of a nonuniform system. II. Thermodynamic basis," *The Journal of Chemical Physics*, vol. 30, p. 1121, 1959.

[136] J. Cahn and J. Hilliard, "Free Energy of a Nonuniform System. III. Nucleation in a Two Component Incompressible Fluid," *The Journal of Chemical Physics*, vol. 31, p. 688, 1959.

[137] "COMSOL Multiphysics Version 4.0 released," *Sealing Technology*, vol. 2010, no. 7, p. 4 EP.

[138] M. Daw and M. Baskes, "Embedded-Atom Method - Derivation and application to impurities, surfaces, and other effects in metals," *Physical Review B*, vol. 29, no. 12, pp. 6443–6453, 1984.

[139] M. W. Finnis and J. E. Sinclair, "A simple empirical N-body potential for transition metals," *Philosophical Magazine A*, vol. 50, pp. 45–55, July 1984.

[140] A. Voter, "Embedded Atom Method Potentials for Seven FCC metals: Ni, Pd, Pt, Cu, Ag, Au, and Al," *Los Alamos Unclassified Report LA-UR 93-3901*, 1993.

[141] R. Johnson and D. Oh, "Analytic embedded atom method model for bcc metals," *Journal of Materials Research*, vol. 4, no. 5, pp. 1195–1201, 1989.

[142] G. J. Ackland and R. Thetford, "An improved N-body semi-empirical model for body-centred cubic transition metals," *Philosophical Magazine A*, vol. 56, pp. 15–30, July 1987.

[143] Y. Mishin, M. Mehl, D. Papaconstantopoulos, A. Voter, and J. Kress, "Structural stability and lattice defects in copper: Ab initio, tight-binding, and embedded-atom calculations," *Physical Review B*, vol. 63, p. 224106, May 2001.

[144] D. Nguyen-Manh, A. Horsfield, and S. Dudarev, "Self-interstitial atom defects in bcc transition metals: Group-specific trends," *Physical Review B*, vol. 73, Jan. 2006.

[145] P. Derlet, D. Nguyen-Manh, and S. Dudarev, "Multiscale modeling of crowdion and vacancy defects in body-centered-cubic transition metals," *Physical Review B*, vol. 76, p. 054107, Aug. 2007.

[146] R. F. Zhang, J. Wang, I. J. Beyerlein, and T. C. Germann, "Twinning in bcc metals under shock loading: a challenge to empirical potentials," *Philosophical Magazine Letters*, vol. 91, pp. 731–740, Dec. 2011.

[147] A. Caro, D. Crowson, and M. Caro, "Classical Many-Body Potential for Concentrated Alloys and the Inversion of Order in Iron-Chromium Alloys," *Physical Review Letters*, vol. 95, p. 075702, Aug. 2005.

[148] G. Ackland and V. VITEK, "Many-Body Potentials and Atomic-Scale Relaxations in Noble-Metal Alloys," *Physical Review B*, vol. 41, no. 15, pp. 10324–10333, 1990.

[149] J. Soler, E. Artacho, J. Gale, A. Garcia, J. Junquera, P. Ordejon, and D. Sanchez-Portal, "The SIESTA method for ab initio order-N materials simulation," *Journal of Physics: Condensed Matter*, vol. 14, no. 11, pp. 2745–2779, 2002.

[150] D. Ceperley and B. ALDER, "Ground-State of the Electron-Gas by a Stochastic Method," *Physical Review Letters*, vol. 45, no. 7, pp. 566–569, 1980.

[151] R. M. Martin, *Electronic structure.* basic theory and practical methods, Cambridge Univ Pr, Apr. 2004.

[152] M. METHFESSEL and A. PAXTON, "High-Precision Sampling for Brillouin-Zone Integration in Metals," *Physical Review B*, vol. 40, no. 6, pp. 3616–3621, 1989.

[153] A. Zunger, S. Wei, and L. Ferreira, "Special quasirandom structures," *Physical Review Letters*, vol. 65, no. 3, pp. 353–356, 1990.

[154] O. Redlich, "Algebraic representation of thermodynamic properties and the classification of solutions," *Industrial & Engineering Chemistry*, vol. 40, no. 2, pp. 345–348, 1948.

[155] G. Kresse and J. HAFNER, "Norm-Conserving and Ultrasoft Pseudopotentials for First-Row and Transition-Elements," *Journal of Physics: Condensed Matter*, vol. 6, no. 40, pp. 8245–8257, 1994.

[156] D. VANDERBILT, "Soft Self-Consistent Pseudopotentials in a Generalized Eigenvalue Formalism," *Physical Review B*, vol. 41, no. 11, pp. 7892–7895, 1990.

[157] G. Kresse and J. Furthmuller, "Efficiency of ab-initio total energy calculations for metals and semiconductors using a plane-wave basis set," *Computational Materials Science*, vol. 6, no. 1, pp. 15–50, 1996.

[158] G. Kresse and J. Furthmuller, "Efficient iterative schemes for ab initio total-energy calculations using a plane-wave basis set," *Physical Review B*, vol. 54, no. 16, pp. 11169–11186, 1996.

[159] L. Zhang, E. Martinez, A. Caro, X.-Y. Liu, and M. J. Demkowicz, "Liquid-phase thermodynamics and structures in the Cu–Nb binary system," *Modelling and Simulation in Materials Science and Engineering*, vol. 21, p. 025005, Jan. 2013.

[160] E. Ogando Arregui, M. Caro, and A. Caro, "Numerical evaluation of the exact phase diagram of an empirical Hamiltonian: Embedded atom model for the Au-Ni system," *Physical Review B*, vol. 66, p. 054201, Aug. 2002.

[161] E. Ogando, M. Caro, and A. Caro, "Reference systems for computational free energy calculations of binary solutions: role of the constrained center of mass motion," *Computational Materials Science*, vol. 25, no. 3, pp. 297–304, 2002.

[162] E. Lopasso, M. Caro, A. Caro, and P. Turchi, "Phase diagram of an empirical potential: The case of Fe-Cu," *Physical Review B*, vol. 68, p. 214205, Dec. 2003.

[163] M. Laradji and D. Landau, "Structural properties of Si_{1-x} Ge_x alloys: A Monte Carlo simulation with the Stillinger-Weber potential," *Physical Review B*, vol. 51, no. 8, pp. 4894–4902, 1995.

[164] B. DUNWEG and D. Landau, "Phase-Diagram and Critical-Behavior of the Si-Ge Unmixing Transition - a Monte-Carlo Study of a Model with Elastic Degrees of Freedom," *Physical Review B*, vol. 48, no. 19, pp. 14182–14197, 1993.

[165] S. Amore, J. Horbach, and I. Egry, "Is there a relation between excess volume and miscibility in binary liquid mixtures?," *Journal Of Chemical Physics*, vol. 134, no. 4, p. 044515, 2011.

[166] P. Erhart, A. Caro, M. Serrano De Caro, and B. Sadigh, "Short-range order and precipitation in Fe-rich Fe-Cr alloys: Atomistic off-lattice Monte Carlo simulations," *Physical Review B*, vol. 77, p. 134206, Apr. 2008.

[167] A. B. Bhatia and D. E. Thornton, "Structural aspects of the electrical resistivity of binary alloys," *Physical Review B-Solid State*, vol. 2, no. 8, pp. 3004–3012, 1970.

[168] W. Shinoda, M. Shiga, and M. Mikami, "Rapid estimation of elastic constants by molecular dynamics simulation under constant stress," *Physical Review B*, vol. 69, p. 134103, Apr. 2004.

[169] T. Höchbauer, A. Misra, K. Hattar, and R. G. Hoagland, "Influence of interfaces on the storage of ion-implanted He in multilayered metallic composites," *Journal of Applied Physics*, vol. 98, no. 12, p. 123516, 2005.

[170] J. Pacaud, C. Jaouen, and G. Gladyszewski, "Irradiation effects in Cu/W multilayers: Ion beam mixing and structural evolution," *Journal of Applied Physics*, vol. 86, no. 9, p. 4847, 1999.

[171] S. Curiotto, R. Greco, N. H. Pryds, E. Johnson, and L. Battezzati, "The liquid metastable miscibility gap in Cu-based systems," in *Fluid Phase Equilibria*, pp. 132–136, Univ Turin, Ctr Eccellenza NIS, Dipartimento Chim IFM, I-10125 Turin, Italy, 2007.

[172] A. Crespo-Sosa, M. Muñoz, J.-C. Cheang-Wong, A. Oliver, J. M. Sániger, and J. G. Bañuelos, "Thermal spikes in Ag/Fe and Cu/Fe ion beam mixing," *Materials Science and Engineering B*, vol. 100, pp. 297–303, July 2003.

[173] L. Kaufman, "Coupled phase diagrams and thermochemical data for transition metal binary systems-III," *Calphad*, vol. 1, no. 2, pp. 117–146, 1978.

[174] T. E. Mitchell, Y. C. Lu, M. Nastasi, and H. Kung, "Structure and mechanical properties of copper/niobium multilayers," *Journal of the American Ceramic Society*, vol. 80, no. 7, pp. 1673–1676, 1997.

[175] M. J. Demkowicz and L. Thilly, "Structure, shear resistance and interaction with point defects of interfaces in Cu–Nb nanocomposites synthesized by severeplastic deformation," *Acta Materialia*, vol. 59, pp. 7744–7756, Dec. 2011.

[176] L. Thilly, M. Veron, O. Ludwig, F. Lecouturier, J. P. Peyrade, and S. Askénazy, "High-strength materials: in-situ investigations of dislocation behaviour in Cu-Nb multifilamentary nanostructured composites," *Philosophical Magazine A*, vol. 82, no. 5, pp. 925–942, 2002.

[177] A. Stukowski, "Structure identification methods for atomistic simulations of crystalline materials," *Modelling and Simulation in Materials Science and Engineering*, vol. 20, p. 045021, May 2012.

[178] R. Banerjee, A. Puthucode, S. Bose, and P. Ayyub, "Nanoscale phase separation in amorphous immiscible copper-niobium alloy thin films," *Applied Physics Letters*, vol. 90, no. 2, p. 021904, 2007.

[179] M. A. Dayananda and D. A. Behnke, "Effective Interdiffusion Coefficients and Penetration Depths," *Scripta Metallurgica Et Materialia*, vol. 25, pp. 2187–2191, Sept. 1991.

[180] M. A. Dayananda, "Average effective interdiffusion coefficients and the Matano plane composition," *Metallurgical and Materials Transactions A*, vol. 27, no. 9, pp. 2504–2509, 1996.

[181] M. Demkowicz and A. Argon, "High-Density Liquidlike Component Facilitates Plastic Flow in a Model Amorphous Silicon System," *Physical Review Letters*, vol. 93, p. 025505, July 2004.

[182] M. Demkowicz and A. Argon, "Liquidlike atomic environments act as plasticity carriers in amorphous silicon," *Physical Review B*, vol. 72, p. 245205, Dec. 2005.

[183] C. H. Rycroft, "VORO++: A three-dimensional Voronoi cell library in C++," *Chaos: An Interdisciplinary Journal of Nonlinear Science*, vol. 19, no. 4, p. 041111, 2009.

[184] A. Lund and C. Schuh, "Driven Alloys in the Athermal Limit," *Physical Review Letters*, vol. 91, p. 235505, Dec. 2003.

[185] E. Lopasso, M. Caro, and A. Caro, "Thermomigration produced by collision cascades in solid solutions," *Physical Review B (Condensed Matter)*, vol. 63, no. 17, 2001.

[186] E. M. Lopasso, A. Caro, and M. Caro, "How fast are the ultra-fast nano-scale solid–liquid phase transitions induced by energetic particles in solids?," *Journal Of Nuclear Materials*, vol. 323, pp. 263–267, Dec. 2003.

[187] A. Caro, M. Alurralde, R. Saliba, and M. Caro, "Heat and mass transport in nanoscale phase transitions induced by collision cascades," *Journal Of Nuclear Materials*, vol. 251, pp. 72–76, 1997.

[188] J. M. Howe, *Interfaces in materials.* atomic structure, thermodynamics and kinetics of solid-vapor, solid-liquid and solid-solid interfaces, Wiley-Interscience, Feb. 1997.

[189] P. Troche, J. Hoffmann, K. Heinemann, F. Hartung, G. Schmitz, H. Freyhardt, D. Rudolph, J. Thieme, and P. Guttmann, "Thermally driven shape instabilities of Nb/Cu multilayer structures: instability of Nb/Cu multilayers," *Thin Solid Films*, vol. 353, pp. 33–39, Sept. 1999.

[190] T. L. Wang, J. H. Li, K. P. Tai, and B. X. Liu, "Formation of amorphous phases in an immiscible Cu–Nb system studied by molecular dynamics simulation and ion beam mixing," *Scripta Materialia*, vol. 57, pp. 157–160, July 2007.

[191] C. D. Cao, Z. Sun, X. J. Bai, L. B. Duan, J. B. Zheng, and F. Wang, "Metastable phase diagrams of Cu-based alloy systems with a miscibility gap in undercooled state," *Journal of Materials Science*, vol. 46, pp. 6203–6212, May 2011.

[192] C. Cao, B. Wei, and D. Herlach, "Disperse structures of undercooled Co-40 wt% Cu droplets processed in drop tube," *Journal of Materials Science Letters*, vol. 21, no. 4, pp. 341–343, 2002.

[193] D. Li, M. Robinson, and T. Rathz, "Measurements of liquidus temperatures in the Cu-Nb and Cu-Cr systems," *J. Phase Equilib.*, vol. 21, no. 2, pp. 136–140, 2000.

[194] C. Wang, X. Liu, I. Ohnuma, R. Kainuma, and K. Ishida, "Formation of immiscible alloy powders with egg-type microstructure," *Science*, vol. 297, no. 5583, pp. 990–993, 2002.

[195] R. Kikuchi, "A theory of cooperative phenomena," *Physical Review*, vol. 81, no. 6, pp. 998–1003, 1951.

[196] G. Bonny, P. Erhart, A. Caro, R. C. Pasianot, L. Malerba, and M. Caro, "The influence of short range order on the thermodynamics of Fe-Cr alloys," *Modelling and Simulation in Materials Science and Engineering*, vol. 17, no. 2, p. 025006, 2009.

[197] H. Ruppersberg, "Short range order in liquid Li–Pb alloys," *The Journal of Chemical Physics*, vol. 63, no. 10, pp. 4095–4103, 1975.

[198] T. Frolov and Y. Mishin, "Stable Nanocolloidal Structures in Metallic Systems," *Physical Review Letters*, vol. 104, no. 5, p. 055701, 2010.

[199] S. Bose, A. Puthucode, R. Banerjee, and P. Ayyub, "The influence of nanoscale phase separation and devitrification on the electrical transport properties of amorphous Cu–Nb alloy thin films," *Journal of Physics: Condensed Matter*, vol. 21, p. 285305, June 2009.

[200] O. S. Roik, O. V. Samsonnikov, V. P. Kazimirov, V. E. Sokolskii, and S. M. Galushko, "Medium-range order in Al-based liquid binary alloys," *Journal of Molecular Liquids*, vol. 151, pp. 42–49, Jan. 2010.

[201] H. C. Andersen, K. Dyrbye, and J. Bottiger, "ON METALLIC-GLASS FORMATION IN CU-NB BY ION-BEAM MIXING," *Mat Sci Eng A*, vol. 115, pp. 123–126, 1989.

[202] R. E. Baumer and M. J. Demkowicz, "Glass Transition by Gelation in a Phase Separating Binary Alloy," *Physical Review Letters*, vol. 110, p. 145502, Apr. 2013.

[203] C.-C. Fu, J. D. Torre, F. Willaime, J.-L. Bocquet, and A. Barbu, "Multiscale modelling of defect kinetics in irradiated iron," *Nature Materials*, vol. 4, pp. 68–74, Dec. 2004.

[204] E. Martínez, J. Marian, M. H. Kalos, and J. M. Perlado, "Synchronous parallel kinetic Monte Carlo for continuum diffusion-reaction systems," *Journal of Computational Physics*, vol. 227, p. 3804, Apr. 2008.

[205] A. F. Voter, F. Montalenti, and T. C. Germann, "Extending the Time Scale in Atomistic Simulations of Materials," *Annu. Rev. Mater. Res.*, vol. 32, pp. 321–346, Aug. 2002.